Universität Zürich
Physik-Institut

www.physik.uzh.ch

Wissenschaftlicher Jahresbericht

April 2008 - März 2009

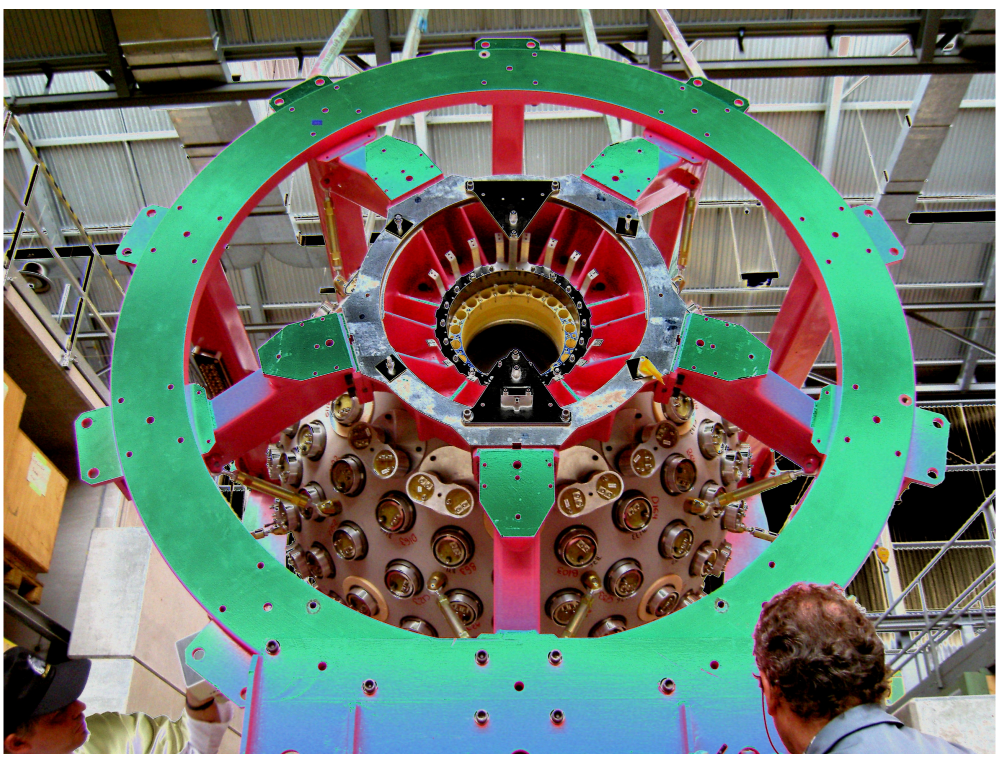

Winterthurerstrasse 190, CH-8057 Zürich/Schweiz

Universität Zürich
Physik-Institut

www.physik.uzh.ch

Wissenschaftlicher Jahresbericht

April 2008 - März 2009

Winterthurerstrasse 190, CH-8057 Zürich/Schweiz

The picture on the front shows the 3π sr pure CsI electromagnetic calorimeter used by the PEN collaboration at PSI (see Sec. 5). The picture on the back shows a beam tracking element used during past year's measuring period.

Sekretariat	044 635 5721	secret@physik.uzh.ch
Prof. C. Amsler	044 635 5784 022 767 2914	amsler@cern.ch
Prof. L. Baudis	044 635 5777	lbaudis@physik.uzh.ch
Prof. H.-W. Fink	044 635 5801	hwfink@physik.uzh.ch
Prof. H. Keller	044 635 5748	keller@physik.uzh.ch
Prof. J. Osterwalder	044 635 5827	osterwal@physik.uzh.ch
Prof. A. Schilling	044 635 5791	schilling@physik.uzh.ch
Prof. U.D. Straumann	044 635 5768	strauman@physik.uzh.ch

The annual reports are available on the internet: http://www.physik.uzh.ch/reports.html.

Begleitwort

Die sieben Forschungsgruppen des Physik-Instituts der Unversität Zürich decken ein breites Spektrum aktueller Themen aus der modernen Physik ab [1]: Physik biologischer Systeme, Oberflächenphysik, Physik magnetischer und supraleitender Materialien, Elementarteilchen- und Astroteilchenphysik. Dieser Jahresbericht [2] dokumentiert die zwischen April 2008 und März 2009 erzielten Fortschritte der Forschungsgruppen. Alle Forschungsgruppen arbeiten in einem breit abgestützten nationalen und internationalen Umfeld und haben in diesem Berichtsjahr Resultate von hohem internationalem Niveau erzielt.

Im September 2008 hat PD Dr. Christof Aegerter seine Tätigkeit am Physik-Institut aufgenommen. Die von *SystemsX.ch* unterstützte Gruppe Aegerter erweitert die Forschungsaktivitäten am Physik-Institut auf dem Gebiet der *Physical System Biology and Non-Equilibrium Soft Matter*.

Die Forschungsgruppen wurden im Berichtsjahr vom *Schweizerischen Nationalfonds* und mit Beiträgen aus der *K. Alex Müller Stiftung*, des *Zürcher Universitätsvereins*, der *Volkswagenstiftung* sowie durch Drittmittelbeiträge des *Paul Scherrer Instituts*, des *IBM Forschungslaboratoriums Rüschlikon* und von der *Swiss Initiative in System Biology (SystemsX.ch)* unterstützt. Das Physik-Institut ist am Nationalen Forschungskompetenzzentrum (NCCR) *Materials with Novel Electronic Properties (MaNEP)* und am *Swiss Institute of Particle Physics (CHIPP)* beteiligt. Es stellt gegenwärtig den Vorsitzenden des *CHIPP* und den wissenschaftlichen Delegierten der Schweiz im CERN-Rat.

Drei Forschungsgruppen des Physik-Instituts sind an EU-Projekten beteiligt, nämlich auf dem Gebiet der Nanowissenschaften an den beiden Projekten *Nanomesh - Boron Nitride Nanomesh as a Scaffold for Nanocatalysts, Nanomagnets and Functional Surfaces* und *SIBMAR - Obtaining Atomically Resolved Structural Information on Individual Bio-Molecules using Electron Holography* sowie auf dem Gebiet der kondensierten Materie am Projekt *Controlling Mesoscopic Phase Separation (CoMePhS)*. Die beiden EU-Projekte aus den Nanowissenschaften werden von Mitgliedern des Physik-Instituts geleitet. Die Projekte *Nanomesh* und *CoMePhS* wurden im Berichtsjahr erfolgreich abgeschlossen.

An dieser Stelle möchte ich dem technischen und administrativen Personal des Physik-Instituts herzlich danken, das mit grossem Einsatz massgeblich zum Gelingen der wissenschaftlichen Forschungsarbeiten im Berichtsjahr beigetragen hat. Besonders verdankt wird die wirksame finanzielle Unterstützung der forschungsfördernden Institutionen.

Zürich, im Mai
Prof. Dr. Hugo Keller

[1] Die Forschungsprojekte des Physik-Instituts findet man auf den Websites der Forschungsdatenbank der Universität Zürich: `http://www.research-projects.uzh.ch/math/unit71600/index.htm`.

[2] Der vollständige Jahresbericht wie auch die Jahresberichte früherer Jahre können auf der Website des Physik-Instituts eingesehen werden: `http://www.physik.uzh.ch/reports.html`.

Mitarbeiter

Wissenschaftliches Personal

Dr. Christof	Aegerter	Phys. Systembiologie
Enver	Alagöz	CMS
Dr. Yves	Allkofer	DIRAC
Prof. Claude	Amsler	ArDM, DIRAC, CMS
Jonathan	Anderson	LHCb
Sebastian	Arrenberg	CDMS
Ali	Askin	XENON
Holger	Bartolf	PTM
Prof. Laura	Baudis	CDMS, GERDA, XENON
Annika	Behrens	XENON
Markus	Bendele	Supraleitung & Magnetismus
Dr. Roland	Bernet	LHCb
Vittorio	Boccone	ArDM
Dominic	Böni	Oberflächenphysik
Olaf	Bossen	PTM
Tobias	Bruch	CDMS
Thomas	Brugger	Oberflächenphysik
Angela	Büchler	LHCb
Nicola	Chiapolini	LHCb
Dr. Vincenzo	Chiochia	CMS
William	Creus	ArDM
Michel	De Cian	LHCb
Dr. Raffaele	Dell´Amore	PTM
Jan-Hugo	Dil	Oberflächenphysik
Patrik	Donà	Oberflächenphysik
Dr. Andreas	Engel	PTM
Conrad	Escher	Bio-Physik
Dr. Dmitry	Eshchenko	Supraleitung & Magnetismus
Dr. Alfredo	Ferella	GERDA, XENON
Prof. Hans-Werner	Fink	Bio-Physik
Francis	Froborg	GERDA
Arno	Gadola	H1,CTA
Dr. Carine	Galli Marxer	Oberflächenphysik
Matthias	Germann	Bio-Physik
Luis	Gómez	PTM
Prof. Thomas	Greber	Oberflächenphysik
Heinz	Gross	Bio-Physik
Marijke	Haffke	XENON
Viktor	Hangartner	LHCb
Cynthia	Hengsberger	Oberflächenphysik
Dr. Matthias	Hengsberger	Oberflächenphysik
Dr. Stefan	Heule	UCN

Wissenschaftliches Personal (cont)

Dr. Sosuke	Horikawa	DIRAC
Ben	Huber	CTA
Kevin	Inderbitzin	PTM
Prof. Hugo	Keller	Supraleitung & Magnetismus
Alexander	Kish	XENON
Martin	Klöckner	Oberflächenphysik
Andreas	Knecht	UCN
Dr. Fabio	La Mattina	Supraleitung & Magnetismus
Dr. Tatiana	Latychevskaia	Bio-Physik
Dominik	Leuenberger	Oberflächenphysik
Jean-Nicolas	Longchamp	Bio-Physik
Haifeng	Ma	Oberflächenphysik
Dr. Alexander	Maisuradze	Supraleitung & Magnetismus
Dr. Mihael	Mali	Supraleitung & Magnetismus
Aaron	Manalaysay	XENON
Teresa	Marrodan-Undagoitia	XENON
Fabian	Meier	Oberflächenphysik
Hanspeter	Meyer	CMS
Barbara	Millan Mejias	CMS
Martin	Morscher	Oberflächenphysik
Prof. K. Alex	Müller	Supraleitung & Magnetismus
Dr. Katharina	Müller	H1
Krzysztof	Nowak	H1
Prof. Jürg	Osterwalder	Oberflächenphysik
Dr. Polina	Otyugova	ArDM
Praveen	Prem	Supraleitung & Magnetismus
Dr. Christian	Regenfus	CMS, ArDM, DIRAC
Mark	Reibelt	PTM
Dr. Peter	Robmann	CMS, H1, $\pi \to e\nu$
Tanja	Rommerskirchen	CMS
Dr. Josef	Roos	Supraleitung & Magnetismus
Silvan	Roth	Oberflächenphysik
Christophe	Salzmann	LHCb
Dr. Roberto	Santorelli	GERDA, XENON
Prof. Andreas	Schilling	PTM
Thomas	Schluck	Phys. Systembiologie
Jeanette	Schmidlin	Oberflächenphysik
Dr. Alexander	Schmidt	CMS
Prof. Toni	Schneider	Supraleitung & Magnetismus
Stefan	Siegrist	PTM
Dr. Olaf	Steinkamp	LHCb, CTA
Elvira	Steinwand	Bio-Physik
Dr. Simon	Strässle	Supraleitung & Magnetismus
Prof. Ulrich	Straumann	H1, LHCb, $\pi \to e\nu$, UCN, CTA
Michal	Tarka	CDMS, GERDA

Wissenschaftliches Personal (cont)

Mario	Thomann	Oberflächenphysik
Dr. Mark	Tobin	LHCb
Prof. Peter	Truöl	H1, $\pi \rightarrow e\nu$
Dimitrios	Tsirigkas	CMS
Dr. Eirini	Tziaferi	XENON
Dr. Andries	van der Schaaf	$\pi \rightarrow e\nu$
Dr. Jeroen	van Tilburg	LHCb
Dr. Ivo	Vellekoop	Phys. Systembiologie
Dr. Achim	Vollhardt	Elektronik, LHCb, CTA
Stephen	Weyeneth	Supraleitung & Magnetismus
Dr. Andreas	Wenger	D0
Lotte	Wilke	CMS
Bastian M.	Wojek	Supraleitung & Magnetismus
Dr. Hirofumi	Yanagisawa	Oberflächenphysik

Technisches und administratives Personal

Eva	Baby	Sekretariat
Kurt	Bösiger	Werkstatt
Tiziano	Crudeli	Zeichnen
Walter	Fässler	Dokumentation, Elektronik
Omid	Fardin	Werkstatt
Ruth	Halter	Sekretariat
Martin	Klöckner	Oberflächenphysik
Bruno	Lussi	Werkstatt
Reto	Maier	Werkstatt
Hanspeter	Meyer	Elektronik, CMS
Tizian	Naterop	Werkstatt
Lucien	Pauli	Vorlesungsbetrieb
Jacky	Rochet	CMS, ArDM, DIRAC
Monika	Röllin	Sekretariat
Marcel	Schaffner	Werkstatt
Jacqueline	Schenk	Sekretariat
Silvio	Scherr	Werkstatt
Jürg	Seiler	Vorlesungsbetrieb
Peter	Soland	Elektronik
Stefan	Steiner	CAD, CMS, LHCb, CTA
Michael	Weber	Vorlesungsbetrieb

Contents

1 Search for dark matter with liquid argon

C. Amsler, V. Boccone, W. Creus, A. Dell'Antone[3], S. Horikawa, P. Otyugova, C. Regenfus, and J. Rochet

in collaboration with:
ETHZ, CIEMAT (Madrid), Soltan Institute (Warsaw), Universities of Granada and Sheffield

(ArDM Collaboration)

Weakly Interacting Massive Particles (WIMPs) are prime candidates for the dark matter in the universe (1). Because dark matter has survived since the birth of the universe it has to be stable and only weakly interacting. The lightest supersymmetric particle in SUSY models conserving R-parity is the most popular candidate for WIMPs. This is the spin 1/2 neutralino χ with mass in the 10 GeV to 10 TeV range. R-parity conservation ensures that the χ is stable. Also, the χ cannot transform into other SUSY particles when interacting with matter, due to its low mass. At the LHC the χ will therefore manifest itself by a large missing energy. On the other hand, the χ can scatter e.g. on constituent quarks in nucleons or nuclei (Fig. 1.1), leading to nuclear recoils in the range of 1 – 100 keV. Non-accelerator laboratory search experiments such as ArDM are all based on the detection of such nuclear recoils.

The XENON-10 (2) and CDMS (3) experiments have produced the best upper limits so far of about 4×10^{-8} pb for the WIMP cross section on nucleons around WIMP masses of 30, resp. 70 GeV. We plan to improve on the sensitivity reached for WIMPs by 1– 2 orders of magnitude and are constructing at CERN a 1 t liquid argon detector using the two-phase technique to detect both charge and luminescence produced by the recoil nuclei following a WIMP interaction. Our experiment differs from other projects (e.g. (4)) by its large size and its measurement techniques. The Zurich group is studying ways to efficiently collect and detect the VUV light to reach a detection threshold of 30 keV in argon and to suppress background from neutrons and electrons, in particular from the β-emitter ^{39}Ar isotope.

Charged particles lead to ionization and excitation of argon atoms forming excimers (Ar_2^+ and Ar_2^*) with the lowest singlet and the triplet excited states decaying into the ground state (two independent atoms) by VUV photon emission in a narrow band around 128 nm. Reabsorption by argon atoms is energetically suppressed. In liquid the singlet and triplet

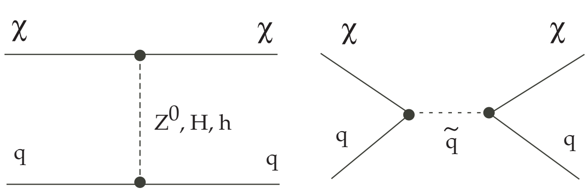

Figure 1.1: Feynman graphs of χ interactions with quarks in the nucleon.

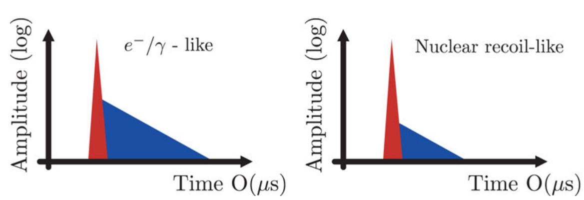

Figure 1.2: Scintillation time distribution in pure argon for minimum ionizing particles (left) and nuclear recoils (right).

[3] Visitor from Università degli Studi di Genova

states have decay times $\tau_1 \simeq 7$ ns and $\tau_2 \simeq 1.6$ μs, respectively (5). However, impurities such as water, air and CO_2 can absorb VUV light and reduce τ_2 (6; 7; 8). The population ratio singlet/triplet depends on ionization density (Fig. 1.2). For minimum ionizing projectiles such as e and γ the ratio is $\approx 1/2$, while for α's and nuclear recoils one finds a ratio of 4 – 5. Hence nuclear recoils from WIMPs populate mostly the fast decaying singlet state.

In addition, the ratio of scintillation to ionization yield is much higher for nuclear than for minimum ionizing particles. This is due to quick recombination which decreases the charge and enhances the luminescence. The higher ratio of light to charge production for nuclear recoils and the higher population of the fast decaying state can both be used to reduce background in WIMP searches.

A sketch of the ArDM detector, as it is now installed in building 182 at CERN, is shown in Fig. 1.3. The working principle is as follows: in liquid argon a WIMP collision leading to 30 keV nuclear recoils produces about 400 VUV (128 nm) photons, together with a few free electrons. The latter are drifted in a strong vertical electric field and are detected in the gas phase by a large electron multiplier (LEM) above the surface of the liquid, while the VUV scintillation light from argon is shifted into blue

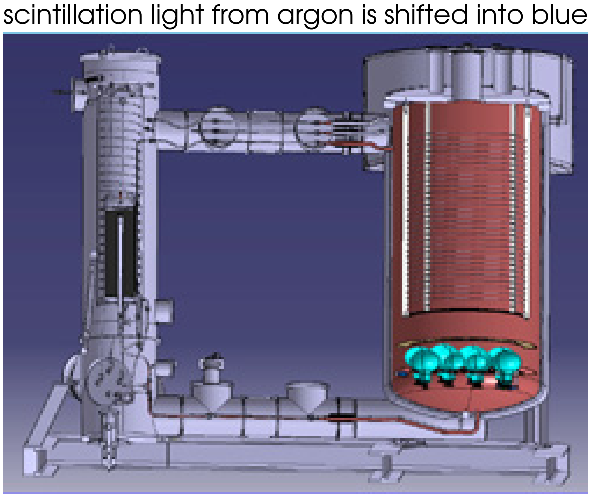

Figure 1.3: Sketch of the ArDM detector and its purification system on the left.

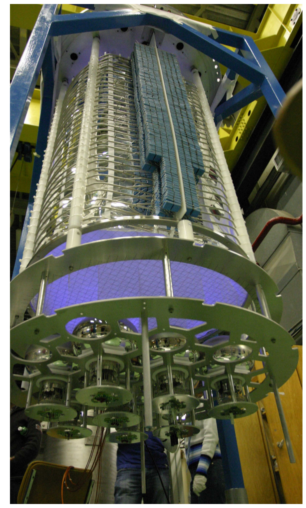

Figure 1.4: Photograph of the detector showing the Greinacher HV divider, the WLS foils and the photomultiplier support mechanics.

light by a wavelength shifter (WLS) and detected by cryogenic photomultipliers at the bottom of the vessel. Fifteen Tetratex sheets (120 $\times$ 25 cm^2) are coated with WLS to cover the cylindrical walls inside the electric field shaping rings. The light detection system consists of fourteen 8″ hemispherical photomultipliers (PMT, Hamamatsu R5912-MOD manufactured with Pt-underlays) at the bottom of the vessel. The PMT glass was coated with a thin WLS layer of a transparent tetraphenylbutadiene (TPB)-paraloid compound to increase the VUV light yield. The cryostat, the purification system, the Greinacher providing the 400 kV HV and the LEM are under the responsibility of ETHZ. Figure 1.4 shows the detector inside the vessel. More details can be found in previous annual reports and in ref. (9).

In parallel to the construction of ArDM we continued R&D activities in our laboratory at CERN to measure and optimize the light output and collection efficiency for charged particles and neutron background (10). Our aim is to achieve a detection efficiency of a few % (defined as the ratio of detected photoelectrons to emitted UV-photons) for the 128 nm fluorescence VUV-light generated in argon. An encouraging $\simeq$ 3% in a test chamber

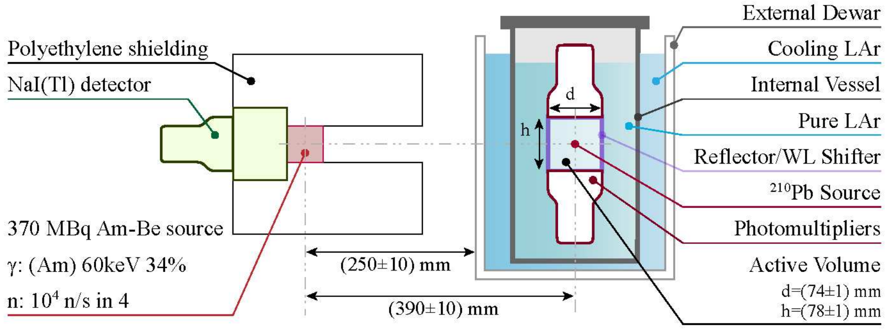

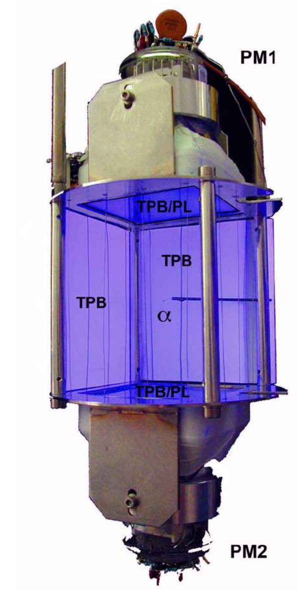

Figure 1.5:
Test cell to measure the light yield from various particles such as neutrons.

with similar geometry as the 1 t detector was achieved so far.

The setup (Fig. 1.5) is composed of two photomultipliers (Hamamatsu low temperature photomultipliers R6091-02MOD) facing an aluminum cylinder (height = 78 mm, diameter = 74 mm) containing liquid argon (Fig. 1.5, right). A wavelength shifter (1mg/cm^2 of TPB (11)) was evaporated on the side reflectors. This time we chose Tyvek from DuPont as substrate for the wavelength shifter to allow a better mechanical stability than the Tetratex used before. The cell was softly baked and pumped for two weeks to reach a pressure of $5 \cdot 10^{-7}$ mbar.

A ^{210}Pb radioactive source was held on a metal stick in the middle of the active volume. Measurements with neutrons were obtained by placing a 370 MBq Am-Be source next to the experimental setup (Fig. 1.5). The 5.4 MeV α's from americium are absorbed by beryllium producing 2 – 12 MeV neutrons (through the reaction ^{9}Be(α, n)^{12}C), 4.4 MeV γ's from the atomic level transition ^{12}C* $\rightarrow$^{12}C, and 60 keV photons from ^{241}Am decays. The source produced about 2$\cdot$10^4 n/s. It was contained in a high density polyethylene shielding block with two apertures, one for the neutrons, the second for the γ's to be detected in coincidence in a NaI(Tl) detector. The neutron flux at the target position was around 30 s^{-1}.

As pointed out before, heavily ionizing particles populate mostly the fast decaying singlet states. We therefore define the fraction r of fast ($<$ 50 ns) component to enhance nuclear recoils. The signal from recoil nuclei associated with neutrons is shown in Fig. 1.6

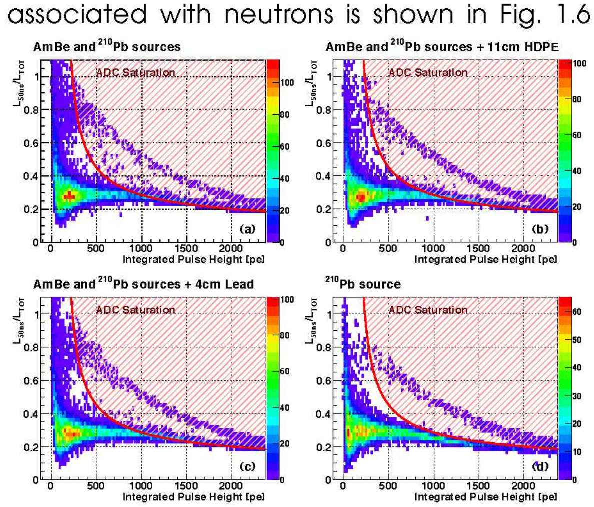

Figure 1.6: Ratio r = $L_{50\ ns}/L_{TOT}$ of fast to total amplitude for the Am-Be- and Pb-sources (top left), for the Am-Be-source shielded with polyethylene (top right), and with 4 cm of lead (bottom left). The contribution from the Pb-source alone is shown in the bottom right figure.

Figure 1.7: DD-neutron source.

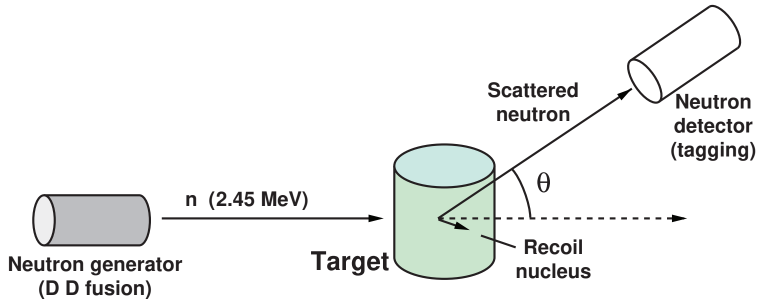

Figure 1.8: Neutron scattering experiment.

around r = 0.8. This can be proven by inserting a 11 cm thick polyethylene absorber, while a 4 cm lead sheet has no effect. The accumulation of events around $r = 0.3$ is due to recoil electrons, the diagonal band due to ADC saturation from α's.

Even small neutron fluxes around 1 MeV are potentially dangerous since the neutron-argon cross section is some 18 orders of magnitude larger than for WIMPs. It is therefore essential to investigate the response of the dark matter detector to neutrons as a function of recoil energy. A decisive advantage of monoenergetic neutrons over radioactive sources (such as Am-Be) is the known incident energy from which the energy transferred to the nucleus can be calculated by measuring the neutron elastic scattering angle.

We have therefore purchased a neutron source from NSD-Fusion GmbH (Fig. 1.7). The source will deliver monoenergetic 2.45 MeV neutrons (10^7 s^{-1}) from the reaction DD $\rightarrow$ $\mathrm{He}^3\mathrm{n}$. A sketch of the experiment we intend to perform is shown in Fig. 1.8. The collimated neutrons are scattered by a small liquid argon cell and detected at a given angle θ by a liquid scintillator counter. We have estimated that, after collimation and using a 10 cm argon cell, we would obtain around 5 counts/s in the neutron detector. The purpose of the experiment is thus to measure the light yield as a function of nuclear recoil energy which differs strongly from that of electronic excitation, due to quenching.

In the 1 t detector the probability for two or more neutron interactions is large enough to be measured precisely. This fraction can be measured with the DD-source and used to reduce the neutron background during WIMP searches, since WIMP interactions do not lead to multiple scattering events.

During 2008 the design of the DD-source was optimised in collaboration with the producer

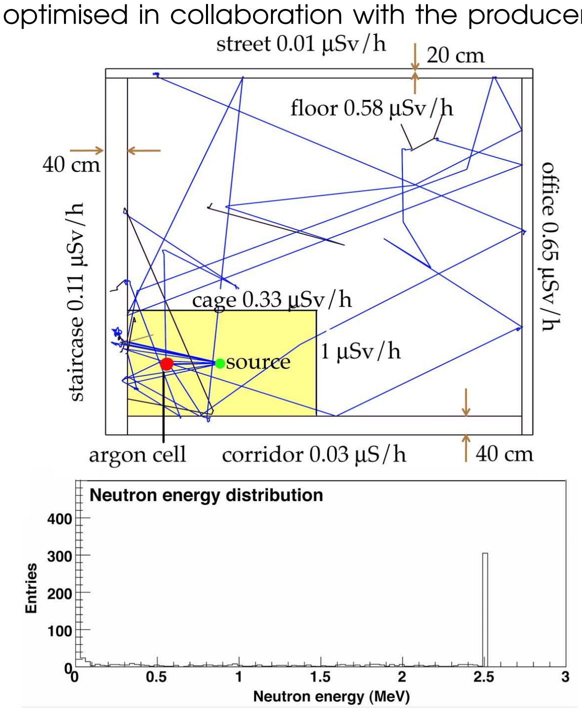

Figure 1.9: Top: predicted dose distribution in our laboratory with the neutron source in operation (the tolerated radiation dose is 2.5 μSv/h). The rays are typical neutron trajectories. Bottom: energy spectrum of neutrons at the argon cell.

to fulfill the safety and radiation requirements at CERN, so that the source could be operated in our laboratory close to our offices. We had also to provide our own GEANT4 simulation of the expected radiation levels in and around our laboratory (Fig. 1.9). The apparatus includes a real time ambient neutron dose monitoring system, and components for an operation interlock. A safety fence will be installed to avoid access to the radiation area during operation.

The neutron source, including its 27 mm thick aluminium housing, is surrounded by a 1 m long cylindrical shielding (50 cm of polyethylene). A hole, 10 cm in diameter, provides the collimated beam of neutrons. The neutron energy spectrum of the neutrons exiting the collimator is shown in Fig. 1.9, bottom. About 1.5% of the total neutron flux reaches the argon cell located at 1 m of the source. A fraction of 20% of the neutrons have the initial energy of 2.45 MeV, while 60% are thermalized.

Meanwhile we have purchased a liquid scintillator cell from SCIONIX with a photomultiplier coupled to a 3″ × 3″ cell filled with $C_6H_4(CH_3)_2$, which has a high H:C ratio of 1.21 (Fig. 1.10). This kind of detector is applicable for neutrons above 50 keV and gives information on the neutron energy, since the recoil proton is fully absorbed in the cell. Neutrons can also be separated from γ-events by pulse shape discrimination. Figures 1.11 and 1.12 show preliminary measurements with the Am-Be-source, displaying the normalized and averaged pulse shapes from electron and proton recoils, and the discrimination power between neutrons and photons.

As mentioned before, the purity in argon (and therefore the scintillation quality) can be monitored by measuring the lifetime of the slow component (6). We have therefore built another small liquid argon cell connected to the 1 t detector (Fig. 1.13). A 10 Bq ^{210}Pb source for the argon excitation is used to monitor the lifetime of the slow component every 10 s. We

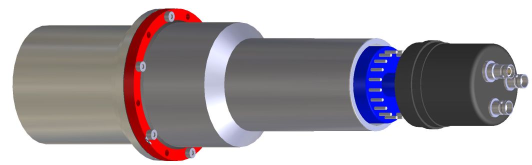

Figure 1.10:SCIONIX liquid scintillator cell.

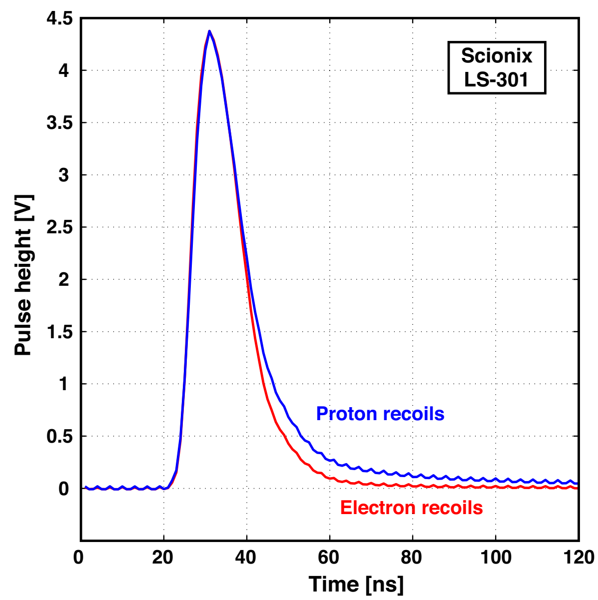

Figure 1.11: Normalized pulse shape from electron and proton recoils.

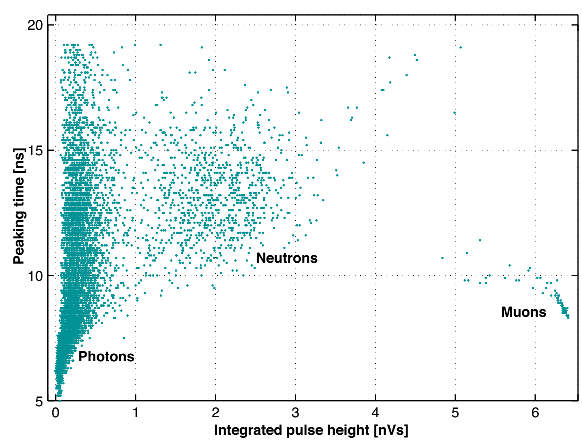

Figure 1.12: Peak-time vs. integrated pulse height measured with the Am-Be source.

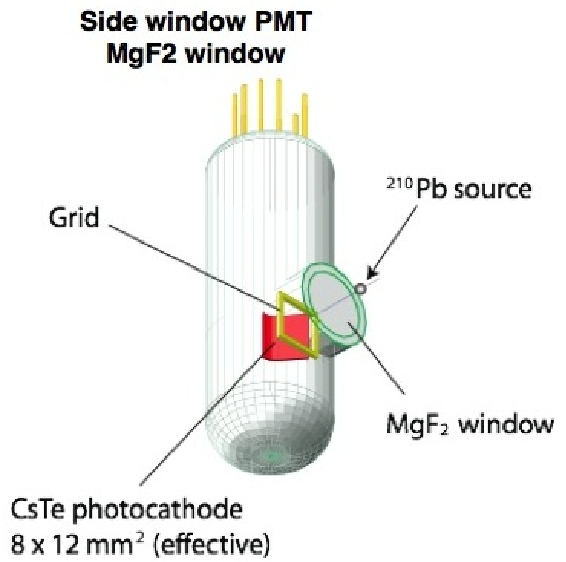

Figure 1.13: Sketch of the liquid argon purity monitor. A small PMT with VUV sensitive photocathode and a ^{210}Pb-source emitting both α and β are immersed in liquid argon.

use a small Hamamatsu R8486 PMT with MgF_2 window and CsTe photocathode which is directly sensitive to 128 μm VUV-photons (quantum efficiency 20%) and therefore does not require a WLS. The device (56 mm in diameter and 50 cm high) is rather compact.

The ArDM detector becomes operational in 2009 and will hopefully be moved to an underground location in 2011, following the extensive performance tests which can be most conveniently performed on the surface at CERN.

[1] For a review on dark matter searches see:
M. Drees and G. Gerbier, Phys. Lett. **B 667** (2008) 1.

[2] J. Angle *et al.*, (XENON-10 collaboration),
Phys. Rev. Lett. **100** (2008) 021303.

[3] Z. Ahmed *et al.* (CDMS collaboration),
Phys. Rev. Lett. **102** (2009) 011301.

[4] N. Ferrari *et al.*, (WARP collaboration),
J. Phys. Conf. Ser. **39** (2006) 111.

[5] A. Hitachi *et al.*, Phys. Rev. **B 27** (1983) 5279.

[6] C. Amsler *et al.*,
Journal of Instrumentation **3** (2008) P02001.

[7] A. Büchler, Bachelor Thesis, Universität Zürich (2006).

[8] M. Thomann, Bachelor Thesis, Universität Zürich (2008).

[9] V. Boccone, PhD thesis, Universität Zürich, in preparation:
V. Boccone, Proc. XIII Int. Conf. on Calorimetry in High Energy Physics, Pavia (2008), prep. arXiv:0810.4490v1.

[10] V. Boccone *et al.* (ArDM Collaboration)
prep. arXiv:0904.0246v1, submitted to Journal of Instrumentation.

[11] H. Cabrera, Master Thesis, Universität Zürich (2007).

2 Search for Cold Dark Matter with CDMS-II

S. Arrenberg, L. Baudis, T. Bruch

in collaboration with: Department of Physics, Brown University, Department of Physics, California Institute of Technology, Department of Physics, Case Western Reserve University, Fermi National Accelerator Laboratory, Lawrence Berkeley National Laboratory, Massachusetts Institute of Technology, Department of Physics, Queen's University, Department of Physics, Santa Clara University, Department of Physics, Stanford University, Department of Physics, Syracuse University, Department of Physics, University of California, Berkeley, Department of Physics, University of California, Santa Barbara, Departments of Physics & Elec. Engr., University of Colorado Denver, Department of Physics, University of Florida, Gainesville, School of Physics & Astronomy, University of Minnesota, Minneapolis.

(CDMS-II Collaboration)

The Cryogenic Dark Matter Search (CDMS) experiment uses high-purity Ge (250 g) and Si (100 g) crystals kept at ∼20 mK to search for dark matter particles. Both phonons and electron-hole pairs are collected after a particle interacts in a crystal. Nuclear recoils produce less electron-ion pairs than electron recoils, thus the ionization yield, defined as $y \equiv E_{charge}/E_{recoil}$, is much smaller for nuclear recoils ($y \sim 0.3$ for Ge and ~ 0.25 for Si) than for electron recoils ($y = 1$) of the same energy. It provides the technique to reject the electron-recoil events which produce most of the background.

CDMS-II operates 5 towers (19 Ge and 11 Si detectors) with 4.5 kg of Ge and 1.1 kg of Si, in stable WIMP search mode since October 2006. Results from the data acquired between October 2006 and July 2007 (Runs 123-124), yielding an exposure of 121.3 kg d in Ge, have recently been published (1). A blind analysis resulted in zero observed events, the deduced upper limit on WIMP-nucleon spin-independent cross section is 4.6×10^{-44}cm^2 for a WIMP mass of 60 GeV/c^2 (1). It improves upon the sensitivity of XENON10 for WIMP masses above 42 GeV/c^2, providing the current best sensitivity above this mass.

Currently, the data from Runs 125-128, yielding an exposure above 400 kg d in Ge are under analysis. Our group was strongly involved in the analysis of the CDMS data Runs 123-124, and we are now focusing on the Runs 125-128. We have developed and are testing data reconstruction and quality cuts, as well as cuts regarding the event selection and topology. As examples, we mention the quality of the charge and phonon pulse reconstruction, the tests of detector behavior with time, the single-scatter cut, the charge threshold and the electron recoil band cuts. The pre-processing of Run 125-128 data is finished and these cuts are now applied and tested on calibration, as well as non-blind WIMP search data. The release of new results, with an expected sensitivity is $\sim 2 \times 10^{-44}$cm^2, is planned for summer 2009.

2.1 Search for solar axions with CDMS

Originally designed for WIMP searches, the CDMS-II experiment can also detect solar axions by Primakov conversion to photons. The Bragg condition for X-ray momentum transfer in a crystal allows for coherent amplification of the Primakov process. Since the orientation of the crystal lattice with respect to the Sun changes

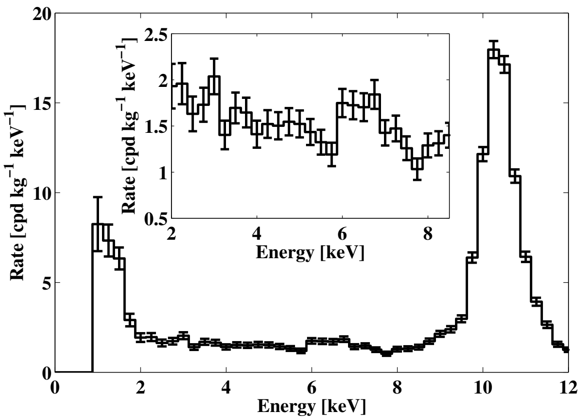

Figure 2.1: Co-added, efficiency corrected low energy spectrum of the Ge detectors considered in this analysis. The inset shows an enlargement of the spectrum in the analysis window, taken to be 2 to 8.5 keV.

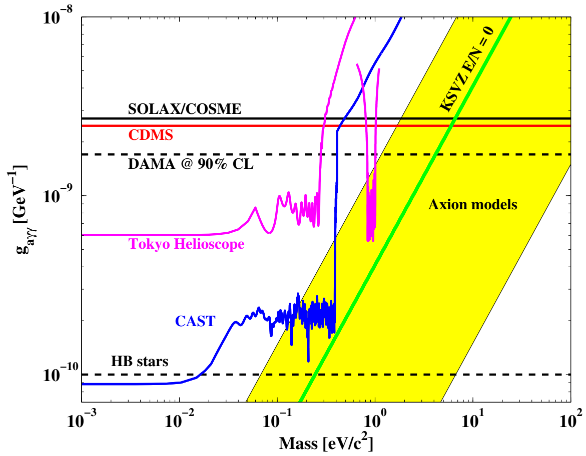

Figure 2.2: Comparison of the 95% C.L. upper limit on $g_{a\gamma\gamma}$ achieved in this analysis (red/solid) with other crystal search experiments (SOLAX/COSME [4; 5] (black/solid) and DAMA (upper black/dashed) [6]) and helioscopes (Tokyo helioscope (magenta/solid) [7] and CAST (blue/solid) [2]). The constraint from Horizontal Branch stars (lower black/dashed) is also shown [8].

with daytime an unique pattern of solar axion conversions is expected. The low background of $\sim$1.5 events/(kg d keV) (see Fig. 2.1)

and knowledge of the exact orientation of all three crystal axes with respect to the Sun make the CDMS-II experiment very sensitive to solar axions and, in contrast to helioscopes, the high mass region $<$ 1 keV can be probed effectively. The result of an analysis of 289 kg-days of exposure resulted in a null observation of solar axion conversion. The analysis sets an upper limit on the axion photon coupling constant of $g_{a\gamma\gamma} < 2.6 \times 10^{-9}$ GeV^{-1} at a 95% confidence level (Fig. 2.2). It inspires the prospects that future large crystal arrays such as SuperCDMS and GERDA may provide competitive sensitivity on the photon-axion coupling constant for $g_{a\gamma\gamma} < 10^{-9}$ GeV^{-1} in the high mass region not easily accessible to helioscopes such as the CAST (2) experiment. A paper with the results has been submitted to PRL (3).

2.2 Effects of the Milky Way's dark matter disk on direct and indirect detection experiments

Recent simulation of hierarchical structure formation including the effect of baryons revealed that a thick dark matter disk forms in galaxies, along with the dark matter halo (9; 10). The dark disk has a density of ρ_d/ρ_h = 0.25 - 1.5 where ρ_h = 0.3 GeV/cm^3 and the kinematics are predicted to follow the Milky Way's stellar thick disk. At the solar neighborhood, this gives a rotation lag of v$_{lag}$ = 40 - 50 km/s with respect to the local circular velocity, and a dispersion of $\sigma \simeq$ 40 - 60 km/s. These velocities are significantly lower than in the standard halo model with v = 220 km/s and σ = 270 km/s. In collaboration with the group of Prof. G. Lake in the Theory Institute at UZH, we studied the impact of the low velocity of particles in the dark disk on direct and indirect dark matter detection.

For direct detection we find that the dark disk boosts the rates at low recoil energies, depending on the WIMP mass. As an example, for $M_W \gtrsim 50$ GeV, recoil energies of 5 - 20 keV and $\rho_d/\rho_h \leq 1$, the rate increases by factors up to 2.4 for Ge and 3 for Xe targets (Fig. 2.3).

Comparing this with the rates at higher energies will constrain the mass of the dark matter particle (M_W), particularly for $M_W > 100$ GeV. The dark disk also has a different annual modulation phase than the dark halo, while the relative amplitude of the two components varies with recoil energy and M_W. The increased expected dark matter flux improves the constraints on the WIMP cross section from current experiments. For likely dark disk properties ($\rho_d/\rho_h \leq 1$), the constraints for pure spin-independent coupling improve by up to a factor of 1.4 for CDMS-II, and 3.5 for XENON10. This work has been published in the Astrophysical Journal (11).

For neutrino telescopes, we find that the dark disk significantly boosts the capture rate of dark matter particles in the Sun and Earth as compared to the standard halo model (SHM). This increase owes to the higher phase space density at low velocities in the dark disk. For the Sun, the expected muon flux from the dark disk with $\rho_d/\rho_h = 1$ is increased by one order of magnitude relative to a pure SHM-generated flux. For the Earth — where WIMP capture and annihilation are not in equilibrium — the increase in the muon flux is two to three orders of magnitude, although this depends sensitively on the distribution function of the dark disk. Fig. 2.4 shows the summed muon flux at the Earth from the SHM and the dark disk as a function of the WIMP mass from neutrinos originated in the Sun, along with current experimental constraints and expected sensitivities for neutrino telescopes. The main results of these studies have been published in Physics Letters B (12). Our next goal is to quantify the impact of the dark disk on directional dark matter detectors.

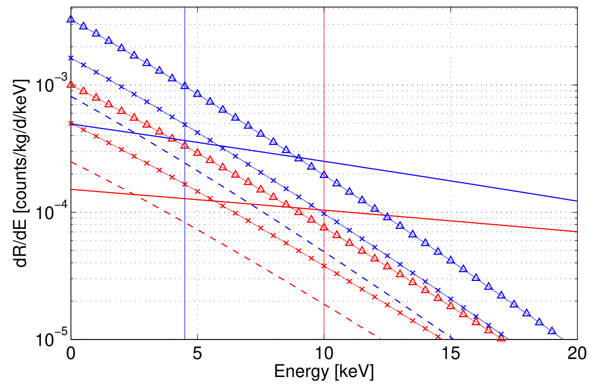

Figure 2.3: Differential recoil rates for Ge (red) and Xe (blue) targets, for WIMPs with $M_W = 100$ GeV and a cross section of 10^{-8} pb in the SHM (solid line) and the dark disk. Three different values of ρ_d/ρ_h (0.5 dashed, 1 $\times$ and 2 $\triangle$) are shown. Vertical lines mark current experiment thresholds: XENON10 (blue) using a Xe and CDMS-II (red) using a Ge target.

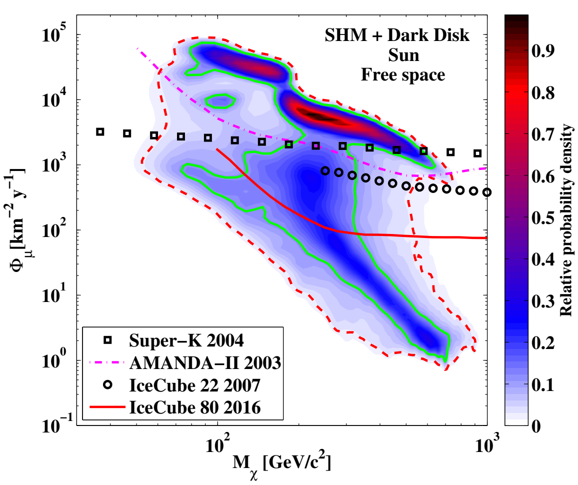

Figure 2.4: Summed muon flux at the Earth from the SHM and the dark disk as a function of the WIMP mass from neutrinos originated in the Sun. The closed contours show – 95% (red/dashed) and 68% (green/solid) – of the probability density of CMSSM models consistent with both astrophysical and collider constraints. The color-bar gives the relative probability density. Current experimental constraints on the muon flux from the Earth and Sun from Super-Kamiokande [13], AMANDA-II [14; 15] and IceCube22 [16] and the prediction for IceCube80 are also shown.

2.3 Analysis for inelastic dark matter and simulation of the WIMP velocity distribution

In direct search experiments dark matter particles in the galactic halo are usually described by a Maxwellian velocity distribution. This follows from the assumption that the dark halo is an isothermal sphere of collisionless particles. Another approach is to use the local velocity distribution of particles obtained from numerical simulations of Milky Way type halos. We are collaborating with the group of Prof. B. Moore in the Theory Institute to investigate the impact of velocity distributions obtained from the analysis of dark matter simulations on direct detection experiments. As shown in Fig. 2.5, the velocity distributions of dark matter particles tend to be broader and slightly suppressed at the peak, compared to the Maxwellian distribution. However, the impact on current limits from direct detection experiments is small, confirming that so far the Maxwellian approximation for the velocity distribution is a valid choice. This work is in progress, some of the goals being to study how many events we would need in an experiment in order to distinguish between different velocity distributions of WIMPs.

The observation of an annual modulation in the event rate by the DAMA collaboration was confirmed by the new DAMA/LIBRA results (17). The interpretation as a dark matter signal coming from standard WIMPs is in severe tension with results from all other direct detection experiments (18), as well as with indirect detection limits from Super-Kamiokande (19). One model which would allow to reconcile DAMA/LIBRA with other searches is the inelastic dark matter scenario (20). In this scenario, WIMP-nucleon scattering occurs only via inelastic scattering with the dark matter particle transiting into an excited state. Thus, only WIMPs with sufficient energy to up-scatter into the excited state can scatter off nuclei in the detector. The mass splitting between the WIMP and its excited state is considered to be a free parameter; in order to explain the DAMA/LIBRA results, the splitting needs to be around 120 keV (20). This model is still in agreement with all experiments, because it eliminates low energy events, the signal peaking at higher energies (for instance, at 70 keV in Ge and at 35 keV in I and Xe), a region which is often not analyzed for WIMP interactions. Our goal is to analyze the new CDMS data with respect to this model, including also the velocity distributions obtained from dark matter simulations discussed above. Figure 2.6 shows differential

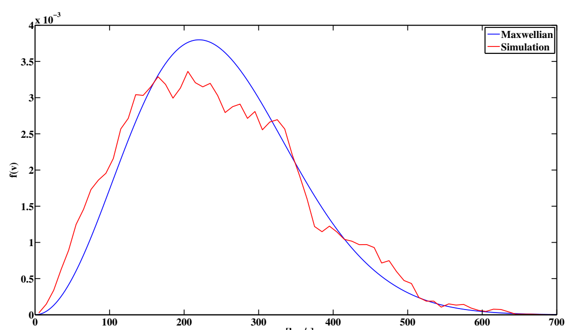

Figure 2.5:
Comparison of the velocity distribution from a particle sample from a simulation, 8 kpc away from the galactic center, with a Maxwellian distribution.

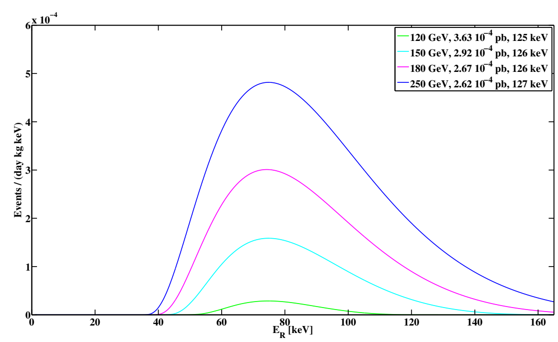

Figure 2.6: Differential event rates in the inelastic dark matter scenario. The numbers in the legend correspond to WIMP mass, WIMP-nucleon cross section and mass splitting, respectively.

rates for different WIMP masses, splittings and cross sections which are consistent with all experiments (20). In the standard WIMP scenario, the rates would be exponentially decreasing over the entire energy range.

[1] Z. Ahmed et al. (CDMS Collaboration), Phys. Rev. Lett. **102**, 011301 (2009).

[2] S. Andriamonje et al., J. Cosmol. Astropart. Phys. **04**, 010 (2007), E. Arik et al., arXiv:0810.4482.

[3] Z. Ahmed et al. (CDMS Collaboration), submitted to Phys. Rev. Lett., arXiv:0902.4693v1 (2009).

[4] F. T. Avigone et al., Phys. Rev. Lett. **81**, 5068 (1998).

[5] A. Morales et al., Astropart. Phys. **16**, 325 (2002).

[6] R. Bernabei et al., Phys. Lett. B **515**, 6 (2001).

[7] M. Minowa et al., Phys. Lett. B **668**, 93 (2008).

[8] G. G. Raffelt, Stars as Laboratories for Fundamental Physics, The University of Chicago Press (1996).

[9] J. I. Read, G. Lake, O. Agertz, V. P. Debattista, MNRAS **389**, 1041 (2008).

[10] J. I. Read, L. Mayer, A. M. Brooks, F. Governato, G. Lake, to be published in MNRAS, arXiv:0902.0009v1 (2009).

[11] T. Bruch, J. I. Read, L. Baudis, G. Lake, Astrophysical Journal **696**, 920-923 (2009).

[12] T. Bruch, A. H. G. Peter, J. I. Read, L. Baudis, G. Lake, Physics Letters B **674**, 250-256 (2009).

[13] S. Desai et al., Phys. Rev. D **20**, 083523 (2004).

[14] T. DeYoung et al. Journal of Physics: Conference Series **136**, 022046 (2008).

[15] A. Achterberg et al., Astropart. Phys. **26** 129 (2006).

[16] A. Karle et al. arXiv:0812.3981v1 (2008).

[17] R. Bernabei et al., Eur. Phys. J. C **56**, 333 (2008).

[18] Savage, Gelmini, Gondolo, Freese, arXiv:0808.3607v1 (2008), M. Fairbairn, T. Schwetz, arXiv:0808.0704v1 (2008), Aalseth et al., Phys. Rev. Lett **101** (2008), Behnke, Collar et al., Science **319** (2008).

[19] D. Hooper, F. Petriello, K. Zurek and M. Kamionkowski, arXiv:0808.246v4 (2008).

[20] S. Chang, G.D. Kribs, D. Tucker-Smith and N. Weiner, Phys. Rev. D **79**, 043513 (2009).

3 Search for the Neutrinoless Double Beta Decay with GERDA

L. Baudis, A. Ferella, F. Froborg, R. Santorelli, M. Tarka

in collaboration with:
INFN Laboratori Nazionali del Gran Sasso LNGS, Institute of Physics, Jagellonian University, Cracow, Institut für Kern- und Teilchenphysik Technische Universität Dresden, Joint Institute for Nuclear Research, Dubna, Institute for Reference Materials and Measurements, Geel, Max Planck Institut für Kernphysik, Heidelberg, Germany, Università di Milano Bicocca e INFN Milano, Milano, Institute for Nuclear Research of the Russian Academy of Sciences, Institute for Theoretical and Experimental Physics, Moscow, Russian Research Center Kurchatov Institute, Max-Planck-Institut für Physik, München, Dipartimento di Fisica dell'Università di Padova e INFN, Physikalisches Institut, Eberhard Karls Universität Tübingen

(GERDA Collaboration)

Neutrino oscillation experiments have established that neutrinos have non-zero masses, with a lower limit for one of the masses at $\sqrt{\Delta m^2_{atm}} \simeq$0.05 eV. However, these experiments can not determine the absolute mass scale and the charge conjugation properties of these particles. The observation of neutrinoless double beta ($0\nu\beta\beta$) decay would prove that neutrinos are Majorana particles, that lepton number is violated in Nature and would give us information on the so-called effective Majorana neutrino mass, m_{ee} (1). Current experimental limits on m_{ee} are of the order $m_{ee} \leq 0.3 - 1.0$ eV, with the most stringent upper limits from ^{76}Ge coming from the Heidelberg-Moscow (2) and IGEX (3) experiments.

GERDA is an experiment to search for the $0\nu\beta\beta$ decay in enriched ^{76}Ge detectors in Hall A of LNGS. The aim of GERDA Phase I and II is to reach a sensitivity for m_{ee} of 270 meV and 110 meV, respectively. This is achieved by operating bare HPGe crystals in a large volume (70 m^3) of liquid argon (LAr), which serves as a passive shield (in Phase I) against the external radioactivity. The liquid argon is surrounded by a water shield instrumented with PMTs.

GERDA is under construction at LNGS: the double walled stainless steel LAr cryostat, the water Cerenkov shield, the superstructure around the outer tank and the electrical systems have been installed. Figure 3.1 shows the water tank for the Cerenkov shield along the superstructure during its installation at LNGS. Currently the clean room on top of the superstructure is under construction. Next the lock system used to insert the crystals with their holders into the LAr and the gas handling system will be installed. The detector commissioning is planned for fall 2009, after which the science run will start.

Figure 3.1: The GERDA water tank for the Cerenkov shield and the superstructure during its installation.

GERDA Phase I will operate 17.9 kg of existing enriched ^{76}Ge detectors in LAr. These detectors are currently at LNGS, where they have successfully been tested in more than 40 cooling cycles in LAr in the GERDA Detector Lab. The cryostat and infrastructure being built for Phase I will also be used in Phase II. An additional 14 (25 for BEGe detectors) enriched HPGe detectors are planned for this second phase. The baseline design so far has been to produce highly segmented n-type detectors. Based on first, promising tests at the MPIK Heidelberg of p-type, broad-energy, point-contact Ge detectors (BEGe), it was realized that these detectors could be a viable alternative to segmented detectors for GERDA phase II. The final decision will be based on overall performance of both detector types and on costs.

At present, the GERDA collaboration is in the possession of 37.5 kg of enriched Ge material (in the form of GeO_2), with an additional 20 kg of enriched material needed. This material will be cleaned by the process of polyzone refinement at PPM Pure Metals in Germany. After this step, crystals will be grown at the Institut fuer Kristallzuechtung (IKZ) Berlin (until end of 2009, the period including test runs with natural, and depleted Ge) in the case of the segmented n-type detectors, and at Canberra USA in the case of BEGe detectors. The actual detectors will be produced at Canberra (until end 2010). All these steps will occur under close collaboration with the GERDA collaborating Institutions, including UZH.

3.1 GERDA calibration system

For GERDA Phase I, our group is responsible for the calibration system (we are leading the Calibrations Task Group in the collaboration): calibration sources, collimators, hardware for insertion/parking in the LAr cryostat, Monte Carlo simulations of possible configurations, source strengths and efficiency of pulse shape discrimination, as well as long-term maintenance and data analysis. We have simulated various source and collimator configurations using the Geant4 based framework MaGe (4) which was designed for the GERDA (5) and Majorana (6) projects. The scope was to determine which sources will be used, in which configuration, position and strength, and how often. The sources will be employed to determine and monitor the stability of the energy scale and resolution of the detectors with time, as well as to establish and monitor the efficiency of the pulse shape analysis method which will be used to distinguish single-site interactions (as expected from a double beta decay event) from multiple scatters (for instance, multiple Compton scatters, or neutron interactions). The best source in terms of energy range is ^{228}Th, with $T_{1/2}$=1.9 yr, providing several lines around the region of interest, as well as a population of single-site events with the double-escape peak of the 2615 keV ^{208}Tl line. Our simulations show that we will need three sources in different positions around the detector arrays, each of about 50 kBq. Figure 3.2 shows ^{228}Th calibration spectra of two detectors in the Phase I array, the detector with the highest and lowest statistics in one layer, respectively. We are developing a dynamic data base to store the calibration parameters after each run and to feed them into the data processing software.

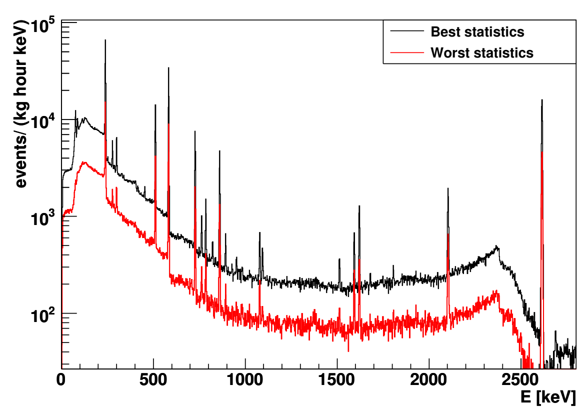

Figure 3.2: ^{228}**Th calibration spectra of two detectors in the Phase I array, the detector with the highest and lowest statistics in one layer, respectively.**

Since the sources will be parked inside the LAr cryostat, a proper shielding by the source collimator is required. We have studied pure tungsten, a W-compound (Densimet, 92% W, rest is Ni and Fe) and pure tantalum. All offer sufficient shielding against the source activity in the parking position, the pure tungsten is however harder to machine, being brittle. So far we have screened the pure tungsten and the Densimet with Gator, obtaining the activities for U/Th/K/Co of 300/30/8.1/40 mBq/kg and 180/70/7/57 mBq/kg, respectively. We are currently screening the tantalum and will then decide which material to use (any of these will give a background which is at least a factor thousand below the background from the source itself, and thus negligible).

A problem with custom-made ^{228}Th sources is the neutron yield via (α,n) reactions in the ceramic pallet ($NaAlSiO_2$) containing the radioactive element. A calculation of the n-spectra and yields for our required source activities gave a neutron rate of about 1.9 n/s for a 50 kBq source, with a mean energy of 1.5 MeV. Subsequent neutron transport simulations in MaGe show that the background in the 1.5-2.5 MeV region is about 1.6×10^{-3} events/(kg yr keV) for all 3 sources, which is higher than the GERDA phase II goal of 1×10^{-3} events/(kg yr keV). We have thus started a collaboration with PSI to fabricate sources embedded in gold, which has a 9.9 MeV threshold for (α,n) reactions, much higher than the light materials in ceramics and above the maximum α energy of the ^{228}Th chain. A solution of ThCl in 1 M HCl will be heated and then mixed with melted gold, yielding a pure Th source embedded in Au. This procedure is first being tested with a lower activity (20 kBq) solution. The resulting source will be tested in a mock-up collimator (see Fig. 3.3) immersed in our LAr cryostat containing a small HPGe detector (see next Section) in our lab at UZH.

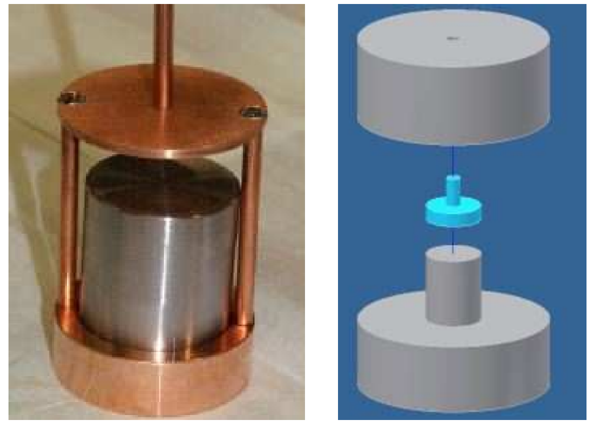

Figure 3.3:
Mock-up W collimator for testing the GERDA calibration source at UZH and a possible source/collimator configuration considered for the final design.

3.2 R&D for GERDA Phase II detectors

GERDA Phase II will use an additional 14 (25 for BEGe) enriched HPGe detectors. Before these detectors can be manufactured, it is essential to test all the steps in the fabrication process using non-enriched Ge material. Two options are currently being considered by the collaboration: 18-fold segmented n-type detectors, or non-segmented, p-type, broad-energy, point-contact Ge detectors (BEGe). Long-term tests of a segmented detector at MPI Munich has yielded an energy resolution of the single segments between 2 keV-3 keV (FWHM) at the 1332 keV ^{60}Co line (7). Motivated by (8), first studies with a 800 g BEGe detector at MPIK Heidelberg were performed, showing a good discrimination of single-site versus multiple-site interactions. This is achieved through a gradient in the impurity concentration level, yielding an electric field distribution which enhances the difference in charge carrier drift times depending on the interaction site (8). This type of detector is thus a viable, possibly cheaper and lower-background alternative for GERDA Phase II detectors. We have engaged in an R&D program together with a few of the GERDA institutions (MPIK, Tuebingen, Milano and Geel) and

Figure 3.4: Our n-type HPGe detector before tests in liquid argon.

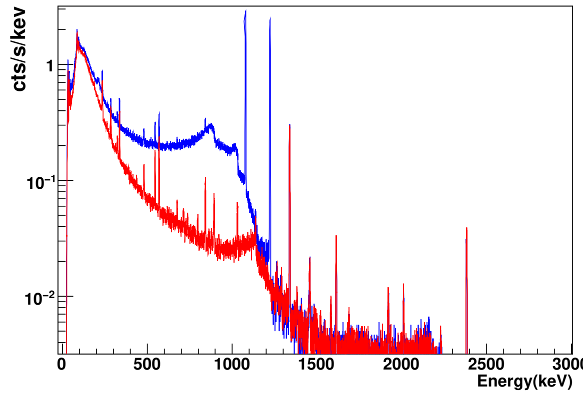

Figure 3.5: Calibration spectrum with a ^{60}Co source (blue) and background spectrum (red) in the UZH lab. The energy resolution of the detector is 2.0 keV at the 1.3 MeV ^{60}Co line.

Canberra USA on the production and tests of BEGe detectors from the available enriched Ge material, with a high yield and at reasonable costs. We will be responsible for the zone refinement and crystal pulling steps (together with Milano), and for the tests of one BEGe detector (3 will be fabricated in this step). All these steps will be tested with depleted Ge material first; 20 kg of this material will be delivered to Canberra in June 2009.

We have also committed to test one of the n-type detectors produced by Canberra France from non-enriched Ge material, in order to verify the quality of crystals from the Institut for Kristallzuechtung (IKZ) which is responsible for pulling crystals for the n-type detectors. This will allow us to directly compare the two type of detectors in the same facility.

We have built a detector test facility, in which we operate a commercial, n-type, naked HPGe-crystal (~300 g) immersed in liquid argon. The aim of this first step was to develop the infrastructure for the detector storage in vacuum, to test the cooling and warming-up procedures avoiding any condensation on the detector surfaces, to test low-noise electronics for detector operation and to validate the Monte Carlo simulations of calibration sources. A picture of our HPGe detector and a calibration spectrum with a ^{60}Co source is shown in Figs. 3.4 and 3.5.

[1] S. R. Elliott and P. Vogel, Ann. Rev. Nucl. Part. Sci. **52**, 115 (2002).

[2] L. Baudis et al. (Heidelberg-Moscow collaboration), Phys. Rev. Lett. **83**, 41 (1999).

[3] I.G. Irastorza et al. (IGEX Collaboration), Phys. Rev. D **65**, 092007 (2002).

[4] Y.-D. Chan et al., arXiv:0802.0860v1 [nucl-ex] (2008).

[5] I. Abt et al, GERDA: The GERmanium Detector Array for the search of neutrinoless $\beta\beta$ decays of ^{76}Ge at LNGS, Proposal to LNGS P38/04, September 2004.

[6] C.E. Aalseth et al. (Majorana Collaboration), Phys. Atom. Nucl. **67** 2002 (2004).

[7] I. Abt et al., Nucl. Instrum. Meth. **A577**, 574-584 (2007).1

[8] Barbeau et al., JCAP **0709**, 009 (2007).

4 Search for Cold Dark Matter Particles with XENON

A. Askin, L. Baudis, A. Behrens, A. Ferella, M. Haffke, A. Kish, A. Manalaysay,
T. Marrodan-Undagoitia, R. Santorelli, E. Tziaferi

in collaboration with:
Columbia, INFN, University of Coimbra, University of Münster, Rice, Subatech, Waseda

(XENON Collaboration)

The goal of XENON (1) is to search for interactions of dark matter particles in liquid xenon. Weakly Interactive Massive Particles (WIMPs) represent a generic class of dark matter candidates (2; 3). Their density in the galactic halo may allow them to be detected in laboratory experiments by looking for the nuclear recoils produced in elastic scattering of WIMPs off nuclei (4). A WIMP with a typical mass between a few GeV and 1 TeV will deposit a recoil energy below 100 keV in a terrestrial detector. The expected rates are determined by the WIMP-nucleus cross section and by their density and velocity distribution in the vicinity of the solar system (3). Direct-detection experiments are beginning to significantly constrain the WIMP-nucleon scattering cross section and, for the first time, start to probe the parameter space of 'Beyond Standard Model' particle physics models (5; 6; 8; 9). Figures 4.1 and 4.2 compare the current best limits from direct detection experiments with predictions from supersymmetry, for spin-independent and spin-dependent coupling, respectively.

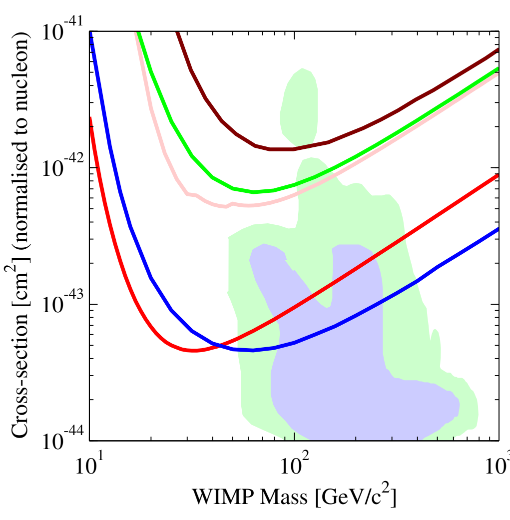

Figure 4.1: Current upper limits for the WIMP-nucleon, spin-independent, cross section as a function of the WIMP mass, the best limits being provided by the XENON10 [5] (red line) and CDMS [6] (blue line) experiments. The predicted region for the neutralino as a dark matter candidate in the constrained MSSM is shown as the green (95% CL) and blue (68% CL) shaded regions [7].

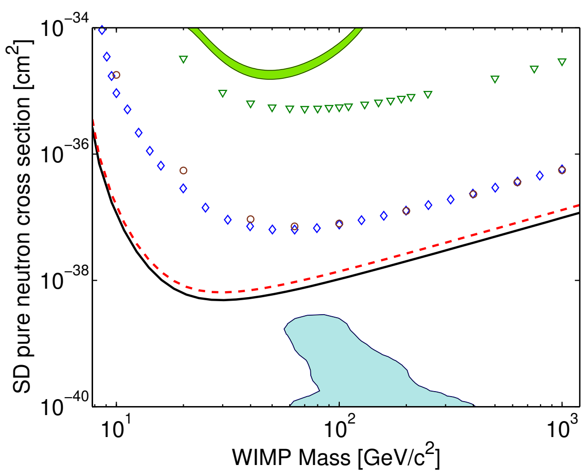

Figure 4.2:
Solid curve: XENON10 combined 90% CL exclusion limits for ^{129}Xe and ^{131}Xe for pure neutron couplings.
Dashed curve: as above with alternate form factor.
Diamonds: CDMS; circles: ZEPLIN-II; triangles: KIMS.
Green band: DAMA evidence region for standard WIMP nuclear recoils and dark halo parameters.
Blue region: prediction for the neutralino in the constrained minimal supersymmetric model.
From Ref. [8].

4.1 XENON100 and its upgrade

After the successful operation of the XENON10 experiment (5; 8), the XENON Collaboration has built a 170 kg liquid xenon time projection chamber (TPC), which is currently under commissioning at the Gran Sasso Laboratory (LNGS) in an improved XENON10 shield (10). The detector uses two arrays of low radioactive, UV-sensitive photomultipliers (Hamamatsu R8520-06-Al 1″ square PMTs) to detect the prompt and proportional light signals induced by particles interacting in the 70 kg sensitive xenon region. The remaining 100 kg viewed by two rings of PMTs are used as an active shield against background. The bottom array of 80 PMTs located below the cathode and fully immersed in LXe, primarily detects the prompt light signal. The 98 PMTs of the top array located in the cold gas above the liquid, detect the proportional light signal which created by the collision of extracted electrons with Xe gas phase.

While the fiducial mass of XENON100 is increased by a factor of 10 with respect to XENON10, the background is lower by a factor of $\sim$100. This is achieved by selecting ultra-low-background materials, by moving cryogenic devices and high-voltage feedthroughs outside the shield, by using the active LXe shield, by purifying the LXe from radioactive ^{85}Kr and by an improved passive shield (5 cm of ultra-pure Cu and 20 cm water, both installed by our group). Data-taking starts in 2009 and after a raw exposure of 6000 kg days the WIMP-nucleon cross sections will have been probed down to $\sim 2\times10^{-45}$cm^2 at a 100 GeV WIMP mass.

During the accumulation of statistics with XENON100, we are planning to start construction of an upgraded detector. The goal is to further reduce the background with a cryostat made of copper and with new photodetectors, Quartz Photon Intensifying Detectors (QUPIDs) which have been developed by Hamamatsu for operation in LXe. They are made of an avalanche photo-diode kept at 0V and a photo-cathode deposited on a quartz window, kept at -10 kV. We have shown that this new photodetector has an ultra low radioactivity (see Table 4.1) and we are planning to test its single photon counting capability, as well as its quantum efficiency by operating it in LXe in our small test chamber at UZH.

The current bottom R8520 PMT array will be replaced with 19 QUPIDs. We will remove most of the activity from the stainless steel (SS) cryostat by replacing it with a low-background, oxygen free copper (OFHC) one. As the activity of the top PMTs will dominate the background, we will double the drift length from current 30 cm to 60 cm. The activity from the top cryostat assembly, made of the lowest activity SS we have identified so far, will add negligible background compared to the top PMTs. A cross-sectional view of the proposed detector mounted inside the upgraded shield is shown in Fig. 4.3.

The dark matter search with the upgraded XENON100 would start in 2011. With two years of data and a raw background rate below 4×10^{-4} events/(kg·d·keV), the upgraded XENON100 could reach a sensitivity of $\sim 2\times10^{-46}$cm^2, which is about a factor of 100 beyond the current best limits.

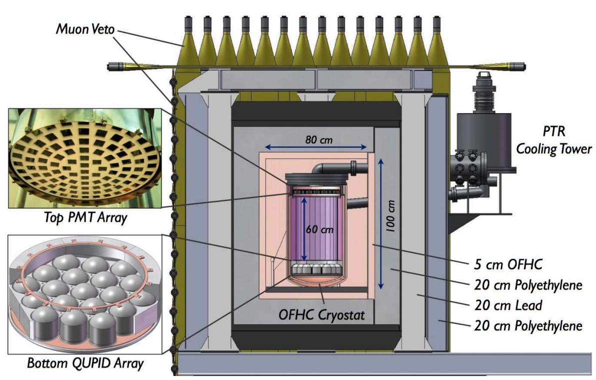

Figure 4.3: The upgraded XENON100 with 19 QUPID sensors on the bottom and an OFHC Cu cryostat in the improved shield, which includes a muon veto.

The main activities of our group are testing and calibrations of XENON100 PMTs, position reconstruction algorithms based on neural networks, material screening with the HPGe detector, Monte Carlo simulations of backgrounds and light-collection efficiencies, energy calibrations with various sources, production of the inner TPC structures, commissioning, operations, data processing and analysis, as well as R&D for the XENON100 Upgrade and XENON1t.

4.1.1 Calibration and Monitoring of the PMTs

We have the responsibility of the detailed characterization of the 242 individual PMT (Hamamatsu R8520) channels of the XENON100 detector. The light calibration involves the measurement of the absolute gain, as well as the resolution on single photoelectron, the peak-to-valley and signal-to-noise ratios, and the monitoring of the PMT responses over time. An external clock generator is used to synchronize an LED driver (which sends pulses to two InGaN/blue LEDs in an external LED box) and the data acquisition system. The light from the LEDs is transferred via an optical fiber to the feedthroughs on the detector, where it is split in order to achieve uniform illumination of all photomultiplier tubes: 4 fibers are used to calibrate top and bottom PMT arrays in the target volume, and 6 fibers for the PMTs in the veto volume. The analysis procedure identifies a PMT pulse, integrates the signal event by event, plots the spectrum for each PMT, discriminates noise and then computes the gain and other relevant parameters. A typical single photoelectron response of the PMTs being operated in XENON100 and a map of the bottom PMT array spectra is shown in Fig. 4.4. The results of the regularly performed light calibrations are written into the MySQL database, created and maintained by our group. The values are accessible by the analysis software and used for the data processing. The database also contains location and history of each phototube, quantum efficiency, gain as function of the supply voltage, and radioactive contamination from the screening.

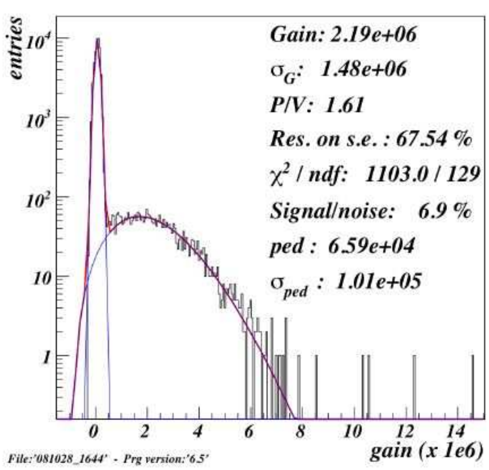

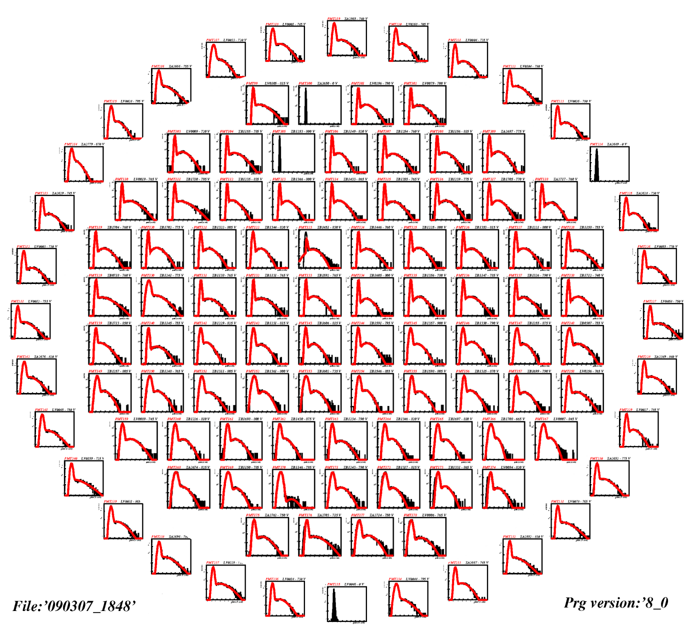

Figure 4.4: (Above) Single photoelectron response (integrated charge signal) of one of the XENON100 PMTs; (Right) Map of the bottom PMT array including the veto PMTs.

Table 4.1: **Radioactivity of XENON100 materials; average values are given if different activities were obtained for different material samples, such as different batches of PMTs and stainless steel. Upper limits are given if no activity above background was found.**

TPC Material	Unit	Quantity used	^{238}U (mBq/unit)	^{232}Th (mBq/unit)	^{40}K (mBq/unit)	^{60}Co (mBq/unit)	^{210}Pb (Bq/unit)
R8520 PMTs	PMT	242	0.15(2)	0.17(4)	9.2±1.2	1.00(8)	
PMT bases	base	242	0.16(2)	0.07(2)	< 0.16	< 0.01	
Stainless steel	kg	70	< 1.7	< 1.9	< 9.0	5.5(6)	
PTFE	kg	10	< 0.31	< 0.16	< 2.2	< 0.11	
QUPID	QUPID	-	<0.49	<0.40	<2.4	<0.21	
Shield Material							
Copper	kg	1600	< 0.07	< 0.03	<0.06	<0.0045	
Polyethylene	kg	1600	< 3.54	< 2.69	< 5.9	< 0.9	
Inner Pb (5 cm)	kg	6300	< 6.8	< 3.9	< 28	< 0.19	17(5)
Outer Pb (15 cm)	kg	27200	< 5.7	< 1.6	14(6)	< 1.1	516(90)

4.1.2 Material screening

We have built a low-background material screening facility at LNGS consisting of a HPGe detector in a four-layer shield of OFHC Cu and low-background Pb, placed inside a metal box including an air lock system, radon purge and a glove box for inserting the samples. The system is permanently monitored by slow control, the output of which is accessible online. We have screened all XENON100 materials, including the 242 PMTs. Apart from our own detector, we also used HPGe detectors from LNGS. Table 4.1 shows results from a subset of screened samples. We have identified low-background materials, such as the stainless steel used for the cryostat and the high-voltage grids, as well as the PTFE used for the TPC structure and PMT holder.

4.1.3 Background simulations

The screening results are used to model the gamma- and neutron-induced backgrounds caused by the natural radioactivity of detector materials and shields. For the current XENON100 the background is dominated by the PMTs, as shown in Table 4.2. For the upgraded detector, the background rate will be reduced by using QUPIDs and a Cu cryostat. Additionally, the self-shielding of LXe decreases the electron recoil (ER) rate in the central part of the target. The intrinsic ER rate due to β decays of ^{85}Kr will be reduced to 10^{-4} events/(kg d keV), with a Kr/Xe level of 5 ppt, achieved by using the cryogenic distillation column procured for the current experiment. (α, n) and spontaneous fission reactions in the detector, shielding materials, and surrounding rock/concrete are the dominant sources of neutrons. Based on the measured U/Th activities, we calculated the neutron yield using the Sources4A code (11) and simulated the nuclear recoil (NR) rates in the LXe target (Table 4.2). The dominant neutron flux comes from the rock/concrete walls of the laboratory. Since the predicted NR rate is higher than the one from the PMTs, we are currently adding 20 cm of water outside the Pb shield. The muon flux at the 3100 mwe Gran Sasso depth is 22 m^{-2}day^{-1}. We are simulating the expected background due to high-energy neutrons produced in the rock and in the shield. Preliminary estimates show that neutrons generated by muons in the shield, due to electromagnetic and hadronic showers and direct spallation, yield a total NR rate at the level of 2.7±0.7 single NRs/(100 kg·yr). To reduce this background, a

Table 4.2: **Predicted single scatter electron recoil (ER) and nuclear recoil (NR) background rates in the WIMP search region (2–12 keVee or 4.5–26.9 keVnr) in the central 50 kg (30 kg) target for the current XENON100 and in the central 100 kg target for the upgraded XENON100. To estimate the total background, the number of events and the sensitivity, we assume 99.5% ER rejection, 50% NR acceptance and 90% software efficiency.**

	Current XENON100				Upgraded XENON100	
Fiducial Mass	50 kg		30 kg		100 kg	
Background	ER	NR	ER	NR	ER	NR
Units [a]	$(10^{-3} dru_{ee})$	$(10^{-7} dru_{nr})$	$(10^{-3} dru_{ee})$	$(10^{-7} dru_{nr})$	$(10^{-3} dru_{ee})$	$(10^{-7} dru_{nr})$
PMTs and bases	4.91	3.25	<1.4	2.87	0.098	0.23
QUPIDs	–	–	–	–	<0.027	<0.10
Stainless steel	<2.01	<2.01	<0.35	<1.66	<0.052	<0.14
PTFE	<0.18	<6.99	<0.03	<5.04	<0.017	<1.60
Copper Cryostat	–	–	–	–	<0.033	<0.02
Polyethylene	<2.50	<5.37	<1.2	<4.73	<0.105	<0.60
^{85}Kr/U/Th [b]	<0.2	–	<0.2	–	<0.02	–
Concrete/Rocks[c]	–	1.34	–	1.11	–	0.2
μ-induced n in shield	–	33	–	33	–	0.7[d]
μ-induced n in rock	–	< 3.7	–	< 3.7	–	<3.7
Total Bkg	<9.8	<55.7	<3.2	<52.1	<0.35	<7.3
Run Time	40 days		200 days		600 days	
Raw Exposure	2000 kg-day		6000 kg-day		60000 kg-day	
Total Bkg events	<1.0		<1.2		<1.4	
# of WIMP events[e]	3.9		11.8		118	
SI $\sigma_{\chi-p}$ reach	6×10^{-45} cm^2		2×10^{-45} cm^2		2×10^{-46} cm^2 (2012)	

[a] dru_{ee} = evts/kg/keVee/day, dru_{nr} = evts/kg/keVnr/day
[b] with < 5 ppt Kr/Xe and U/Th in Xe below 10^{-13} g/g. The Upgrade requires another factor 10 reduction
[c] with a layer of 20 cm water outside the current shield
[d] with a 98% efficient muon veto
[e] for 100 GeV/c^2 WIMPs with spin-independent $\sigma_{\chi-p} = 10^{-44}$ cm^2

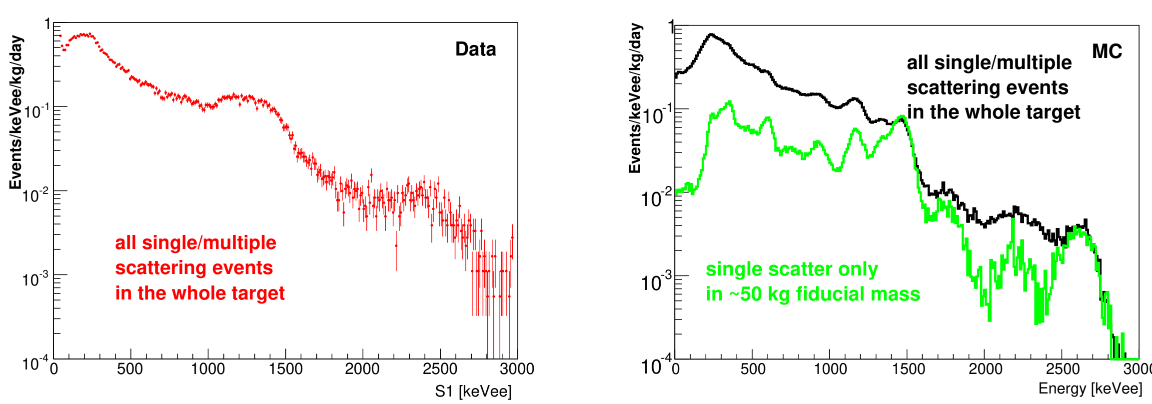

Figure 4.5: Measured (left) and MC predicted (right) background spectra in XENON100. This measurement is based on the S1 signal only, thus no position information is available.

98% efficient muon veto will be used for the upgraded XENON100. The high energy muons interacting in the rock can produce highly penetrating neutrons with energies up to few GeV, with an estimated single scatter NR rate $< 0.3/(100\,\mathrm{kg{\cdot}yr})$.

Preliminary background measurements in XENON100 have been performed with the primary scintillation (S1) signal. The measured spectrum including all event topologies (Fig. 4.5) is consistent with our Monte Carlo predictions. To obtain information on the singles rate, we need the S2 signal delivering the position information for each event.

4.2 R&D for XENON

Particles interacting in LXe produce prompt scintillation photons and ionized electrons. The *yield*, defined as the number of quanta produced per unit energy, depends on the particle species interacting in the medium. The scintillation yield of nuclear recoils relative to the scintillation yield of 122 keV gammas is known as $\mathcal{L}_{eff}$. We have recently measured $\mathcal{L}_{eff}$ at the Radiological Research Accelerator Facility (RARAF) at Columbia University. The results, shown in Fig. 4.6, tested $\mathcal{L}_{eff}$ down to 5 keV nuclear recoil energies and are not in agreement with previous data at low energies. A paper with our results and their implication for the XENON10 dark matter limits has been accepted in Phys. Rev. C (12).

The ionization yield of nuclear recoils has been measured only down to 20 keV (13). The energy threshold of XENON10 was 4.5 keV and extrapolations from higher energies were necessary. To perform new, lower energy measurements using a mono-energetic neutron beam, a dedicated dual phase xenon time projection chamber (MiniXENON) is currently being operated at the Physik Institut. A D-D neutron generator will provide the 1.5 MeV mono-energetic neutron beam. Before taking neutron data, we will test a new low-energy

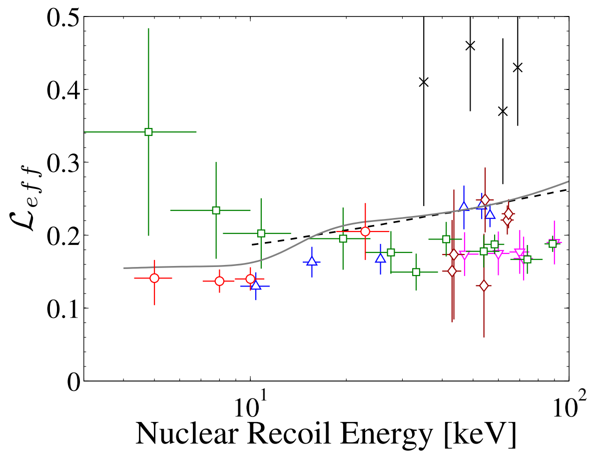

Figure 4.6: Measured $\mathcal{L}_{eff}$ values as a function of Xe nuclear recoil energy.
(○)–this work (□)–Chepel et al. [14]
(△)–Aprile et al. [15] (◊)–Akimov et al. [16]
(×)–Bernabei et al. [17] (▽)–Arneodo et al. [18]
The solid gray curve results from a recent best-fit analysis of XENON10 AmBe source data and MC [19]. Also shown is the theoretical prediction of Hitachi (dashed line) [20].

calibration source for XENON100 and the Upgrade, ^{83m}Kr. It is a decay product of ^{83}Rb, has a short half-life of 1.83 h and decays via a cascade of 32 and 9.4 keV transitions. ^{83m}Kr will be regularly introduced in the TPC, allowing S1 and S2 calibrations uniformly throughout the volume. It will also allow to determine the light and charge yield relative to low-energy gammas.

For the XENON100 Upgrade, we plan to use MiniXENON to test the new QUPID sensors. If the single photo electron response will meet our requirements, we will replace the XENON100 bottom PMT array and install an array of 19 QUPIDs. As for the current XENON100, our group will be responsible for the calibration, gain monitoring of the PMT arrays and the PMT data base.

[1] E. Aprile et al.(XENON Collaboration), New Astr. Rev. **49**, 289 (2005).

[2] B.W. Lee and S. Weinberg, Phys. Rev. Lett. **39**, 165 (1977).

[3] G. Jungman, M. Kamionkowski, and K. Griest, Phys. Rep. **267**, 195 (1996).

[4] M. W. Goodman and E. Witten, Phys. Rev. D **31**, 3059 (1985).

[5] J. Angle et al. (XENON Collaboration), Phys. Rev. Lett. **100**, 021303 (2008).

[6] Z. Ahmed et al. (CDMS Collaboration), Phys. Rev. Lett **102**, 011301 (2009).

[7] R. R. de Austri, R. Trotta, L. Roszkowski, JHEP 0707 **075** (2007).

[8] J. Angle et al. (XENON Collaboration), Phys. Rev. Lett. **101**, 091301 (2008).

[9] S. Arrenberg, L. Baudis, K. Kong, K. T. Matchev, J. Yoo, Phys. Rev. D **78**, 056002 (2008).

[10] E. Aprile and L. Baudis, Status and Sensitivity Projections for the XENON100 Dark Matter Experiment, Proceedings of Science (2009), arXiv:0902.4253.

[11] W. B. Wilson et al., SOURCES-4C: A Code for Calculating (alpha,n), Spontaneous Fission and Delayed Neutron Sources and Spectra, American Nuclei Society/Radiation Protection and Shielding Division (2002).

[12] E. Aprile, L. Baudis, B. Choi, K. L. Giboni, K. E. Lim, A. Manalaysay, M. E. Monzani, G. Plante, R. Santorelli, M. Yamashita, Phys. Rev. C **79**, 045807 (2009).

[13] E. Aprile et al., Phys. Rev. Lett. **97**, 081302 (2005).

[14] V. Chepel et al., Astropart. Phys. **26**, 58 (2006).

[15] E. Aprile et al., Phys. Rev. D **72**, 072006 (2005).

[16] D. Akimov et al., Phys. Lett. B **524**, 245 (2002).

[17] R. Bernabei et al., EPJdirect C **11**, 1 (2001).

[18] F. Arneodo et al., Nucl. Inst. and Meth. A **449**, 147 (2000).

[19] P. Sorensen et al., Nucl. Inst. and Meth. A **601**, 339 (2009).

[20] A. Hitachi, Astropart. Phys. **24**, 247 (2005).

5 Testing lepton universality, the $\pi \rightarrow e\overline{\nu}/\ \pi \rightarrow \mu\overline{\nu}$ branching ratio

P. Robmann, A. van der Schaaf, U. Straumann, P. Truöl and A. Palladino (guest from PSI/Virginia)

in collaboration with: University of Virginia, Charlottesville, USA; Institute for Nuclear Studies, Swierk, Poland; JINR, Dubna, Russia; Paul Scherrer Institut, Villigen, Switzerland and Rudjer Bošković Intitute, Zagreb, Croatia

(PEN Collaboration)

The measured value of the branching ratio

$R^{\mathrm{exp}}_{e/\mu} \equiv \Gamma_{\pi\rightarrow e\overline{\nu}(\gamma)}/\Gamma_{\pi\rightarrow\mu\overline{\nu}(\gamma)} = 1.230(4) \times 10^{-4}$ (1)

exhibits the best test of the universality of the coupling $Wl_i\nu_{l_i}$ (i=1,2,3 generation number) of the W boson to the leptons.

Within the Standard Model the decay $\pi \rightarrow e\overline{\nu}$ is helicity suppressed ($R_{e/\mu} \approx m_e^2/m_\mu^2/(1 - m_\mu^2/m_\pi^2)^2 \approx 1.3\times10^{-4}$) which makes it sensitive to a number of hypothetical exotic contributions (2).

The PEN experiment aims at reducing the uncertainty for $R^{\mathrm{exp}}_{e/\mu}$ by an order of magnitude (3) which would bring it in the region of the present theoretical accuracy. See the Annual Report 2006/07 for further details on the theoretical motivation and a description of the PEN detection system.

5.1 Measurement principle

Determinations of $R_{e/\mu}$ are based on observing final states with positrons emerging from a stopped π^+ beam. Decays $\pi \rightarrow e\overline{\nu}(\gamma)$ result in positrons appearing with the pion lifetime (26 ns) and with an energy distribution peaking at $E_{e^+} = m_\pi c^2/2$. Decays $\pi \rightarrow \mu\overline{\nu}(\gamma)$ result in positrons too, through the subsequent decay $\mu \rightarrow e\nu\overline{\nu}$. The latter process leads to a time distribution first rising with the pion lifetime and then falling with the muon lifetime of 2.2 μs, and to a continuous energy distribution with $E_{e^+} \leq m_\mu c^2/2$. Whereas $\approx$ 98% of the $\pi \rightarrow e\overline{\nu}(\gamma)$ decays are unambiguously identified by their energy, in the remaining $\approx$ 2% the observed energy leaks into the region below $m_\mu c^2/2$ dominated by $\pi \rightarrow \mu\overline{\nu}(\gamma)$. For this reason it is crucial to know (measure and/or simulate) the full $\pi \rightarrow e\overline{\nu}(\gamma)$ energy distribution.

Random background from accidental pion-positron coincidences is suppressed by rejecting event topologies with nearby additional pion signals and the remaining background is extrapolated from events in which positrons are observed before a pion stop.

All measurements so far removed events in which the positrons appeared within a few ns after the pion stop time to suppress background processes originating in the abundant pion reactions with target nuclei. For our experiment such approach would require the knowledge of the time offset with a precision of $\approx$ 20 ps which would introduce a major source of systematic error. For this reason we decided to include the prompt region and control the prompt background by reducing the beam momentum and improving the event signature by a careful measurement of the pion energy deposition and range. For this purpose the pion energy loss is measured all along the trajectory with the help of active beam elements (plastic scintillator) read out with 2 GHz digitizers. The scheme not only helps to account for pion reactions but also for decays during the moderation process.

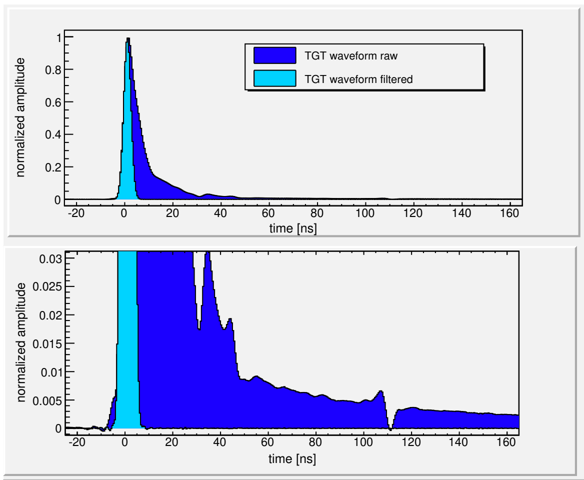

Figure 5.1: Raw and shaped target signals averaged over a very large number of pion interactions in the active target. The upper panel shows the full signal. In the lower panel the scale is reduced to show the structure in the signal tail. The shaping algorithm is explained in the text.

5.2 Target waveform analysis

Figure 5.1 shows the mean target waveform for pion reactions from a large sample of events before and after numerical shaping. The latter primarily removes distortions introduced by imperfect signal propagation (attenuation, dispersion, reflections) through the photomultiplier, cabling, splitters and mismatched terminators. The $\approx 0.5\%$ structure after 110 ns, for example, is caused by an AC-coupled timing discriminator. One also notices a $\approx 0.5\%$ shoulder in the leading edge which may result from crosstalk between the final dynodes of the photomultiplier.

The shaping is done in a single pass:

$$\tilde{w}_i = \sum_{k=k_{\min}}^{k_{\max}} s_k w_j ,\ k \equiv i - j \ , \qquad (5.1)$$

where w and $\tilde{w}$ are the raw and shaped waveforms, respectively, and s_k is an array

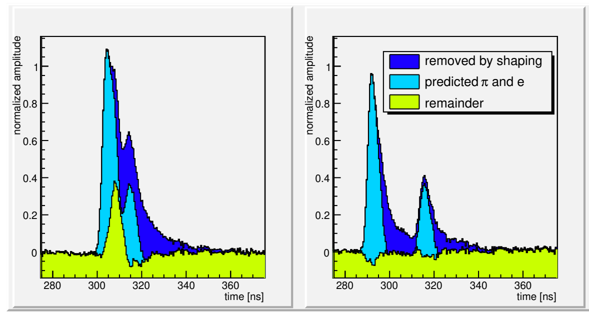

Figure 5.2:
Typical target waveforms for $\pi \to \mu \to e$ (left) and $\pi \to e\nu$ (right). Signals predicted for pion and positron are subtracted, as discussed in the text. For the $\pi \to e\nu$ event, the remaining signal is nil, while for the $\pi \to \mu \to e$ event, a 4 MeV muon is observed.

of coefficients trained to make $\tilde{w}$ approach a Gaussian distribution with $\sigma = 1.5$ ns as closely as possible (4). The shaping interval $(k_{\min}, k_{\max})$ roughly coincides with the region shown in Fig. 5.1. One should keep in mind that the scintillation signal has an intrinsic fall time of ≈ 2 ns only so there is no significant loss in statistical accuracy of the associated energy signal. We believe the method described is novel [4] certainly in the fields of particle and nuclear physics.

Figure 5.2 shows examples of target waveforms for the two decay modes. The waveform discrimination is done by comparing χ^2 values of waveform fits with and without an intermediate muon. Since pulses may appear almost simultaneously additional constraints on the amplitudes of the particles involved are included in the χ^2 expressions for the two hypotheses:

- E_μ
  The energy of the mono-energetic muon is fixed to 4.1 MeV from 2-body kinematics.

- t_π and t_e
  Pion and positron times are fixed to the values deduced from the degrader and the

[4] Similar problems occur in totally different areas such as acoustics and seismology but so far we didn't find treatments as rigorous as ours

plastic hodoscope, respectively.

- $\boldsymbol{E_\pi}$
  Pion energy in the target can be predicted from the kinetic energy deduced event-by-event from the pion time of flight over the final 3.5 m of the beamline after correction for the observed energy loss in the degrader. Figure 5.3 shows the correlation between predicted and observed pion energies in the target, which is small on the scale of the 4.1 MeV muon.

- $\boldsymbol{E_e}$
  The positron energy scales with the positron path length in the target, which can be deduced from the observed positron and pion trajectories (see below). As in the case of the pion the deviation from the predicted value, normalized to the uncertainty, is included. In the $\pi \to \mu \to e$ fit the uncertainty is affected by the 1.5 mm distance traveled by the muon.

The above considerations lead to the following extended χ^2 expression:

$$\chi^2 = \frac{1}{n_{\mathrm{d.o.f.}}} \sum_{i=1}^{n} \left(\frac{\tilde{w}_i^{\mathrm{fit}} - \tilde{w}_i}{\sigma_{\tilde{w}}} \right)^2 + \left(\frac{E_\pi^{\mathrm{fit}} - E_\pi^{\mathrm{pred}}}{\sigma_{E_\pi}} \right)^2 + \left(\frac{E_e^{\mathrm{fit}} - E_e^{\mathrm{pred}}}{\sigma_{E_e}} \right)^2 ,$$

where $\tilde{w}$ was introduced in Eq. 5.1. The summation is limited to the n bins of $\tilde{w}_i$ which receive contributions from the $\pi \to \mu \to e$ fit so n varies depending on the amount of overlap between the three peaks. The number of degrees of freedom $n_{\mathrm{d.o.f.}}$ equals n-2 and n-3 for the fits to $\pi \to e\nu$ and $\pi \to \mu \to e$, respectively. σ_{E_π}=0.6 MeV and σ_{E_e} is distributed according to the asymmetric energy-loss distribution.

Figure 5.4 shows preliminary results for the χ^2 difference between the two decay hypotheses indicating a separation of better than 1:100 based on waveform analysis alone.

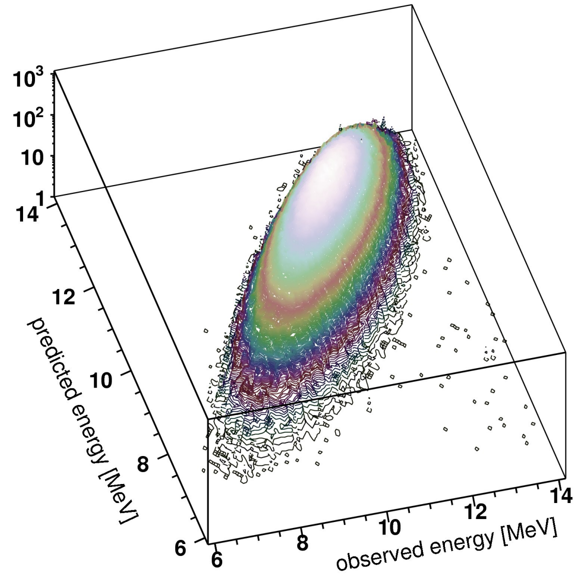

Figure 5.3:
Distribution of observed versus predicted pion energy in the target. The predicted energy is the kinetic energy deduced from the measured pion velocity corrected for the observed energy loss in the degrader.

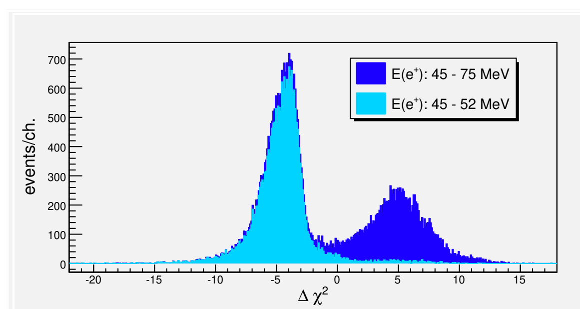

Figure 5.4:
Distributions of the difference in χ^2 with/without intermediate muon. Events were selected in which the positron appeared within 75 ns after the pion stop. Note the contribution in the lower-energy interval with $\Delta\chi^2 \approx 5$ which is expected from the low-energy tail of the $\pi \to e\nu$ response.

Figure 5.5: The four-plane wedged degrader used in 2008 to measure the pion trajectory before wrapping. The beam enters from the left.

5.3 A poor man's beam tracker

The determination of the decay vertex requires the tracking of both the positron and the pion. In future running, the pion tracking will be done with a mini-TPC which is presently being tested. Halfway during the 2008 data-taking we installed as an intermediate solution a fourfold segmented degrader (see Fig. 5.5) which was produced in our mechanical workshop.

Depending on the pion position in the transverse plane, the energy loss in the four detector elements varies which allows position determination. Unfortunately, the 12 mm thick detector significantly affects the pion trajectories by multiple scattering resulting in a relatively poor ($\sigma \approx 2$ mm) vertex resolution. It also appears that the light collection shows significant position dependence which had to be taken into account numerically.

5.4 Outlook

A second four-month period of data-taking has been scheduled for the end of 2009. As mentioned above, we will use a new mini-TPC for pion tracking. This detector will be situated between the degrader and the target. This modification in the setup will not only lead to a dramatic improvement in vertex resolution, but also allow for a 10% reduction in beam momentum which will result in improved time-of-flight resolution and thus a lower σ_{E_π}.

Meanwhile we will proceed with the analysis of the 2008 data. Presently we are developing the framework of a sophisticated likelihood analysis of all observables discussed above. In addition to the two main signal processes, a series of other event types have to be included to push the systematic error in the branching ratio well below 10^{-3}. Radiative decays, in-flight decays, various types of accidental coincidences and pion reactions have been identified so far. It is our aim to determine all probability density functions directly from the measurement. To help access systematic uncertainties, detailed Monte Carlo studies have recently been initiated.

[1] G. Czapek et al., Phys. Rev. Lett. **70** (1993) 17; D. I. Britton et al., Phys. Rev. Lett. **68** (1992) 3000.

[2] M. Raidal and A. van der Schaaf et al., Eur. Phys. J. C **57** (2008) 13 [arXiv:0801.1826 [hep-ph]].

[3] PEN Collaboration, PSI experiment R-05-01, D. Pocanic and A. van der Schaaf, spokespersons.

[4] A. Palladino, D. Pocanic and A. van der Schaaf, in preparation.

6 Evidence for $K\pi$-atoms

Y. Allkofer, C. Amsler, A. Benelli[5], S. Horikawa, C. Regenfus, and J. Rochet

in collaboration with:
CERN, Czech Technical University, Institute of Physics ACSR and Nuclear Physics Institute ASCR (Czech Republic), Laboratori Nazionali di Frascati, Messina University, Trieste University, KEK, Kyoto Sangyo University, Tokyo Metropolitan University, IFIN-HH (Bucharest), JINR (Dubna), Skobeltsin Institute for Nuclear Physics (Moscow), IHEP (Protvino), Santiago de Compostela University, Basel University, Bern University.

(DIRAC-II Collaboration)

Electromagnetically bound $\pi^{\mp}K^{\pm}$-pairs ($\pi^{\mp}K^{\pm}$-atoms) have been observed for the first time in 2008 by our DIRAC-II Collaboration at CERN (1; 2). The $\pi^{+}K^{-}$-atom is unstable and decays through the strong force into $\pi^0\bar{K}^0$ (while π^-K^+-atoms decay into π^0K^0). The mean life τ, which we intend to measure, is related to the S-wave πK-scattering lengths a_1 and a_3 in the isospin 1/2 and 3/2 states, respectively. The πK-scattering length is of interest to test chiral perturbation theories extended to the s-quark.

Predictions for τ can be obtained from the S-wave phase shifts of the πK-system, extrapolated to low energy kaon-nucleon scattering ($\pi K \to \pi K$ scattering off the exchanged π). However, kaon-nucleon scattering at low momentum is difficult due to the short lifetime of the kaon and hence the S-phase shifts are poorly known at low energy. The experimental uncertainties in a_1 and a_3 are correspondingly substantial, and the predicted mean life of πK-atoms scatters between 1 and 5 fs. Using the values from dispersion relations (3) one predicts a mean life $\tau \sim$ 3.7 fs.

Details on the previous apparatus (DIRAC-I) to study $\pi^+\pi^-$-atoms (4) can be found in ref. (5). A sketch of the modified spectrometer (DIRAC-II) to collect the πK (and more $\pi\pi$) data is shown in Fig. 6.1. The 24 GeV/c proton beam from the CERN-PS impinges on a

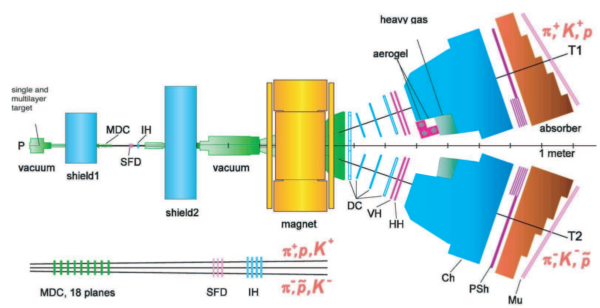

Figure 6.1: Sketch of the updated DIRAC-II spectrometer, showing the locations of the Čerenkov counters to identify electrons, pions and kaons. MDC = microdrift chambers, SFD = scintillator fibre detector, IH = ionization hodoscope, DC = drift chambers, VH, HH = vertical and horizontal scintillation hodoscopes, PSh = preshower, Mu = muon counters.

26 μm Pt-target (average intensity of 1.6×10^{11} protons/pulse). The proton beam then passes through a vacuum pipe and is absorbed by the beam dump. The secondary particles emerging from the target are analyzed in a double-arm magnetic spectrometer measuring the momentum vectors of two oppositely charged hadrons. The particles are collimated through two steel shielding blocks, upstream of the microdrift chambers (MDC) and downstream of the ionization hodoscope (IH), respectively. They pass through a vacuum chamber and are bent by the 1.65 T field of the dipole magnet. The two-arm spectrome-

[5] Visitor from the University of Basel

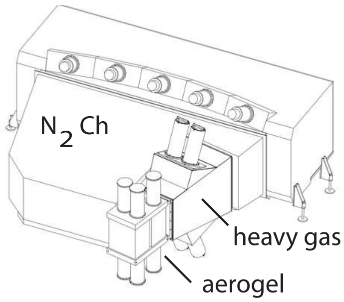

Figure 6.2:
N_2, aerogel and heavy gas Čerenkov counters.

ter is tilted upwards with respect to the proton beam by an angle of 5.7°. Positive particles are deflected into the left arm, negative ones into the right arm. Electrons and positrons are vetoed by the N_2-Čerenkov detectors (Fig. Fig. 6.2) and muons by their signals in scintillation counters behind the steel absorbers. Pions are separated from kaons with the heavy gas and aerogel counters. The signal from πK-atoms is observed for kaon and pion pairs with a very small relative momentum (typically $|Q_L| < 3$ MeV/c is the c.m.s system).

The Zurich group carries the main responsibility for the πK measurements, while the rest of the collaboration concentrates on $\pi\pi$. Our group has developed and built a novel aerogel Čerenkov counter in the left arm (positive charges) for kaon detection and proton suppression, and the heavy gas system for pion detection. An aerogel detector in the right arm (negative charges) is not necessary since the antiproton flux is negligible compared to that from negative kaons, while protons in the left arm are much more frequent than positive kaons. The aerogel detector consists of three independent modules. Two of them (total volume of 24ℓ) have refractive index $n = 1.015$ for kaons between 4 and 5.5 GeV/c, and the third one (13ℓ) has the lower index $n = 1.008$ for 5.5 to 8 GeV/c kaons and kaon-proton separation. The loss due to light absorption is compensated by using a wavelength shifter and by increasing the radiator thickness in the center of the detector (pyramid geometry). Details can be found in our recent publications (6; 7) and in previous annual reports.

The startup of DIRAC-II, originally planned for summer 2006, was postponed by one year due to repeated failures of a switching magnet in the CERN primary proton beam line. The defective magnet was successfully replaced in spring 2007 and DIRAC-II could be commissioned in June 2007. The aerogel counters worked according to expectations and data were taken in 2007 and 2008.

Last year the Zurich group was involved in the data analysis of the runs taken so far. This includes test beam calibrations and Monte-Carlo simulation for the aerogel counter. An event preselection was performed for both the πK and the $\pi\pi$ data. We studied the energy loss in the detector for the various particles and thereby cured a longstanding small momentum shift in the Q_L-distribution. We now describe the analysis of the 2007 data which led to the first observation of πK-atoms (1; 2).

For this analysis we used only detectors downstream of the dipole magnet. The trajectories were determined by the drift chambers, the pattern recognition starting from the coordinates in the last plane and extrapolating back to the target. The variable of interest in the following analysis is the relative momentum Q of the $\pi^{\mp}K^{\pm}$-pairs in their center-of-mass systems, in particular the longitudinal component Q_L which is not affected by multiple scattering. In the transverse plane, the resolution on the relative momentum Q_T (typically 3 MeV/c) is dominated by multiple scattering, while the resolution on the longitudinal component Q_L ($<$ 1 MeV/c) is not affected. For further analysis we use therefore only Q_L.

Figure 6.3 shows the four mechanisms which contribute to the production of $\pi^{\pm}K^{\mp}$-pairs. Accidental pairs are due to particles produced on different nucleons (Fig. 6.3a), non-Coulomb-pairs are associated with the production of long-lived intermediate states

(Fig. 6.3b). On the other hand, $\pi^{\pm}K^{\mp}$-pairs which interact electromagnetically form correlated Coulomb-pairs (Fig. 6.3c), or atomic bound states (Fig. 6.3d). The latter atoms, while traveling through the target, can either decay, be (de)-excited or break up into $\pi^{\pm}K^{\mp}$-pairs which emerge from the target with very low relative momentum.

For prompt pairs the time difference between the positive and negative spectrometer arm lies between –0.5 and 0.5 ns. Accidental pairs are first removed using the time information from the vertical hodoscopes. Accidental pairs (those with large time differences) are also needed for subsequent analysis. Electrons or muons are removed, and a loose preselection of oppositely charged particles is performed (2). Pions, kaons and protons below 2.5 GeV/c can be separated by time-of-flight. For the $\pi^{-}K^{+}$ analysis the aerogel detector is used in addition to remove protons in the positive arm, while for the $\pi^{+}K^{-}$ analysis the time difference between the negative and the positive arm has to be negative to remove protons faking pions.

Once the accidentals have been subtracted the prompt pairs are composed of the following three types: atomic-pairs, Coulomb-pairs, and non-Coulomb-pairs. We assume that the background due to non-Coulomb pairs can be described by the Q_L-distribution of accidentals, following a similar analysis for $\pi^{+}\pi^{-}$-atoms (4). Coulomb pairs have to be simulated. Since the shapes of both contributions are known, one can extrapolate into the $|Q_L| < 3$ MeV/c signal region. The difference (residuals) between the data and the sum of both contributions is plotted in Fig. 6.4. Above $|Q_L| = 3$ MeV/c the residuals are consistent with zero, while the enhancement at low relative momentum is the first evidence for πK-atoms. We obtain 173 $\pm$ 54 detected atomic pairs with a statistical significance of 3.2σ. The systematic uncertainty is estimated to be around 5%, much smaller than the statistical one.

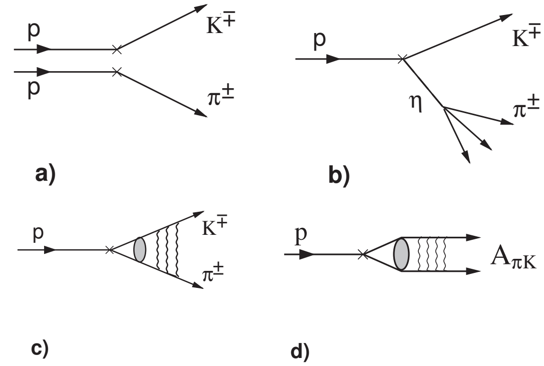

Figure 6.3:
Production mechanisms of πK-pairs: a) accidental-pairs from two protons; b) non-Coulomb-pairs from long-lived intermediate states such as the η-meson; c) Coulomb-pairs from direct production or from short-lived intermediate states; d) πK-atoms.

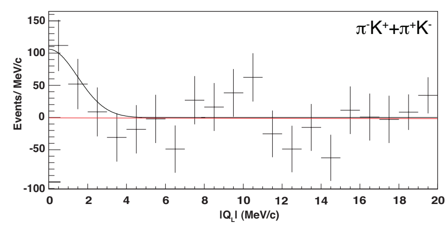

Figure 6.4:
Residuals between data and the fitted background for $\pi^{-}K^{+}$ and $\pi^{+}K^{-}$. A Gaussian fit has been applied (solid line) to illustrate the distribution of atomic-pairs.

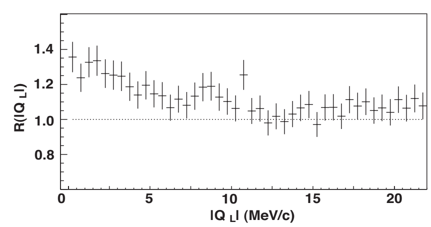

Figure 6.5:
Correlation function R as a function of $|Q_L|$ for πK-pairs. The deviation from the horizontal dotted line proves the existence of Coulomb-πK-pairs.

The evidence for the observation of πK-atoms is strengthened by the observation of Coulomb-pairs which, a fortiori, implies that atoms have also been produced. This can be seen as follows: non-Coulomb pairs have a similar Q_L-distribution as accidentals. Hence dividing the normalized distribution for prompt pairs by the one for accidentals one obtains the correlation function R describing Coulomb-pairs. The function R, shown in Fig. 6.5 as a function of $|Q_L|$, is clearly increasing with decreasing momentum, proving that Coulomb-pairs have been observed.

The ratio of the number of produced atoms to the number of Coulomb-pairs with small relative momenta has been calculated (8; 9). This number needs to be corrected by Monte-Carlo simulation to take into account the acceptance of the apparatus and the cuts applied in the analysis. The breakup probability P_{br} relates the number of atoms to the number of atomic pairs. A calculation of the breakup probability as a function of mean life (Fig. 6.6) has been performed using the Born approximation (10). For the predicted mean life of 3.7 fs P_{br} is 53% (dotted line in Fig. 6.6). One then obtains from the number of produced atoms the predicted number of observed atomic pairs, 147 $\pm$ 36, in good agreement with the experimental result.

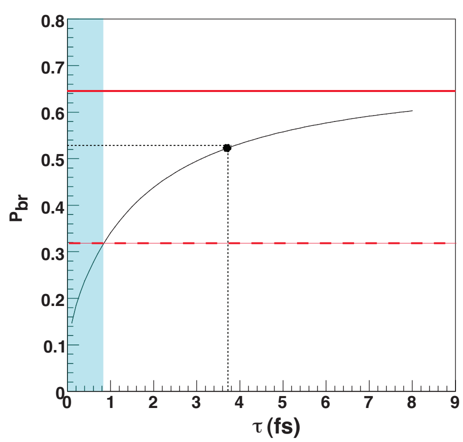

Figure 6.6: Breakup probability P_{br} for the 26 μm Pt-target as a function of mean life of πK-atoms in the 1s-state. The horizontal solid line is the measured breakup probability and the horizontal dashed line the 1.28σ lower bound corresponding to a lower limit of 0.8 fs for the mean life. The excluded area (90% confidence level) is shown in blue. The horizontal dotted line gives the theoretical prediction corresponding to 3.7 fs.

Conversely, one can use the number of observed atomic-pairs from the fit and the number of Coulomb-pairs below $|Q_L| < 3$ MeV/c to calculate the breakup probability: P_{br} = 64 $\pm$ 25 % (horizontal solid line in Fig. 6.6). This leads to a lower limit for the mean life of πK-atoms of τ_{1S} = 0.8 fs at a confidence level of 90%. This result can be translated into an upper limit $|a_{1/2} - a_{3/2}| < 0.58\ m_\pi^{-1}$ at 90% confidence level.

The choice of Pt as production target for the 2007 data was justified by the high breakup probability so that of πK-atoms could be observed. Data taken in 2008 – 2010 are being collected with a 98 μm Ni-target, for which the breakup probability is lower ($\sim$35% according to ref. (10)) but still rapidly rising around the predicted mean life of 3.7 fs. This will allow a more accurate measurement of τ. The ultimate goal is to measure the mean life of πK-atoms with a precision of about 20%, leading to a 10% uncertainty in the difference of scattering lengths $|a_{1/2} - a_{3/2}|$.

[1] B. Adeva et al. (DIRAC Collaboration), Phys. Lett. **B 674** (2009) 11.

[2] Y. Allkofer, PhD Thesis, University of Zurich (2008).

[3] P. Büttiker, S. Descotes-Genon, B. Moussallam, Eur. Phys. J. **C 33** (2004) 409.

[4] B. Adeva et al. (DIRAC Collaboration), Phys. Lett. **B 619** (2005) 50.

[5] B. Adeva et al. (DIRAC Collaboration), Nucl. Instr. Meth. in Phys. Res. **A 515** (2003) 467.

[6] Y. Allkofer et al., Nucl. Instr. Meth. in Phys. Res. **A 582** (2007) 497; Y. Allkofer et al., Nucl. Instr. Meth. in Phys. Res. **A 595** (2008) 84.

[7] S. Horikawa et al., Nucl. Instr. Meth. in Phys. Res. **A 595** (2008) 212.

[8] L.L. Nemenov, Sov. J. Nucl. Phys. **41** (1985) 629.

[9] L. Afanasyev and O. Voskresenskaya, Phys. Lett. **B 453** (1999) 302.

[10] B. Adeva et al., CERN-SPSC-2004-009, SPSC-P-284, Add.4.

7 Particle Physics at DESY/HERA (H1)

K. Müller, K. Nowak, P. Robmann, A. Schöning, U. Straumann, and P. Truöl

in collaboration with:
C. Grab and M. Sauter, Institut für Teilchenphysik der ETH, Zürich, S. Egli, M. Hildebrandt, and R. Horisberger, Paul Scherrer Institut, Villigen, and 37 institutes outside Switzerland

(H1 - Collaboration)

Since the end of the running period of HERA in 2007 the collaboration concentrates on the analysis of the high quality HERA-II data sets collected in the years 2004-2007 after the upgrade of the H1 detector with an integrated luminosity of 238 pb^{-1} for collisions with electrons and 219 pb^{-1} for collisions with positrons. The final months of HERA operation were devoted to collisions at lower proton energies: 6.2 pb^{-1} and 12.4 pb^{-1} were collected with 27.4 GeV positrons colliding with 575 or 460 GeV protons, respectively. This data has been used for a first direct measurement of the longitudinal structure function F_L(1).

In fifteen years of data taking, the results of the H1 and ZEUS experiments already found their way into the textbooks. Besides the deep insight into the structure of the proton at very small distances which has a major impact on the LHC experiments, the HERA measurements confirmed the nature of the strong force and showed that indeed the weak and the electromagnetic force have the same strength at high momentum transfer and can be unified into the electroweak force. The full data set of HERA allows to present most of the final results with low statistical and systematical errors.

Nine publications (1) – (9) and many contributions to the XVI International Conference on High energy Physics in Philadelphia 2009 (10) – (33) document the continuing effort in the analysis of the H1 data. New results, partly preliminary (34), which deserve to be mentioned, concern the following topics:

- Direct measurement of the longitudinal structure function F_L at medium Q^2 (1).
- Precise determination of the neutral electroweak current cross sections over a large range of the squared four momentum transfer Q^2 and the extraction of the parton density functions (PDF) (11; 12).
- Multi-jets at high and low Q^2 leading to an improved determination of the running coupling constant α_s (13).
- Photo-produced diffractive dijets (14), diffractive ρ- and ϕ-mesons (16), inelastic J/ψ (15), beauty (25) and D^*-mesons (21), and prompt photons (20).
- Search for states and interactions outside the Standard Model (SM), such as leptoquarks (17), single top production, excited electrons and quarks (9; 18), multi-lepton production (8) and isolated leptons with large missing momentum (4).
- Strangeness (5; 23) and D^*-meson (28) production in deep inelastic scattering, charm fragmentation (6) and the extraction of the charm and beauty contribution to the proton structure function (29; 30).

In the past years our analysis effort concentrated on events with isolated photons produced in either photoproduction ($Q^2 \approx 0$), as discussed below (Sec. 7.3), or deep inelastic scattering ($Q^2 > 4$ GeV^2). The latter is already published (35; 36) and has been described in previous annual reports (37).

7.1 Single top production

Top quarks are of particular interest in searches for new physics because of the large top mass which is close to the electroweak scale. In ep collisions top production in the standard model is strongly suppressed, hence the observation of single top production would be a clear indication of a new physics process. Several extensions of the SM predict the top quark to undergo flavour changing neutral current interactions (FCNC) which could lead to a sizeable cross section at HERA ($ep \to \nu tbX$).

A search for single top production was performed using the full $e^{\pm}p$ data set with a total integrated luminosity of 474 pb^{-1}. Single top production is detected via the decay of the top quark $t \to bW$.In the case of leptonic decays of the W the signature is a charged lepton and missing transverse momentum, accompanied by a high transverse momentum (P_T) hadronic final state from the fragmentation of the b quark. The signature for single top production with a subsequent hadronic decay of the W is three high P_T jets with an invariant mass compatible with the top mass. To estimate a possible top quark contribution in a sample with isolated leptons or high P_T jets, a top quark candidate is reconstructed from its decay products (lepton or two jets, neutrinos and b quark). Three observables are defined to discriminate the top signal from QCD background corresponding to the transverse momentum of the reconstructed b quark, the invariant mass of the reconstructed top and the W decay angle.

A multivariate discriminant based on a neural network is formed to differentiate top quark candidates from SM background. Fig. 7.1 shows the discriminator D for the electron and the muon channel. The SM background, mainly from W production is located at small values of D whereas the expectation for a single top signal is at large values of D. Also shown are the data events as classified by the discriminator. The observed slight excess of events with an isolated lepton and high missing transverse momentum has already been reported in previous years(4; 38; 39). The signal cross section is extracted from the discriminator spectra using the fractional event counting which takes statistical and systematical uncertainties into account. For all channels combined an upper bound of the cross section for anomalous single top production via FCNC is:

$$\sigma(ep \to etX) < 0.25 \text{ pb} .$$

The limits on the cross section are converted to limits at 95% CL on the anomalous FCNC coupling $\kappa_{tu\gamma}$. They are shown in Fig. 7.2 with

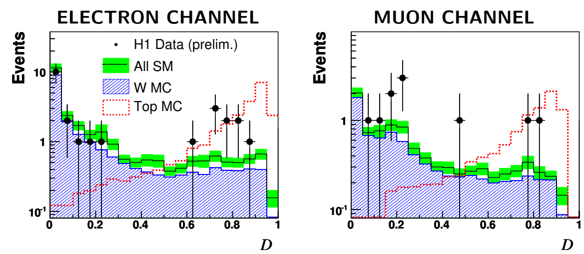

Figure 7.1: Distribution of the discriminant which is used to differentiate single top production from SM background processes for the channel with an isolated electron (left) and an isolated muon (right).

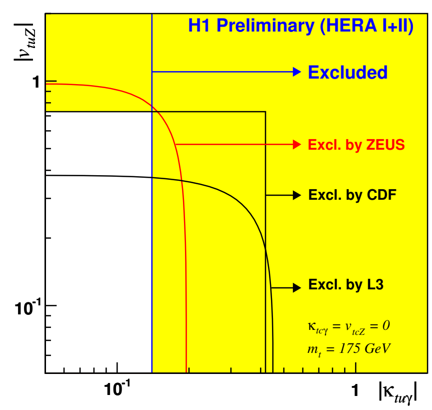

Figure 7.2: Exclusion limit at 95% CL on the anomalous $\kappa_{tc\gamma}$ and v_{tuZ} couplings. The domain excluded by H1 is represented by the light shaded area.

the limits of other experiments. The limit of the ZEUS (40) experiment which is based on HERA1 data only are only slightly weaker, mainly reflecting the top like events observed by H1 and not by ZEUS. The measurement has been presented to several conferences and is in the process of being published.

7.2 Measurement of $F_2^{c\bar{c}}$ and $F_2^{b\bar{b}}$

The measurement of inclusive charm (c) and beauty (b) quark cross sections in deep inelastic scattering at HERA provides an important test of QCD. The charm structure function $F_2^{c\bar{c}}$ and the beauty structure function $F_2^{b\bar{b}}$ are obtained from a measurement of the cross section of events containing heavy quarks. They are distinguished from events containing light quarks using variables reconstructed in the H1 Silicon Vertex Detector. The most important of these variables is the significance, defined as the transverse displacement of tracks from the primary vertex divided by the error. For events with three or more tracks in the vertex detector the reconstructed variables are used as input to a neural net. The fractions of c, b and light quarks are extracted in each bin by a least square simultaneous fit to the NN output and the significance of the two tracks with the highest significance.

The fraction of the beauty cross section to the total cross section varies from 0.2% at $Q^2 = 5$ GeV^2 to 1.0% at $Q^2 = 60$ GeV^2. The fraction of the charm cross section is 16% in average and increases slightly with increasing Q^2 and decreasing x. The measurement of $F_2^{c\bar{c}}$ as a function of Q^2 is shown in Fig. 7.3. The data are compared to a NLO (41) and a NNLO(42) calculation, which gives a better description at low Bjorken x, the momentum fraction carried by the struck quark. The measurement has been presented on various conferences (29) and will soon be published.

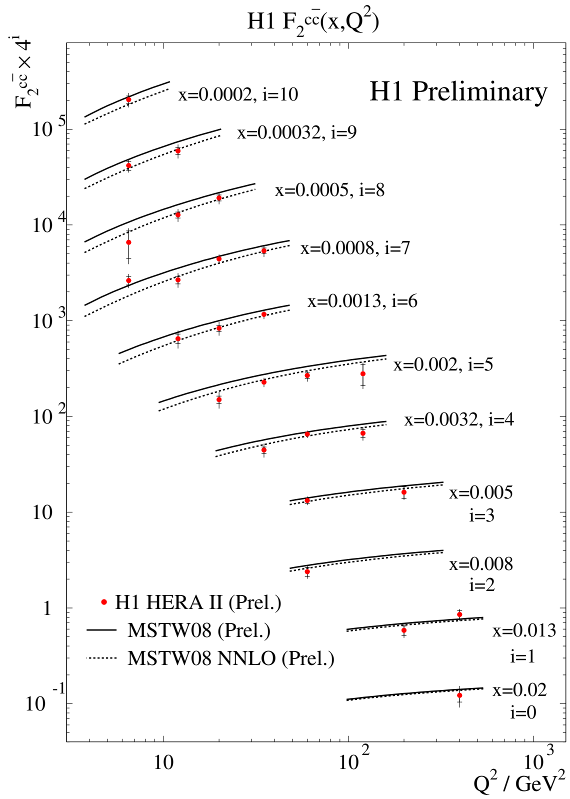

Figure 7.3: The charm structure function $F_2^{c\bar{c}}$ as a function of Q^2 for various x values. The inner error bars show the statistical error, the outer error bars represent the statistical and systematic errors in quadrature. QCD predictions at NLO are shown as dotted line and at NNLO as full line.

7.3 Isolated photons in photoproduction

Events with an isolated photon emerging from the hard subprocess $ep \rightarrow e\gamma X$ - so called prompt photons - are a powerful probe of the dynamics of the hard subprocess. They require generally lower corrections for hadronisation than measurements relying on jets, since the photons emerge without the hadronisation process by which final state quarks or gluons form a jet. Production of isolated photons with high transverse momentum can be calculated in QCD, but previous measurements have shown that higher order corrections are important. In photoproduction (PhD thesis of Krzysztof Nowak) at very low Q^2 the scattered electron escapes detection through the beam pipe. The exchanged quasi-real photon either interacts directly with a parton from the proton (direct contribution) or resolves into partons which take part in the interaction (resolved contribution). Hence, the cross section yields information on the quark and gluon densities in the photon and the proton with different and generally lower corrections for hadronisation than in jet measurements. The data collected during 2004-2007 correspond to a total integrated luminosity of 340 pb^{-1}, three times the value of the previous measurement.

Isolated photons with transverse energy $6 < E_T^\gamma < 15$ GeV and pseudorapidity $-1.0 < \eta^\gamma < 2.4$ are selected in events with inelasticity $0.1 < y < 0.7$. This considerably extends the phase space of previous measurements at HERA towards larger pseudorapidities of the photon and to lower event inelasticities. To ensure isolation of the photon, the energy fraction z of the photon-jet carried by the photon candidate has to to be larger than 90% ($z \equiv E^\gamma/E^{photon-jet} > 0.9$). The isolation rejects a large part from the background from decay photons of neutral hadrons in dijet photoproduction events. The photon signal is extracted by combining different shower shape variables into a discriminator and then unfolding the photon signal. A regularised unfolding procedure (43) is used to relate the measured observables to the true variables on hadron level, determine the fraction of signal and background and to correct the data for the detector acceptance. The observables are the transverse energy E_T^γ and pseudorapidity η^γ of the photon. Each E_T^γ-η^γ bin is further divided into bins in variables depending on jet properties for the exclusive measurements. In addition, each measurement bin is binned in the discriminator D to allow the discrimination of signal and background. The unfolding matrix is computed using the PYTHIA(44) simulations for the signal and the background.

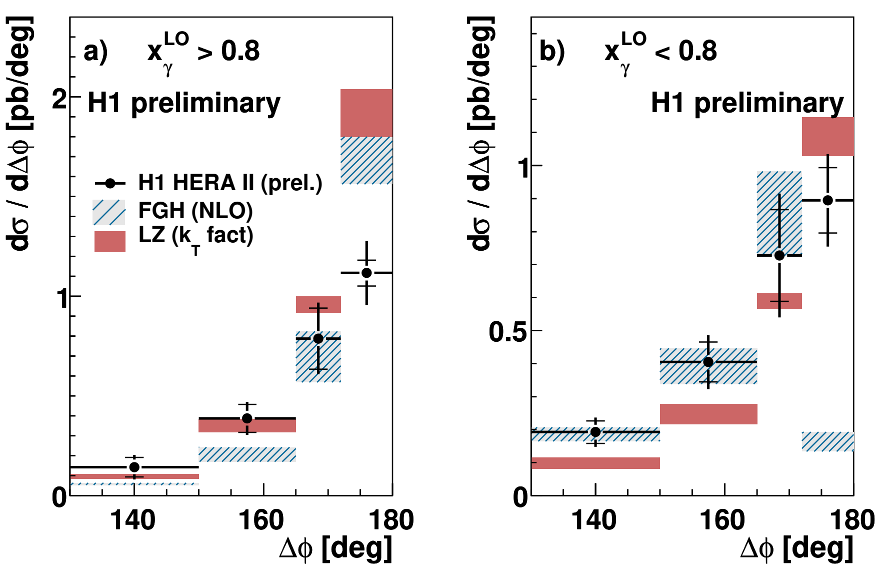

Figure 7.4: Differential prompt photon plus jet cross sections $d\sigma/d\Delta\Phi$ for a sample with the direct (a) and the resolved (b) contribution enhanced. The cross section is measured for photons with transverse energy $6 < E_T^\gamma < 15$ GeV and pseudorapidity $-1.0 < \eta^\gamma < 2.43$ accompanied by a hadronic jet with $E_T^{jet} > 4.5$ GeV and $-1.3 < \eta^{jet} < 2.3$. The inelasticity is restricted to $0.1 < y < 0.7$.

Transverse correlations between the photon and the jet are studied for prompt photons accompanied by a hadronic jet. They are particularly sensitive to higher order gluon emission. Fig. 7.4 shows the azimuthal acoplanarity between the photon and the jetfor (a) $x_\gamma^{LO} > 0.8$ where the direct interaction of a photon with the proton dominates and for (b) $x_\gamma^{LO} < 0.8$ with a significant contribution of events with a resolved photon. The data are compared to a NLO calculation (45), denoted by FGH, and a calculation based on the k_T factorisation approach which uses the un-integrated quark and gluon densities of the proton and the photon according to the Kimber-Martin-Ryskin prescription (46) (LZ).

Both predictions slightly overestimate the back-to-back configuration for $x_\gamma^{LO} > 0.8$. For $x_\gamma^{LO} < 0.8$ there is a lower contribution from the back-to-back configuration and the photon tends to be closer to the jet. This reflects the increased contributions from events with a resolved photon and from photons radiated from quarks. FGH describes the distributions within the errors, except for the highest bin in $\Delta\Phi$ for $x_\gamma^{LO} < 0.8$. This region is sensitive to multiple soft gluon radiation which limits the validity of fixed order calculations. The LZ predicts a significantly lower contribution of events with no back-to-back signature.

[1] F. D. Aaron *et al.* [H1 Collaboration], Phys. Lett. B **665** (2008) 139, arXiv:0805.2809 [hep-ex].

[2] **A General Search for New Phenomena at HERA**, F. D. Aaron *et al.* [H1 Collaboration], arXiv:0901.0507 [hep-ex].

[3] F. D. Aaron *et al.* [H1 Collaboration], Phys. Lett. B **673** (2009) 119, arXiv:0901.0477 [hep-ex].

[4] **Events with Isolated Leptons and Missing Transverse Momentum and Measurement of W Production at HERA**, F. D. Aaron *et al.* [H1 Collaboration], arXiv:0901.0488 [hep-ex].

[5] **Strangeness Production at low Q^2 in Deep-Inelastic ep Scattering at HERA**, F. D. Aaron *et al.* [H1 Collaboration],

[6] F. D. Aaron *et al.* [H1 Collaboration], Eur. Phys. J. C **59** (2009) 589, arXiv:0808.1003 [hep-ex].

[7] F. D. Aaron *et al.* [H1 Collaboration], Phys. Lett. B **672** (2009) 219, arXiv:0810.3096 [hep-ex].

[8] F. D. Aaron *et al.* [H1 Collaboration], Phys. Lett. B **668** (2008) 268, arXiv:0806.3987 [hep-ex].

[9] F. D. Aaron *et al.* [H1 Collaboration], Phys. Lett. B **666** (2008) 131, arXiv:0805.4530 [hep-ex].

[10] Contributed papers by the H1-Coll. to ICHEP2008, 34th International Conference on High Energy Physics, Philadelphia, USA, 30/7 - 5/8 2008; papers are listed, which are not yet submitted to journals.

[11] **HERA I PDF Fit: Extraction of the proton parton density functions using a NLO-QCD fit of the combined H1 and ZEUS inclusive DIS cross sections** [10].

[12] **High Q^2 NC analysis using the complete HERA data** [10].

[13] **Inclusive and Multi-Jet Production at high Q^2 and determination of α_s using full HERA data** [10].

[14] **Diffractive photoproduction of jets with the H1 detector** [10].

[15] **Inelastic Photo-Production of J/Psi Mesons at HERA** [10].

[16] **Diffractive rho and phi production in DIS with the H1 detector** [10].

[17] **A search for Leptoquarks in ep collisions at HERA** [10].

[18] **A search for excited quarks in ep collisions at HERA** [10].

[19] **Multiparton interactions in photoproduction of dijets at H1** [10].

[20] **Prompt photons in photoproduction at HERA II** [10].

[21] **Measurement of the D^* production cross section in photoproduction with the H1 detector using HERA II data** [10].

[22] **Measurement of jet production in deep-inelatic ep scattering at low Q^2** [10].

[23] **Strangeness Production at low Q^2 in Deep-inelastic ep Scattering at HERA** [10].

[24] **Measurement of the Inclusive ep Scattering Cross Section at medium Q^2 and x at HERA** [10].

[25] **A Measurement of Beauty Photoproduction Through Decays to Muons at HERA-II** [10].

[26] **Charm Production at large Q^2 in deep inelastic electron-proton scattering at HERA** [10].

[27] **The Charm Fragmentation Function in DIS** [10].

[28] **D^* production at medium/low Q^2 with the H1 detector** [10].

[29] **Measurement of F_2^{cc} and F_2^{bb} using the H1 vertex detector at HERA** [10].

[30] **Extraction of the Charm Contribution to the Proton Structure Function F_2^C from $D^{*\pm}$ Measurements in Deep Inelastic Scattering at HERA** [10].

[31] **Leading Neutron production in DIS at HERA** [10].

[32] **Inclusive $K^{*\pm}$ production at low Q^2 at HERA** [10].

[33] **Search for a $D*$p resonance at HERA II** [10].

[34] Preliminary H1 results to be presented at the 2009 Workshop on Deep Inelastic Scattering (DIS 2009), Madrid, April 7-11, 2009; available at *http://www-h1.desy.de/publications/H1preliminary.short_list.html*.

[35] F. D. Aaron *et al.* [H1 Collaboration], Eur. Phys. J. C **54** (2008) 371, arXiv:0711.4578 [hep-ex].

[36] **Isolated photon production in deep-inelastic scattering at HERA**, Carsten Schmitz, PhD Thesis, University of Zürich (2007) available at http://www-h1.desy.de/publications/theses_list.html.

[37] Physik-Institut, University of Zürich, Annual Reports 1996/7 ff.; available at *http://www.physik.unizh.ch/reports.html*.

[38] V. Andreev *et al.* [H1 Collaboration], Phys. Lett. B **561** (2003) 241, arXiv:0301030 [hep-ex].

[39] C. Adloff *et al.* [H1 Collaboration], Eur. Phys. J. C **5** (1998) 575, arXiv:9806009 [hep-ex].

[40] S. Chekanov *et al.* [ZEUS Collaboration], Phys. Lett. B **559** (2003) 153, arXiv:0302010 [hep-ex].

[41] A. D. Martin, W. J. Stirling, R. S. Thorne and G. Watt, "Parton distributions for the LHC," arXiv:0901.0002 [hep-ph].

[42] R. S. Thorne, Phys. Rev. D **73** (2006) 054019, arXiv:0601245 [hep-ph].

[43] V. Blobel, "An unfolding method for high energy physics experiments," Proc. Advanced Statistical Techniques in Particle Physics, Durham (2002).

[44] T. Sjöstrand *et al.*, PYTHIA 6.2 Physics and Manual, arXiv:0108264 [hep-ph].

[45] M. Fontannaz, J. P. Guillet and G. Heinrich, Eur. Phys. J. C **21** (2001) 303.

[46] A. V. Lipatov and N. P. Zotov, Phys. Rev. D **72** (2005) 054002.

8 High-precision CP-violation Physics at LHCb

J. Anderson, R. Bernet, A. Büchler, N. Chiapolini, M. De Cian, V. Hangartner, C. Salzmann, S. Steiner, O. Steinkamp, U. Straumann, J. van Tilburg, M. Tobin, A. Vollhardt

in collaboration with: The silicon tracking group of LHCb: University of Lausanne; Max Planck Institute, Heidelberg, Germany; University of Santiago de Compostela, Spain; and Ukrainian Academy of Sciences, Kiev, Ukraine.

The full LHCb collaboration consists of 52 institutes from Brazil, China, France, Germany, Ireland, Italy, The Netherlands, Poland, Romania, Russia, Spain, Switzerland, Ukraine, the United Kingdom, and the United States of America.

(LHCb)

LHCb (1) is a dedicated B-physics experiment at the new 14 TeV proton-proton collider LHC at CERN. The main goal of LHCb is to perform precision measurements of CP violating processes in the B meson systems and to search for rare B decays. Unique triggering and particle-identification capabilities will enable LHCb to measure CP asymmetries in many different decay modes and to perform consistency tests of the Standard Model explanation of CP violation. Since CP violating asymmetries are generated by processes that involve internal loops of virtual particles, they are sensitive to contributions from new particles that are predicted in most extentions of the Standard Model. Measurements of these asymmetries therefore provide a powerful tool for searches of "new physics" beyond the Standard Model. They are complementary to the direct searches at the high energy frontier that will also be performed at the LHC.

Figure 8.1 shows a vertical cross section through the LHCb detector, which is layed out as a single-arm forward spectrometer. One of the crucial tasks in LHCb is the efficient and precise reconstruction of the trajectories and momenta of the charged particles that are generated in the decays of the B mesons. The tracking system consists of a silicon-microstrip vertex detector (VELO) and four planar tracking stations: TT (Tracker Turicensis) upstream of the LHCb dipole magnet and T1-T3 downstream of the magnet. The TT has an active area that is 160 cm wide and 130 cm high and is covered by four layers of silicon micro-strip detectors. In the much larger stations T1-T3, two detector technologies are employed: A 120 cm wide and 40 cm high region in the centre of the stations is covered with silicon micro-strip detectors (Inner Tracker, IT), whereas the outer part of these stations is covered by straw drift-tube detectors. Other components of the LHCb detector are two ring-imaging Cherenkov detectors (RICH1 and RICH2), calorimeters (SPD,PS,ECAL,HCAL) and muon chambers (M1-M5).

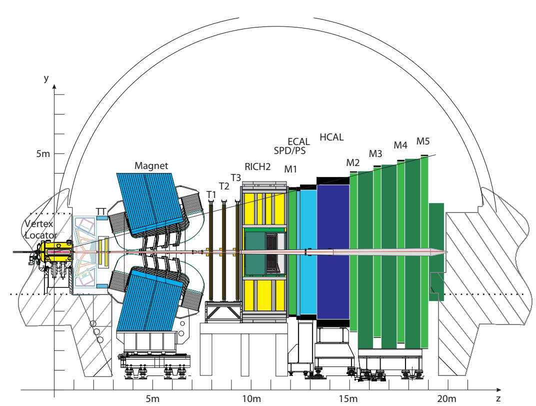

Figure 8.1: Vertical cross section through the LHCb detector.

The installation of the detector was essentially completed in 2008. By autumn 2008, the experiment was ready to record the first proton-proton collisions expected from the LHC. First beam-related events were indeed collected beginning of September during proton injection tests into the LHC ("TED runs"). A few days later, the commissioning of the accelerator was unfortunately interrupted by an incident involving the release of several tons of liquid Helium into the LHC tunnel. This incident resulted in a one-year delay in the startup of the LHC and first beams are now expected for autumn 2009. LHCb is using the additional time to fix minor problems, improve detector monitoring and operating procedures, and perform stress tests of the data acquisition system. Data collected during the TED runs has been used to test algorithms for the alignment of detector elements.

8.1 The Zürich Group in LHCb

Our group has played a leading rôle in the design, construction and operation of the LHCb Silicon Tracker (ST), which comprises TT (1; 2) and IT (3). The TT was entirely developed and constructed in Zürich. In addition, we have been responsible for the silicon sensors and for the optical readout link for both TT and IT.

The installation of the TT and the readout electronics was completed in spring 2008. Since then, a large fraction of our efforts has gone into the integration of the TT into the LHCb data acquisition and detector control systems, and the commissioning of the detector and its readout.

In addition to our contributions to the detector, we have started to participate in a number of simulation studies in preparation for physics analyses. We have continued our participation in the production of large samples of simulated data necessary for such studies, and we have worked on alignment algorithms for the TT.

8.2 Tracker Turicensis

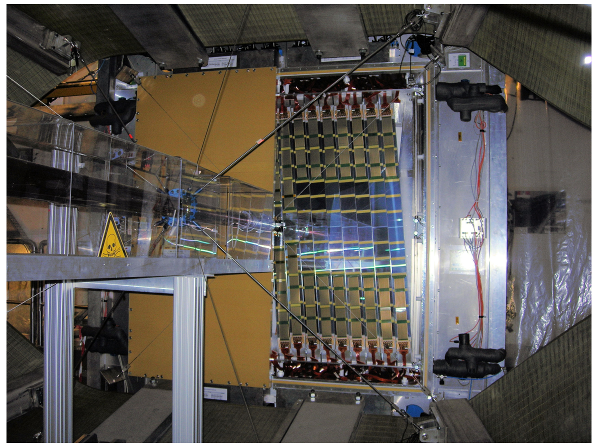

Figure 8.2: The TT viewed through the LHCb dipole magnet. One half of the detector box is open and the modules can be seen.

A photograph of the TT during its installation in LHCb is shown in Fig. 8.2. By the time of the expected startup of the LHC in September 2008, the detector was fully installed and more than 97% of the 143'000 detector channels were fully working.

The first beam-related signals in the TT were recorded during the TED runs early September 2008. J. van Tilburg, J. Anderson and A. Büchler led this effort, supported by other members of our group. The full detector was powered at nominal bias voltage and signal amplitudes were measured with varying time delays with respect to the beam trigger. The observed distributions (see Fig. 8.3) reflect the signal shape at the output of the pre-amplifier and are compatible with expectations from prototype beam tests.

These data were used to reconstruct particle trajectories through both VELO and TT. A clear signal was observed (see Fig. 8.4) which was used to train the alignment algorithms for the TT. C. Salzmann is working on this analysis under the supervision of J. van Tilburg.

Since September, the TT has been regularly operated and read out, both in stand-alone

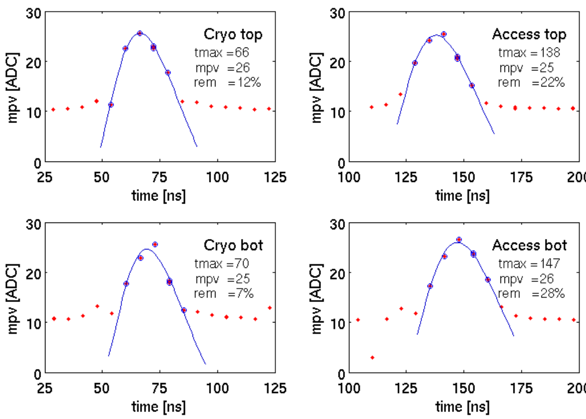

Figure 8.3: Results from the TED run. Shown are delay curves of the mean amplitude of the TT signals with respect to the beam time. The four panels correspond to different regions of the detector.

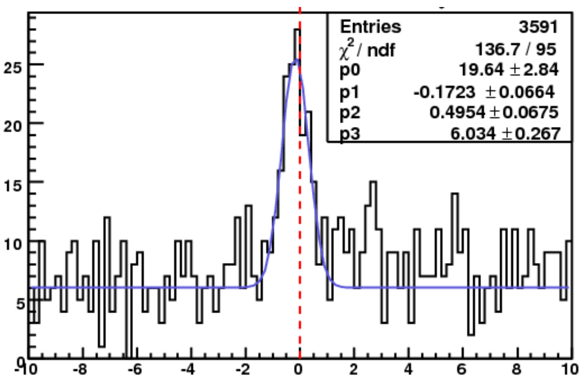

Figure 8.4: Residuals distribution (in mm) of hit positions measured in TT with respect to trajectories reconstructed with VELO. The observed position resolution is dominated by the uncertainties in the trajectory.

mode and in conjunction with other LHCb sub-detectors. These "dry runs" without beam absorb a significant amount of manpower but are vital for getting the detector into the best possible shape for the start-up of the LHC. Goals of this exercise are to gain experience in the operation of the detector, to improve user interfaces and to develop and test automated operation and monitoring procedures. This effort is organized by J. van Tilburg. J. Anderson, M. Tobin (who joined our group in February 2009), A. Büchler and C. Salzmann spend large fractions of their time at CERN to participate in these tests. N. Chiapolini contributes significantly to the development of online monitoring tools which were also adopted for other sub-detectors in LHCb. V. Hangartner is investigating the data to improve the understanding of the noise behaviour of the detector.

Another important goal of the commissioning effort is to "burn-in" the various components of the detector and to identify and replace weak components. Potentially the most serious problem we have encountered concerns a small number of detector modules on which a fraction of wire bonds has broken during operation in LHCb. The cause of this problem is under careful investigation to ensure it is not due to a principle design mistake which might cause it to appear on a larger number of modules later on. J. van Tilburg, S. Steiner and O. Steinkamp are involved in these investigations.

An easily fixed problem concerned the optical readout links for TT and IT. It had already been found during quality assurance tests in Zürich that a significant fraction of the VCSEL diodes used for the optical transmission had been damaged during the assembly of the electronics boards. These VCSELs showed a too low output and had to be replaced. During the readout tests in LHCb we found, however, that a number of faulty VCSELs had escaped detection during the acceptance tests. These VCSELs have meanwhile been replaced. At the same time some other minor modifications were implemented to further improve the operation stability of detector and readout. A. Vollhardt was in charge of these repairs, with help from S. Steiner.

8.3 Physics studies

We will focus on topics known from previous work that members of our group have done either in LHCb or elsewhere. Data from the TT will play an important rôle in all these analyses as position measurements in the TT significantly improve the momentum resolution for charged particles. This is crucial for the suppression of backgrounds, especially in measurements of rare decays, and for obtaining the excellent decay-time resolution required in time-dependent measurements of CP asymmetries in the B_s system.

We have chosen the following four physics topics:

- **The CP-violating phase β_s in $B_s\overline{B}_s$ mixing**
  This phase is very small in the SM (4) but could be enhanced in new-physics models due to virtual contributions of new particles. The most promising channel for measuring this phase is $B_s^0 \rightarrow J/\psi\phi$ since it is theoretically clean, has a relatively high branching fraction of $\approx 3 \times 10^{-5}$ and a clean experimental signature. However, the final state is not a CP eigenstate and a time-dependent angular analysis is required to statistically separate the CP-even and CP-odd contributions. A simulation study for this decay has been performed for LHCb showing that a measurement of $2\beta_s$ with a sensitivity of 0.030 using 2 fb^{-1} of data should be possible (5). The decay $B_s^0 \rightarrow J/\psi\eta'$ has a lower event yield than the mode $B_s \rightarrow J/\psi\phi$ but is a decay to a pure CP eigenstate so that no angular analysis is needed to disentangle the two CP contributions. A simulation study of this decay has been performed by D. Volyanskyy as part of his PhD thesis in our group. He found that a measurement of $2\beta_s$ with a sensitivity of 0.08 can be expected using 2 fb^{-1} of data (6). C. Salzmann will study these channels as part of his PhD thesis, supervised by J. van Tilburg.

- **Branching ratio of the rare decay $B_s \rightarrow \mu^+\mu^-$**
  This branching ratio is of order 10^{-9} in the Standard Model but can be significantly enhanced within specific extensions of the Standard Model. An LHCb simulation study has shown that assuming the Standard Model cross-section a 3σ observation should be possible using 2 fb^{-2} of data (7). A. Büchler has started to work on this analysis as part of her PhD thesis, supervised by J. van Tilburg. This study is a natural continuation of the work of R. P. Bernhard, who did an analysis of this channel at the D0 experiment as part of his PhD thesis (8) in our group.

- **$b \rightarrow s\ell^+\ell^-$ decays**
  These decays proceed through suppressed loops in the Standard Model and are therefore sensitive to contributions from new physics. One of the interesting observables is the forward-backward asymmetry, A_{FB}, which is defined through the angle between the ℓ^+ and the direction of flight of the B meson in the di-lepton rest frame. This asymmetry as a function of the di-lepton invariant mass can be predicted with small theoretical uncertainties. It can be measured in the exclusive decay channel $B_d \rightarrow K^\star\mu^+\mu^-$ and a study for LHCb has shown that a measurements of its zero-crossing with a sensitivity of 0.46 GeV^2 can be achieved using 2 fb^{-1} of data (9). Another interesting observable is the cross-section ratio of $b \rightarrow s\mu^+\mu^-$ and $b \rightarrow se^+e^-$ decays. In the Standard Model, this ratio is predicted to be close to unity, with theoretical uncertainties $<$ 1% (10). A measurement of this ratio will test the Standard Model as well as a variety of Minimum Flavour Violating extentions of the Standard Model, which predict a deviation of this ratio from unity that is closely related to the branching ratio of the rare decay $B_s \rightarrow \mu^+\mu^-$ (10). The measurement can be performed in the exclusive modes $B_u \rightarrow K\ell^+\ell^-$ and $B_d \rightarrow K^\star\ell^+\ell^-$. An LHCb study has shown that a measurement with

an uncertainty of $\approx 10\%$ can be expected using a dataset of 2 fb^{-1} (11). M. De Cian is investigating these channels as part of his PhD thesis work under the supervision of J. Anderson. These studies are a logical continuation of the work of A. Wenger, who studied the channel $B \to K^\star \mu^+ \mu^-$ at the D0 experiment as part of his PhD thesis, which he completed in our group end of 2008 (12).

- **Parton distributions in $\gamma^\star/Z \to \mu^+\mu^-$**
  Previous measurements of Parton distribution functions (PDFs) have been performed in fixed target experiments, at HERA, and at the Tevatron. For Z production at LHCb, the momentum fractions x carried by the two interacting partons are very asymmetric. A measurement of the Z cross-section will allow to improve the PDFs down to $x = 4.8 \times 10^{-5}$ and up to $x = 0.87$. By measuring di-muon production through Drell-Yan process at low invariant masses, LHCb will have the unique ability to measure PDFs down to $x \approx 10^{-6}$, exploring a totally unknown kinematic domain. Preparations for a measurement of the $Z \to \mu^+\mu^-$ cross-section are well advanced. J. Anderson worked on this channel as part of his PhD thesis work at UC Dublin before joining our group. He showed that systematic uncertainties are expected to be $\approx 1\%$ and that with an integrated luminosity of only 50 pb^{-1} a total cross-section measurement will already be systematics limited (see (13)). This is therefore a measurement for the early days of LHCb. Work on extending the analysis to the low mass region is still at an early stage. J. Anderson is interested in continuing these analyses together with a new PhD student. The measurement of PDFs is a logical continuation of the involvement of our group in similar measurements at H1 at HERA.

8.4 Outreach activities

In response to the growing public interest in the LHC, we have engaged in various outreach activities. A. Büchler participated in the "LHC first beam" event in September 2008, guiding journalists through the LHCb exhibition and control room. Also in September 2008, we had a joint exhibition stand with particle physicists from ETH at the "Nacht der Forschung" in Zürich. A. Büchler also appeared in the popular science programme "Einstein" on the Swiss public television channel SF1 (see Fig. 8.5).

Figure 8.5: Angela Büchler explaining the TT detector to journalist Monika Schärer, in the television programme "Einstein im CERN" [14].

8.5 Summary and Outlook

The installation of the LHCb experiment in general, and of the Tracker Turicensis in particular, is completed and the commissioning of the detector is well advanced. We are looking forward to the first beams from the LHC, which are now expected for autumn 2009. The commissioning of the detector with beams will still take up a significant fraction of our resources for the coming year, but event reconstruction and physics analyses are playing a more and more important rôle.

[1] A. A. Alves et al. (LHCb Collaboration), JINST **3**, S08005 (2008).

[2] J. Gassner, M. Needham, O. Steinkamp,
Layout and expected performance of the LHCb TT station, LHCb note 2003-140.

[3] LHCb Inner Tracker Technical Design Report, CERN/LHCC 2002-029.

[4] CKMfitter 2008, see webpage.

[5] G. Lanfranchi,
Search for new physics in $B_s \to J/\psi\phi$ decay at LHC, CKM workshop, Rome, Italy, September 9-12 (2008).

[6] D. Volyanskyy, The Trigger Tracker and a Monte Carlo Study of the $B_s \to J/\psi\eta'$ Decay in the LHCb Experiment, PhD thesis, Universität Zürich (2007).

[7] D. Martinez et al., LHCb potential to measure/exclude the branching ratio of the decay $B_s \to \mu^+\mu^-$,
LHCb note 2007-028 (2007).

[8] R. .P. Bernhard,
Search for rare decays of the B_s^0 meson with the D0 experiment, PhD thesis, Universität Zürich (2006).

[9] J. Dickens et al., LHCb note 2007-033.

[10] G. Hiller and F. Kruger, Phys. Rev. D69, 074020 (2004).

[11] P. Koppenburg, LHCb note 2007-034 (2007).

[12] A. Wenger,
Search for the Rare Decays $B^\pm \to K^\pm\mu^+\mu^-$ and $B^0 \to K^\star\mu^+\mu^-$ with the D0 experiment,
PhD thesis, Universität Zürich (2008).

[13] J. Anderson,
Testing the electroweak sector and determining the absolute luminosity at LHCb using dimuon final states,
PhD thesis, University College Dublin (2007);
J. Anderson and R. McNulty,
Measuring $\sigma_Z \cdot Br(Z \to \mu^+\mu^-)$ at LHCb,
LHCb note 2007-114 (2007).

[14] "Einstein im CERN", 26.02.2009, podcast on www.sf.tv/
sendungen/einstein/sendung.php?docid=20090226

9 Particle physics with CMS

E. Alagöz, C. Amsler, V. Chiochia, Hp. Meyer, B. Millan Mejias, C. Regenfus, P. Robmann, J. Rochet, T. Rommerskirchen, A. Schmidt, S. Steiner, D. Tsirigkas, and L. Wilke

In collaboration with: Paul Scherrer Institut (PSI) and the CMS Collaboration

The silicon pixel detector is the innermost component of the CMS apparatus (1) at the LHC, with which a precise reconstruction of charged particles and secondary vertices from heavy quark decays will be performed. The barrel pixel detector (48 million pixels) consists of three cylindrical layers at radii of 4.4 cm, 7.4 and 10.2 cm, with a length of 53 cm. Four forward disks (18 million pixels) are located along the beam axis, two on each side (18 million pixels) at $\pm$34 cm and $\pm$47 cm from the collision point.

We were involved in the design, construction and commissioning of the barrel pixel detector. We have provided equipment and have led prototype tests on CERN beams (2; 3; 4), measuring sensor performances such as position resolution, detection efficiency, charge sharing and Lorentz deflection, before and after irradiation. We have also contributed to the development and commissioning of the readout chip (ROC) (5). We have developed and built in the Institute workshop the mechanical and cooling structure and the two service tubes which provide the coolant and power, and transfer the signals to and from the pixel detector (6).

In 2008 we continued the analysis of the test beam data taken in 2006. We had used a telescope with pixel sensors (150 μm $\times$ 100 μm pixels), two in front and two behind the irradiated pixel detector under test. Irradiated sensors were kept at -10°C in a cooling box with Peltier elements. The pixels were bump-bonded to the final CMS pixel readout chips. The apparatus was located in a Helmholtz superconductor 3T magnet and exposed to a 150 GeV π^--beam.

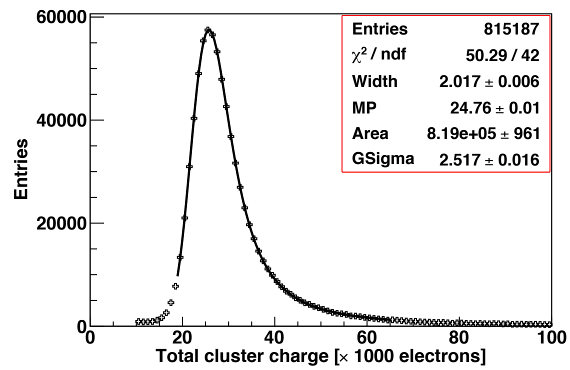

Figure 9.1: Cluster charge distribution for the un-irradiated sensor. The solid line is a Gaussian convoluted Landau fit (from [4]).

The charge distribution of an un-irradiated sensor operated at 150 V bias voltage in a 3T magnetic field is shown in Fig. 9.1. The solid line is the Gaussian convoluted Landau fit. The most probable value for the cluster charge is around 24'760 electrons. For irradiated pixels one observes a charge loss which is partially recovered by applying higher bias voltages. The collected charge is reduced to 77% (38%)

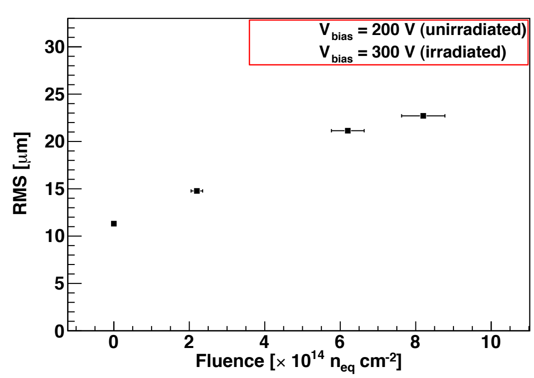

Figure 9.2: Position resolution as a function of irradiation fluence for perpendicular incidence (from [4]).

for a fluence of $2.2{\times}10^{14}$ ($8.2{\times}10^{14}$) $\mathrm{n_{eq}cm^{-2}}$. The spatial resolution as a function of irradiation fluence is shown in Fig. 9.2. The degradation in the position resolution is due to charge loss as a result of radiation damage. In addition, the higher bias voltage reduces the Lorentz angle, leading to reduced charge sharing among adjacent pixels.

We have developed reconstruction and physics analysis software, in particular track and vertex reconstruction (7; 8), and constraining kinematic fits (9). This activity continues with the development of b-tagging algorithms (10). We plan to exploit the first data from LHC for a study of $B_s \to J/\psi\ \phi$ (11; 12) and for a measurement of the $t\bar{t}$-cross section (13). More information and related publications can be found in previous annual reports.

We are also preparing a search for supersymmetry in dijet events (14). The study is focused on the SUSY parameter space where squarks are pair-produced and both decay into a quark and a neutralino. The latter escapes undetected and gives rise to missing energy. Although the background from QCD dijet events is overwhelming, powerful discriminating variables can be found due to the particular kinematics of SUSY events. This should enable results already with early collision data.

CMS (and the other LHC experiments) will produce enormous amounts of data to be processed and analyzed. This will be achieved by tiered computing architectures, dividing the data streams and processing tasks among several computing centers. The Tier-0 center is located directly at the experiment. A small number of Tier-1 centers perform the first steps of re-processing. The skimmed data are accessible from Tier-2 centers (CSCS at Manno for us) and Tier-3 centers (PSI for us). The final stage of analysis is usually performed locally with small Tier-4 clusters, managed by the research groups themselves.

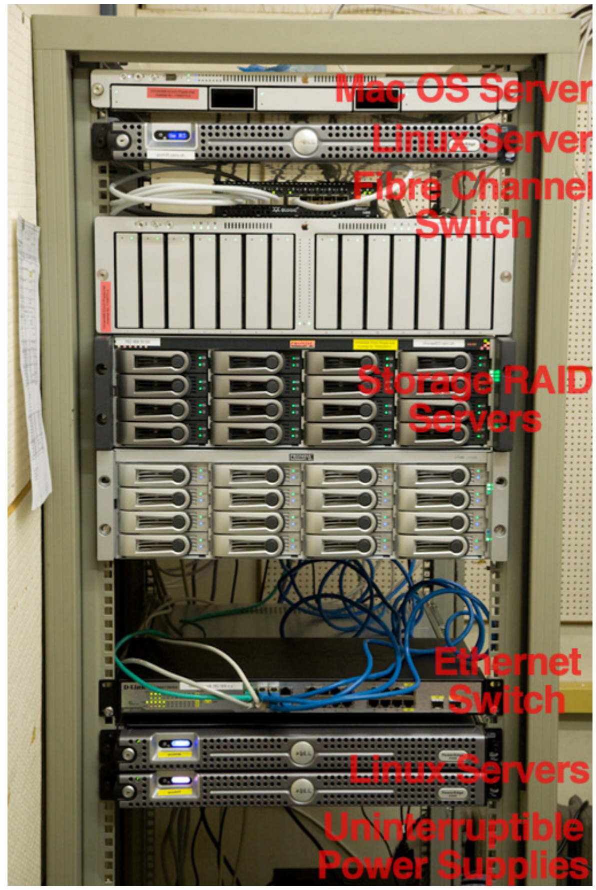

Figure 9.3: One of the two racks of the UZH computing cluster. Visible are the 35 TeraByte storage RAID servers and three of the Linux servers, as well as some switching and cabling infrastructure.

During 2008 we purchased and installed our own computing cluster at CERN. It consists of 28 CPU cores running at 3 GHz and 35 TeraByte of redundant (RAID) storage space, connected via a high-speed Fiber Channel Network. Efficient and easy access to all CERN services is available, since the whole cluster is located inside of the CERN network. Figure 9.3 shows a photograph of one of the two racks of the cluster. The computing nodes are running the Scientific Linux (SLC4) average operating system, and the data storage is mounted on each computing node via the network file system (NFS). An air conditioning system was installed to provide the necessary cooling power to keep the room temperature well below 30 degrees. Uninterruptible power supplies prevent potential damage caused by the frequent power glitches and outages at CERN. Our computing cluster was already used for the cosmic runs in 2008.

We are responsible for the implementation, maintenance and validation of the barrel pixel geometry in the Monte-Carlo simulation. The description in the simulation (6) needs to be as precise as possible to reproduce the exact amount of material interactions. Such interactions deteriorate the trajectories of particles and influence the measurements in the outer detectors (strip tracker, calorimeters and muon detectors). Figure 9.4 shows for example the material thickness in the CMS tracker as a function of pseudorapidity which reveals the relatively large thickness in the regions of pseudorapidity $1 < \eta < 1.5$. The weight of the pixel detector implemented in the Monte-Carlo simulation has been compared with its real weight and the agreement was found to be within 6%.

The innermost layer of the pixel detector provides information on secondary vertices and impact parameters for b- and τ-decays which are relevant to Higgs searches. Studies of impact parameter resolution, track seeding, b- and τ-tagging efficiency will be performed. Before physics research can start, tasks such as software detector alignment and calibration need to be performed during the early phase of detector operation. Detector alignment, crucial for vertex reconstruction and b-tagging, is expected to improve with time and luminosity.

We have simulated the expected efficiency of identifying b-jets ("b-tagging efficiency") for various degrees of detector alignment (Fig. 9.5). At startup only information from survey measurements and cosmic muon tracks can be used to perform the detector alignment. At 10 pb^{-1} the tracker can be aligned by using hadrons and muons from the decays of low mass resonances such as J/ψ and Υ. At 100 pb^{-1} high p_T muons from Z- and W-boson decays become available, at which time the misalignment of the pixel tracker is expected to be around 20μm. The tracker is finally aligned with an integrated luminosity of 1 fb^{-1} which can be achieved within one year of detector operation.

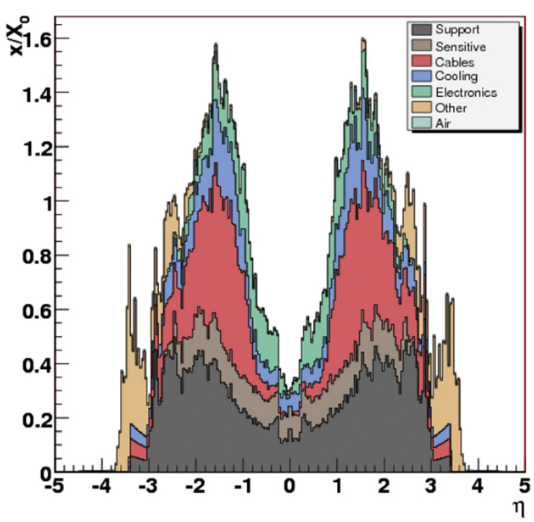

Figure 9.4:
Material thickness X (in radiation lengths X_0) in the CMS tracker, as a function of pseudorapidity η.

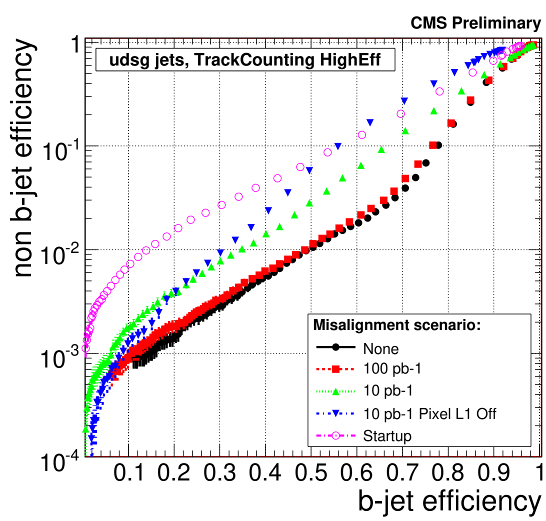

Figure 9.5: Expected misidentification efficiency versus b-jet tagging efficiency for different values of integrated luminosity with corresponding improvements in detector alignment.

The Monte-Carlo simulation then needs to be tuned according to detector performance. Large amounts of events need to be simulated using our Tier-3 facility at PSI. The simulation is time consuming (up to two minutes on a modern CPU and hundreds of millions of events are needed). A fast Monte-Carlo simulation is provided which uses parametrizations based on the full simulation and a simplified detector geometry (10; 15). The fast simulation is 100 – 1000 $\times$ faster than the full simulation.

The construction and installation of the pixel detector was completed in 2008 and operation started with beam on 10 September. Following the incident on 19 September, the detector was commissioned with cosmic ray data. Some 300 million events were collected until the end of the year. Data was taken without magnetic field ("CRUZET" data) and with 3.8 T ("CRAFT " data). With magnetic field turned on about 80′000 events had a muon crossing the pixel detector. Figure 9.6 shows one of the cosmic ray events. The various CMS subdetectors could be aligned with these data and the detection efficiencies measured. In particular, 99% (96%) of the barrel (forward) pixels was found to be operational.

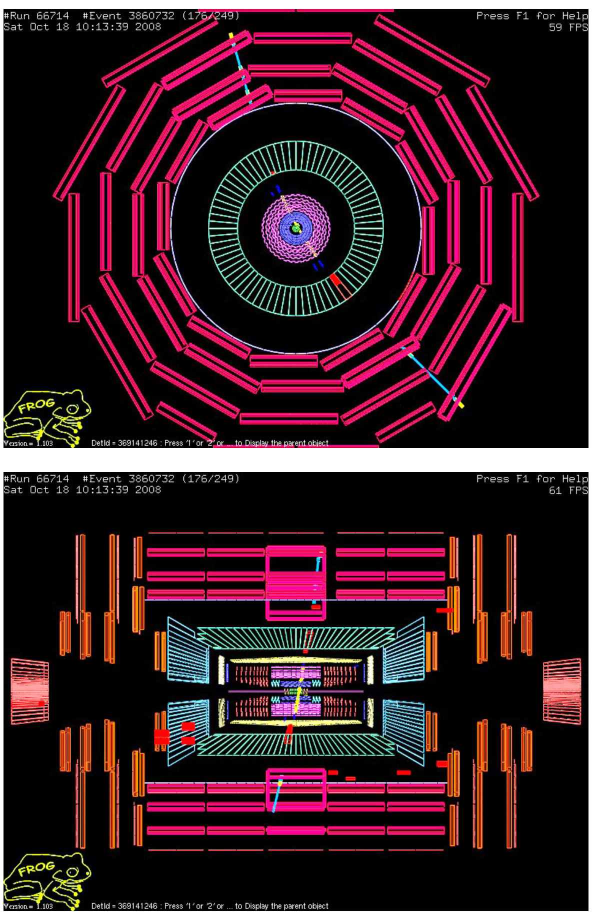

Figure 9.6: A spectacular event display showing a cosmic muon crossing CMS and the pixel detector.

The tracking performance of the CMS detector depends crucially on the alignment of the tracking devices, in particular of the pixel detector. Different alignment techniques are being used. In one method we use cosmic ray tracks traversing the pixel detector. For the pattern recognition this leads to two tracks emerging from the detector center. In a first step we use the outer strips from the tracker to determine the trajectories and to compute the difference (residuals) between the predicted and measured hits in the pixel detector. This is done for every sensor module. The average residual is then determined and used to align the detector.

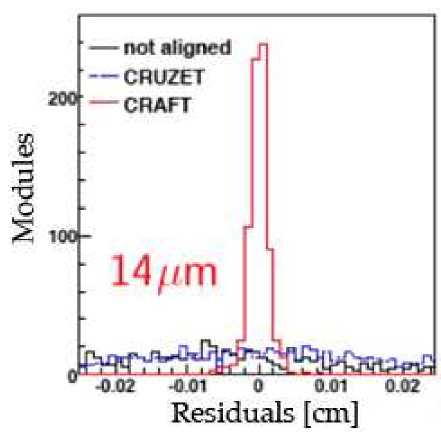

Figure 9.7: Average residuals for the barrel pixels before and after alignment with cosmic rays with field off (blue) and field on (red).

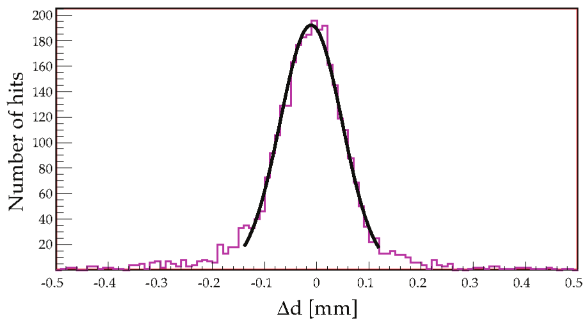

Figure 9.8: Distribution of the difference Δd between the distances to the detector axis for the two half tracks originating from a high momentum cosmic muon.

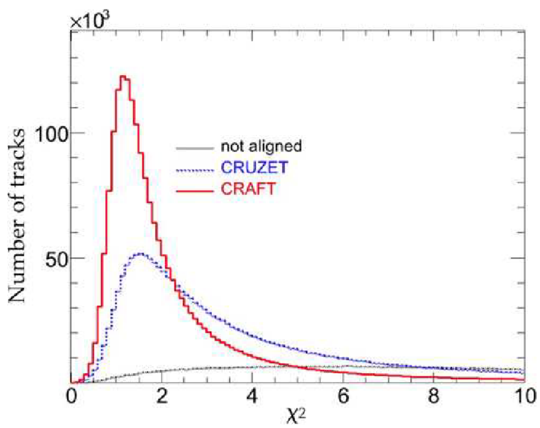

Figure 9.9: χ^2-distribution for reconstructed cosmic ray tracks, before and after alignment without magnetic field (CRUZET) and with magnetic field (CRAFT).

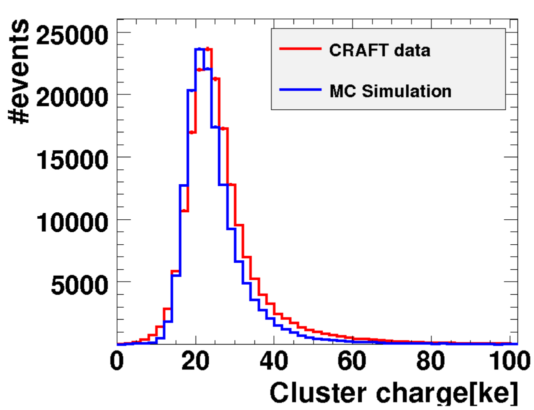

Figure 9.10: Distribution of the cluster charge measured in the barrel pixel detector.

Figure 9.7 shows the distribution of the average residuals for the barrel pixels before and after alignment. The accuracy on the alignment is around 14 μm r.m.s. Figure 9.8 shows the difference of distances to the detector axis after detector alignment with cosmic rays of more than 20 GeV/c transverse momentum, which is a measure for the impact parameter resolution. The r.m.s resolution on the impact parameter is 59 $\pm$ 1 μm. Figure 9.9 shows the spectacular improvement on the track reconstruction that could already be achieved with cosmics (described below). However, since cosmic rays are mostly vertical, the alignment of detectors lying in the horizontal plane will have to be performed with collision data.

Studying the differences between simulation and data helped to improve our understanding of the pixel detector. One of the most important variables is the cluster charge. Several effects have been identified which are not be reproduced in Monte-Carlo simulations, such as the dependence of the readout time on the signal amplitude. These effects have been studied extensively. Figure 9.10 shows the cluster charge distribution after selection cuts, as measured with field on (CRAFT) in the barrel pixel detector. The simulation reproduces already quite well the peak-position and the measured width.

In the 3.8 T field of CMS the electrons produced by a charged particle passing through the pixel detector drift perpendicularly to the magnetic field in the sensor (Fig. 9.11). This leads to a non-vanishing

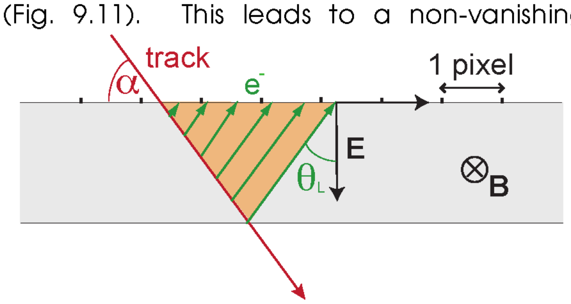

Figure 9.11: Lorentz angle θ_L (from [11]).

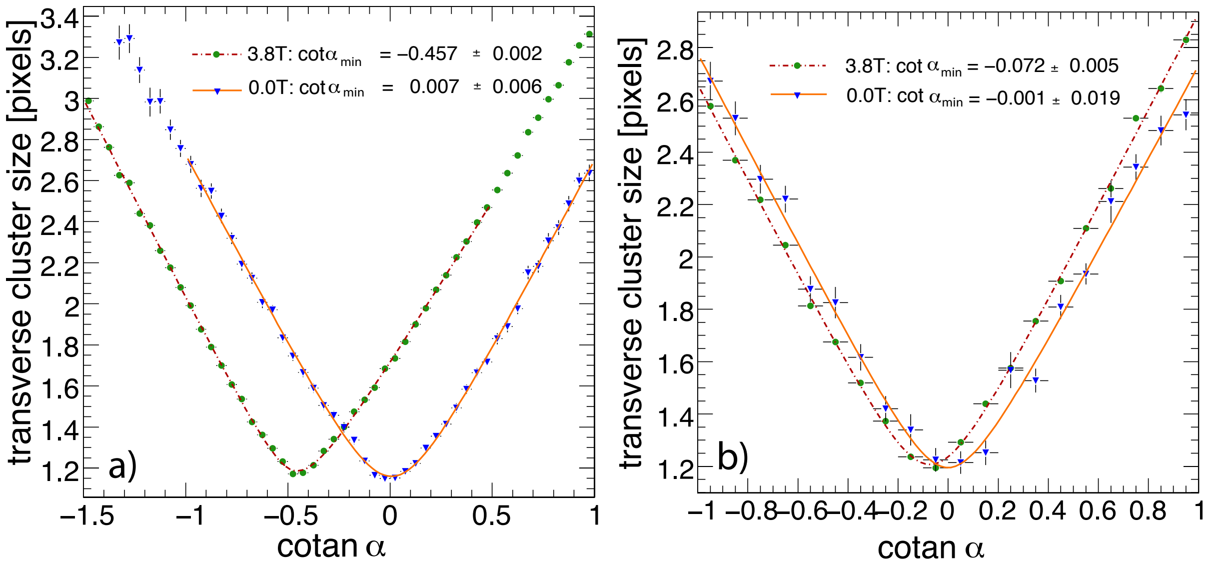

Figure 9.12: Measured cluster size as a function of incidence angle α for un-irradiated pixels. The predictions (lines) are compared to data at 3.8 T (circles) and 0 T (triangles) for the barrel (a) and forward (b) pixel detector. Only statistical errors are shown (from [11]).

Lorentz angle θ_L and hence a shift of the hit coordinate. The correction (up to 120 μm) will decrease as a function of time. This is due to the increasing bias voltage needed to compensate for radiation damage (see below). Furthermore, since the irradiation is not uniform across the detector, each module will evolve differently. The Lorentz angle will therefore be estimated directly from data. With collision data this is done by comparing the observed shapes of charged clusters with the reconstructed tracks in the tracker (16).

Meanwhile we have determined θ_L from cosmic rays. The spread of the charge distribution over neighboring pixels depends on the particle incidence angle α and is minimum when the particle flies along the drift direction (when α = 90° + θ_L, see Figs. 9.11 and 9.12). Hence θ_L is measured by finding the minimum of the mean cluster size distribution, measured as a function of track incidence angle. The barrel pixel detector modules are perpendicular to the magnetic field while the forward modules are inclined by α = 20° relative to the magnetic field, leading to in a much lower value θ_L for the forward detector. The results (Fig. 9.12) are then compared to the PIXELAV simulation (17) of the pixel detector. The measured values agree well with the predicted values (see also Table 9.1). Cosmic data without magnetic field (for which θ_L = 0) are used as a consistency check.

Table 9.1: Measured values for $\tan\theta_L$ at 3.8 T for un-irradiated pixels, compared with expectations for the barrel and forward pixel detectors.

	$\tan\theta_L$ measurement	$\tan\theta_L$ PIXELAV prediction
barrel	$-0.457(2)$	$-0.452(2)$
forward	$-0.072(5)$	$-0.080(5)$

Operation with cosmic rays will resume in summer 2009 while first collisions with 10 TeV protons are expected in autumn.

[1] S. Chatrchyan *et al.* (CMS Collaboration), Journal of Instrumentation **3** (2008) S08004.

[2] Y. Allkofer *et al.*, Nucl. Instr. Meth. in Phys. Research **A 584** (2008) 25.

[3] V. Chiochia *et al.*, Nucl. Instr. Meth. in Phys. Research **A 568** (2006) 51; V. Chiochia *et al.*, IEEE Trans. Nucl. Sci. **52** (2005) 1067.

[4] E. Alagöz, PhD Thesis (in preparation).

[5] C. Hörmann, PhD Thesis, Universität Zürich (2006).

[6] C. Amsler *et al.*, submitted to Journal of Instrumentation.

[7] R. Frühwirth and T. Speer, Nucl. Instr. and Meth. in Phys. Res. **A 534** (2004) 217.

[8] R. Frühwirth, K. Prokofiev, T. Speer, P. Vanlaer and W. Waltenberger, Nucl. Instr. Meth. in Phys. Res. **A 502** (2003) 699.

[9] K. Prokofiev, PhD Thesis, Universität Zürich (2005).

[10] A. Schmidt, Nucl. Phys. B - Proceedings Supplements **187** (2009) 216.

[11] L. Wilke, PhD Thesis (in preparation).

[12] B. Millan Mejias, PhD Thesis (in preparation).

[13] D. Tsirigkas, PhD Thesis (in preparation).

[14] T. Rommerskirchen, PhD Thesis (in preparation), CMS Note PAS SUS-08-005.

[15] A. Schmidt, 2008 IEEE Nuclear Science Symposium Conference Record (2008) 2795.

[16] L. Wilke, V. Chiochia, T. Speer, CMS Note 2008/012.

[17] M. Swartz, Nucl. Instrum. Meth. **A 511** (2003) 88.

10 Superconductivity and Magnetism

M. Bendele (since January 2009), D.G. Eshchenko (till January 2009), H. Keller, F. La Mattina (till June 2008), A. Maisuradze (till May 2008), P. Prem (since January 2009), J. Roos, S. Strässle, St. Weyeneth, B.M. Wojek, C. Duttwyler (Master student), U. Mosele (Master student, till August 2008)

Visiting scientists: M.V. Eremin, B. Graneli, V.A. Ivanshin, R. Puzniak, A. Shengelaya
Emeritus members: K.A. Müller (Honorarprofessor), T. Schneider (Titularprofessor), M. Mali

in collaboration with:
ETH Zürich (J. Karpinski), Paul Scherrer Institute (K. Conder, R. Khasanov, E. Morenzoni), Max-Planck-Institute for Solid State Research Stuttgart (A. Bussmann-Holder), IBM Rüschlikon Research Laboratory (J.G. Bednorz, S.F. Alvarado), University of Geneva (Ø. Fischer, J.M. Triscone), University of Rome (D. Di Castro), Kazan State University (A. Dooglav, M.V. Eremin, V. Ivanshin, B.I. Kochelaev), Polish Academy of Sciences (R. Puzniak), University of Belgrade (I.M. Savić), Tbilisi State University (A. Shengelaya), Iowa State University (A. Kaminski).

During the reporting period we continued our research activities in the field of novel electronic materials. We investigated their magnetic and electronic properties by combining experiments using microscopic tools, such as muon-spin rotation (μSR), electron paramagnetic resonance (EPR), nuclear magnetic resonance (NMR), nuclear quadrupole resonance (NQR), and the more macroscopic techniques of SQUID and torque magnetometry. From our various investigations we present in the following three studies which are currently of highest interest in this research field.

10.1 Oxygen isotope effects within the phase diagram of cuprates

In 1990 our group started a project on isotope effects in cuprate high-temperature superconductors (HTS's) which was initiated by K. Alex Müller. Several novel oxygen isotope (^{16}O/^{18}O) effects (OIE's) on different quantities in cuprates were observed by our group, such as on the transition temperature T_c (including site-selective OIE), the in-plane magnetic penetration depth $\lambda_{ab}(0)$ (including site-selective OIE), the anisotropy parameter γ, the pseudogap temperature T^*, the charge-ordering temperature T_{co}, the superconducting energy gap Δ_0, the Néel temperature T_N, the spin-glass freezing temperature T_g, and the EPR line width Γ (1; 2; 3; 4). These unconventional OIE's were detected in different cuprate HTS families by using various types of samples (powders, single crystals, films) and experimental techniques (SQUID, magnetic torque, μSR, EPR, XANES, neutron scattering).

Cuprate HTS's exhibit a rich phase diagram (Fig. 10.1). The undoped parent compounds are characterized by a long range 3D antiferromagnetic (AFM) order, which is rapidly destroyed when holes are doped into the CuO_2 planes. Short-range AFM correlations survive, however, well in the superconducting (SC) region of the phase diagram by forming a spin-glass (SG) state. Upon the onset of superconductivity this phase persists for a limited doping range, suggesting that SC and SG phases coexist within a certain doping range. With increasing doping, the superconducting transition temperature T_c increases. Correspondingly, four phases can be differentiated: the AFM phase, the SG phase, the SG+SC phase, and the SC phase. How these phases are related to each other is an open and controversial issue, and until now experiments are missing which could provide a fundamental link between them. In particular, it is very interesting to investigate the OIE's on the corresponding transition temperatures between the various phases.

Years ago we observed a huge OIE on the spin-glass freezing temperature T_g in $La_{2-x}Sr_xCu_{1-z}Mn_zO_4$ ($x = 0.03$ and 0.05; $z = 0.02$) by means of μSR (5). This is a clear signature that the spin dynamics in cuprates are ultimately correlated with lattice vibrations.

Recently, we performed a detailed OIE study of the various phases (SC, SG+SC, SG, AFM) in the prototype cuprate system $Y_{1-x}Pr_xBa_2Cu_3O_{7-\delta}$ by means of μSR and magnetization experiments (6). These techniques have the advantage of being direct, bulk sensitive, unambiguous, and able to measure T_c as well as T_g in the region where both coexist. The results are sumarized in Figs. 10.1 and 10.2 (6).

All phases exhibit an OIE which is strongest, where the respective phase terminates. Note that the OIE on the magnetic phases (SG and AFM) are sign reversed as compared to the one on the superconducting phase. Another interesting anti-correlation is observed in the region where spin-glass magnetism coexists with superconductivity (SG+SC). Here a small OIE on T_c corresponds to a large OIE on T_g in sequence and vice versa. This behavior suggests that in this regime phase separation sets in where the superfluid density coexists with a SG related one. Since the isotope effect on T_c can be accounted for through polaron formation (7), the one on T_g is expected to originate from the same physics. By relating the AFM transition temperature to the metal-insulator transition, a reduction in kinetic energy caused by polaron formation is proposed to explain this OIE as well. The various OIE's reported here, clearly evidence that lattice effects are effective in all phases of cuprate superconductors and impose serious constraints on theories for cuprate superconductivity.

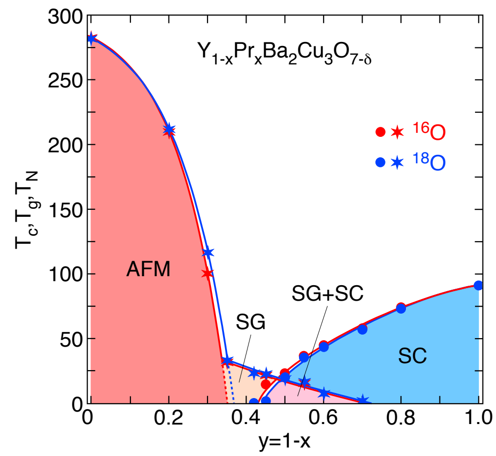

Figure 10.1: Dependence of the superconducting transition (T_c), the spin-glass ordering (T_g), and the antiferromagnetic ordering (T_N) temperatures for $^{16}O/^{18}O$ substituted $Y_xPr_{1-x}Ba_2Cu_3O_{7-\delta}$ on the Pr content x. The solid lines are guides to the eye. The areas denoted by "AFM", "SG", and "SC" represent the antiferromagnetic, the spin-glass, and the superconducting regions, respectively. "SG+SC" corresponds to the region where spin-glass magnetism coexists with superconductivity. After [6].

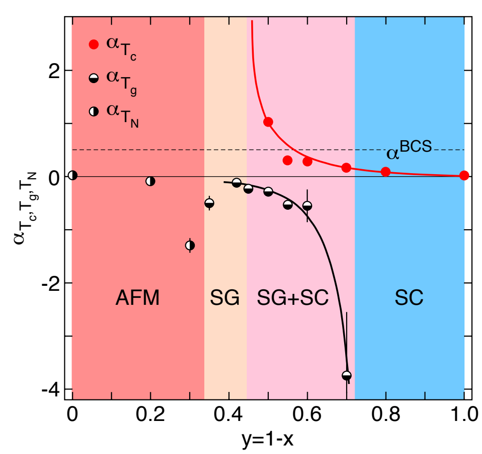

Figure 10.2:
OIE exponents α_{T_c}, α_{T_g}, and α_{T_N} for $^{16}O/^{18}O$ substituted $Y_xPr_{1-x}Ba_2Cu_3O_{7-\delta}$ as a function of the Pr content x. The dashed line corresponds to $\alpha_{T_c}^{BCS}$=0.5. The solid lines are guides to the eye. The meaning of the areas denoted by "AFM", "SG", "SG+SC", and "SC" are the same as in Fig. 10.1. After [6].

[1] D. Zech, H. Keller, K. Conder, E. Kaldis, E. Liarokapis, N. Poulakis, and K.A. Müller, Nature (London) **371**, 681 (1994).

[2] G.-M. Zhao, M.B. Hunt, H. Keller, and K.A. Müller, Nature (London) **385**, 236 (1997).

[3] G.-M. Zhao, H. Keller, and K. Conder J. Physics: Condens. Matter **13**, R569 (2001).

[4] H. Keller, in *Superconductivity in Complex Systems*, Structure and Bonding Vol. **114**, eds. A. Bussmann-Holder and K.A. Müller (Springer-Verlag Berlin Heidelberg 2005), pp. 143-169.

[5] A. Shengelaya, G.-M. Zhao, C. Aegerter, K. Conder, I.M. Savić, and H. Keller, Phys. Rev. Lett. **83**, 5142 (1999).

[6] R. Khasanov, A. Shengelaya, D. Di Castro, E. Morenzoni, A. Maisuradze, I.M. Savić, K. Conder, E. Pomjakushina. A. Bussmman-Holder, and H. Keller, Phys. Rev. Lett. **101**, 077001 (2008).

[7] A. Bussmann-Holder and H. Keller, in Polarons in Advanced Materials, ed. A.S. Alexandrov (Springer Series in Materials Science 103, Canopus Publishing, Bristol 2007), pp. 599-621.

10.2 Temperature dependent anisotropy parameter in the novel iron-pnictide superconductors

Since the discovery of high-temperature superconductivity in the cuprate superconductors, much effort has been spent on finding similar superconducting transition-metal based oxides. The discovery of superconductivity at $T_{\rm c} \simeq 26$ K for $LaFeAsO_{1-x}F_x$ (La1111) in 2008 by Hosono and coworkers triggered great interest in the scientific community (1). Soon after, by substituting La with other lanthanide ions like Ce, Pr, Nd, Sm, Gd, Tb, and Dy, a series of novel superconducting materials was synthesized with T_c's up to 56 K (2).

All these iron-pnictide superconductors have a layered crystal structure containing Fe_2As_2-sheets, where the Fe ions are arranged on simple square lattices (1). Superconductivity takes place in the Fe_2As_2-layers, whereas the spacing layers are charge reservoirs when doped with holes or electrons. These novel iron-based superconductors are in many respects similar to the cuprates, and it is interesting to compare their physical properties. However, in order to investigate the anisotropic properties of these superconductors, single crystals of high quality are required. In the last year we performed a detailed study of the anisotropy parameter in single crystals of the Ln1111 (Ln= Lanthanide) family by means of torque magnetometry (3; 4).

High quality single crystals of the Ln1111 family were grown using the cubic anvil high-pressure technique at ETH Zurich (5). The rectangular plate-like crystals have typical masses of 0.1 - 6 μg. The crystal structure was checked by means of X-ray diffraction revealing the c axis to be perpendicular to the plates. Selected crystals were characterized in a SQUID magnetometer.

In order to investigate the anisotropic properties of the Ln1111 family, we studied the angular dependence of the superconducting torque in a tilted magnetic field with respect to the crystallographic axes. The torque was found to be best described by using a two-anisotropy model (6), where the anisotropy of the magnetic penetration depth $\gamma_\lambda = \lambda_c/\lambda_{ab}$ and the anisotropy of the upper critical field $\gamma_H = H_{\rm c2}^{ab}/H_{\rm c2}^{c}$ enter distinctly into the theoretical description of the data. Here λ_i and $H_{\rm c2}^i$ denote the magnetic penetration depth and the upper critical field of the material, respectively, with the magnetic field oriented along the crystallographic i axis. Some examples of angular dependent torque data are depicted in Fig. 10.3.

The final result of this anisotropy study for three different crystals of the compounds $SmFeAsO_{0.8}F_{0.2}$ and $NdFeAsO_{0.8}F_{0.2}$ with $T_{\rm c}$'s

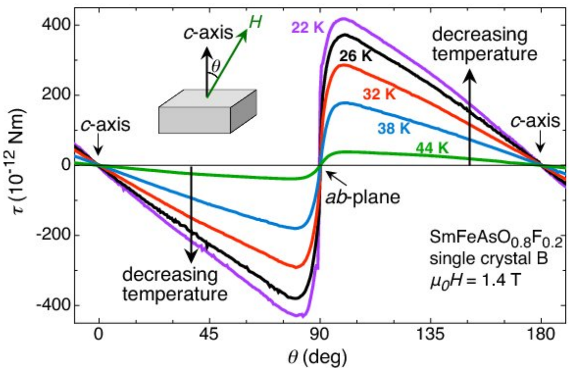

Figure 10.3: Angular dependence of the reversible torque data for $SmFeAsO_{0.8}F_{0.2}$ at several temperatures derived in a magnetic field of 1.4 T. For clarity not all measured data are shown.

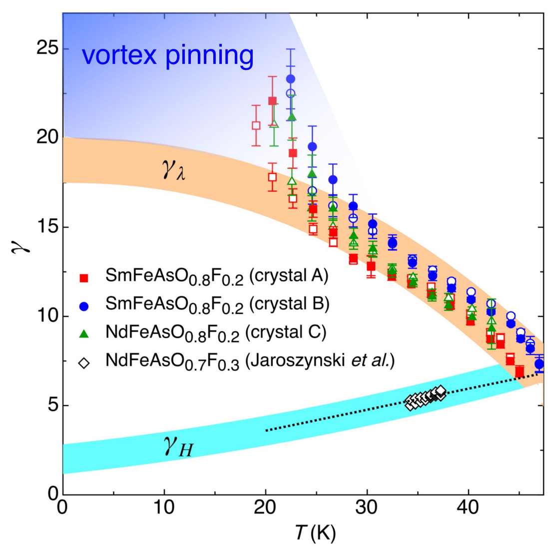

Figure 10.4: Summary of the systematic analysis of the torque data of single crystals $SmFeAsO_{0.8}F_{0.2}$ (crystal A and B) and $NdFeAsO_{0.8}F_{0.2}$ (crystal C). Values of γ (open symbols) and γ_λ (closed symbols) were obtained from fits to the data. The upper broad orange band is a guide to the eye, suggesting an estimate of $\gamma_\lambda(0) \approx 19$. The dotted line is the linear extrapolation of γ_H obtained from resistivity measurements [7] on a $NdFeAsO_{0.7}F_{0.3}$ single crystal with similar $T_c \simeq 45$ K (diamonds). The lower broad blue band is a guide to the eye, suggesting an estimate of $\gamma_H(0) \approx 2$. At low temperatures, the fitted anisotropy exceeds the guide to the eye, since substantial pinning contributions to the torque influence the determination of the anisotropy parameter.

in the range of 45 K is summarized in Fig. 10.4. We found strong evidence that the two anisotropies γ_λ and γ_H are different and depend strongly on temperature (3; 4). This implies that superconductivity in the oxypnictides is unconventional, since for conventional Ginzburg-Landau superconductors, the anisotropy parameter is a unique quantity, independent on temperature and field. Torque magnetometry in low magnetic fields is very sensitive to γ_λ which exhibits a pronounced increase with decreasing temperature. This is in contrast to the behavior of γ_H which according to recent resistivity measurements decreases with decreasing temperature (7). Close to T_c both anisotropies have very similar values of $\gamma_\lambda(T_c) \approx \gamma_H(T_c) \approx 7$, whereas at low temperatures the magnetic penetration depth anisotropy $\gamma_\lambda(0) \approx 19$ and the upper critical field anisotropy $\gamma_H(0) \approx 2$. This behavior is similar to that in the two-band superconductor MgB_2 (although $\gamma_\lambda(T)$ and $\gamma_H(T)$ have reversed slopes) where the temperature dependences of $\gamma_\lambda(T)$ and $\gamma_H(T)$ are well understood (8). This result strongly suggests multiband superconductivity in the novel class of oxypnictide superconductors.

[1] Y. Kamihara, T. Watanabe, M. Hirano, and H. Hosono, J. Am. Chem. Soc. **130**, 3296 (2008).

[2] Z. Bukowski, S. Weyeneth, R. Puzniak, P. Moll, S. Katrych, N.D. Zhigadlo, J. Karpinski, H. Keller, and B. Batlogg, Phys. Rev. B **79**, 104521 (2009).

[3] S. Weyeneth, R. Puzniak, U. Mosele, N.D. Zhigadlo, S. Katrych, Z. Bukowski, J. Karpinski, S. Kohout, J. Roos, and H. Keller, J. Supercond. Nov. Magn. **22**, 325 (2009).

[4] S. Weyeneth, R. Puzniak, N.D. Zhigadlo, S. Katrych, Z. Bukowski, J. Karpinski, and H. Keller, J. Supercond. Nov. Magn. **22**, 347 (2009).

[5] N.D. Zhigadlo, S. Katrych, Z. Bukowski, S. Weyeneth, R. Puzniak, and J. Karpinski, J. Phys.: Condens. Matter **20**, 342202 (2008).

[6] V.G. Kogan, Phys. Rev. B **24**, 1572 (1981) and V.G. Kogan, Phys. Rev. Lett. **89**, 237005 (2002).

[7] J. Jaroszynski, F. Hunte, L. Balicas, Y.-J. Jo, I. Raicevic, A. Gurevich, D.C. Larbalestier, F.F. Balakirev, L. Fang, P. Cheng, Y. Jia, and H.-H. Wen, Phys. Rev. B **78**, 174523 (2008).

[8] M. Angst, R. Puzniak, A. Wisniewski, J. Jun, S.M. Kazakov, J. Karpinski, J. Roos, and H. Keller, Phys. Rev. Lett. **88**, 167004 (2002).

10.3 NMR investigations of orbital current effects in YBCO compounds

The possible existence and role of a hidden order parameter in the phase diagram of high-T_c superconductors are highly debated issues not only in cuprates but in high-T_c physics in general. Among the concepts of broken symmetry, the d-density wave (DDW) order (1) and the circulating-current (CC) picture (2) are the most prominent proposals. The characteristic of these models are currents, which are believed to flow in the CuO_2 planes of cuprate superconductors.

Besides photoemission evidence for dichroism (3), reports on polarized neutron scattering data claim consistency with such an ordered phase ($e.g.$ (4; 5)). However, the experimental situation remains controversial and it is highly desirable to use a more local probe, like nuclear magnetic resonance (NMR), to search for such orbital currents (OC's). For NMR, the relevant feature of OC formation is the resulting internal magnetic field distribution. For symmetry reasons, additional OC fields at the Y site in YBCO compounds point either along or perpendicular to the crystalline c axis for any of the proposed current patterns. Such current patterns are expected to form when the material enters the so-called pseudogap phase. With this phase a peculiar partial gap at the Fermi surface is associated, which still lacks a satisfying microscopic description. It is generally agreed, that a detailed understanding of the pseudogap phase is essential to solve the mystery of high-temperature superconductivity.

We completed our ^{89}Y NMR investigation of oriented powder samples of $Y_2Ba_4Cu_7O_{15-\delta}$ (Y247) to search for OC effects. Y247 exhibits a doping difference of Y neighboring CuO_2 planes which prevents a possible complete cancellation of fields due to OC circulating in adjacent planes. We found no clear evidence for the appearance of an OC phase in this specific compound (6). Nevertheless, we provide limits for static magnetic fields and fluctuating field amplitudes, which constitute meaningful constraints to theoretical models.

Typical NMR spectra are displayed in Figs. 10.5 a, b. In the Y247 compound the Knight shift drops significantly as one lowers the temperature below $200\,\mathrm{K}$, which is evidence for the opening of a pseudogap (Fig. 10.5 c).

To check for static magnetic fields, showing up at the Y site when entering the pseudogap phase, the temperature dependence of the leading-edge line width of the NMR absorption line was determined (Fig. 10.5 d). Additional static magnetic fields influence the NMR line only when pointing along the externally applied field. Conservatively, the total observed broadening in the investigated temperature range was taken to deduce an upper limit for a static OC effect, although both field orientations show the same broadening within measurement uncertainties. From our experiments we find a limit of $0.15\,\mathrm{mT}$ for an additionally in the pseudogap phase appearing static magnetic field at the Y site in Y247.

For the spin-lattice relaxation process only fields fluctuating perpendicular to the quantization axis are relevant. Hence, the occurrence of fluctuating OC must alter the ratio between the spin-lattice relaxation rate measured for the external field directed along ($1/T_1^{\parallel}$) and perpendicularly ($1/T_1^{\perp}$) to the c axis. The temperature dependence of the spin-lattice relaxation rate ratio was mea-

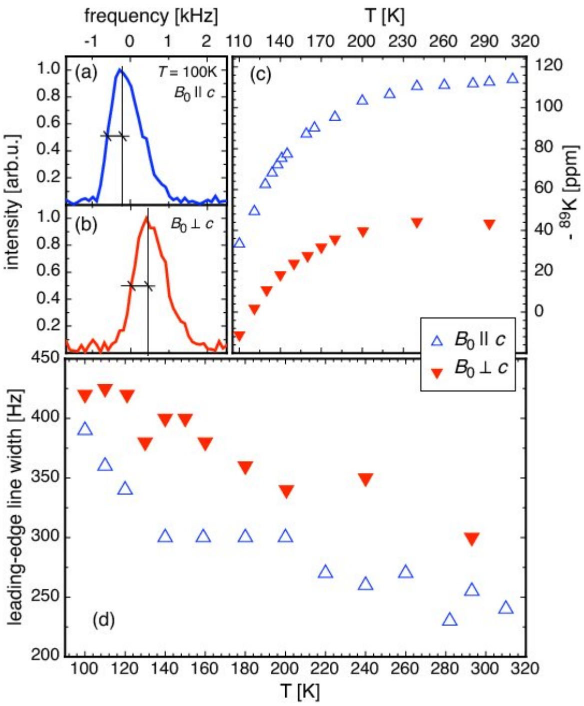

Figure 10.5: ^{89}Y NMR data of c-axis aligned powder measured in a $9\,\mathrm{T}$ field orientated parallel (‖) or perpendicular (⊥) to c. (a),(b): typical absorption lines at $100\,\mathrm{K}$ for both field orientations; (c): temperature dependent magnetic shift; (d): temperature dependent leading-edge line width at half height.

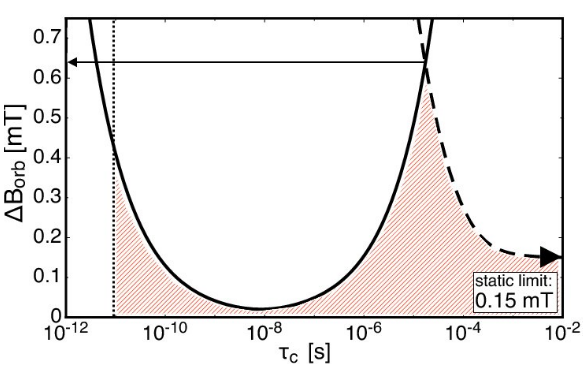

Figure 10.6: Dependence of the possible OC field amplitude ΔB_{orb} on the OC correlation time τ_c from ^{89}Y nuclear spin-lattice relaxation measurements in Y247 at $100\,\mathrm{K}$ (solid line, see text). Lower limit of τ_c from neutron (dotted) and upper limit of τ_c from line width measurements (dashed line) are shown. The maximum static field $\lesssim 0.15\,\mathrm{mT}$ is included. The shaded area represents all ΔB_{orb} consistent with measurements.

sured in the normal conducting state up to room temperature, covering the pseudogap regime. Within measurement error no change of this ratio was observed. Using a simple relaxation model the maximum field amplitude ΔB_{orb} consistent with measurement uncertainties was determined in dependence of the correlation time τ_c of fluctuating OC fields (6) (solid line in Fig. 10.6).

To limit τ_c towards the slow fluctuation regime, we included in our line-width analysis motional narrowing behavior (dashed line in Fig. 10.6). For the cutoff in the fast fluctuation regime we used results of reports on neutron scattering (4), where it was stated that the anomalous magnetism observed and related to OC is static on the neutron time scale. From Fig. 10.6 it is evident that a fluctuating magnetic field, which may appear at the Y site in the pseudogap phase of Y247 cannot exceed $0.7\,\mathrm{mT}$.

[1] S. Chakravarty, R.B. Laughlin, D. K. Morr, and Ch. Nayak, Phys. Rev. B **63**, 094503 (2001).

[2] C.M. Varma, Phys. Rev. B **73**, 155113 (2006).

[3] A. Kaminski, S. Rosenkranz, H.M. Fretwell, J.C. Campuzano, Z. Li, H. Raffy, W.G. Cullen, H. You, C.G. Olson, C.M. Varma, and H. Höchst, Nature **416**, 610 (2002).

[4] B. Fauque, Y. Sidis, V. Hinkov, S. Pailhes, C.T. Lin, X. Chaud, and P. Bourges, Phys. Rev. Lett. **96**, 197001 (2006).

[5] Y. Li, V. Baledent, N. Barisic, Y. Cho, B. Fauque, Y. Sidis, G. Yu, X. Zhao, P. Bourges, and M. Greven, Nature **455**, 372 (2008).

[6] S. Strässle, J. Roos, M. Mali, and H. Keller, Phys. Rev. Lett. **101**, 237001 (2008).

11 Phase transitions and superconducting photon detectors

O. Bossen, K. Inderbitzin, M. Reibelt, R. Dell'Amore, H. Bartolf, S. Siegrist, L. Gómez, A. Engel and A. Schilling

in collaboration with: Paul Scherrer Institute, University of Bern (K. Krämer), EPF Lausanne (H. Berger), Bhaba Atomic Research Center (G. Ravikumar), Forschungszentrum Karlsruhe (Th. Wolf, H. Küpfer), Tohoku University (N. Toyota), Universität Karlsruhe (K. Il'in), ETH Zürich (J. Karpinksi), Deutsches Zentrum für Luft- und Raumfahrt (H.-W. Hübers), University of Wellington (B. Ruck), Istituto Nazionale di Ricerca Metrologica I.N.RI.M Torino (C. Portesi), FIRST Lab ETH Zürich.

11.1 Physics of superconducting thin-film nanostructures and fast single-photon detectors

Single-photon detectors made from superconducting nanowires are representing a promising new technology: they are extremely fast and have a feasible detection efficiency. These characteristics make them detectors of first choice for a number of quantum correlation experiments or the emerging field of quantum encryption.

The properties of superconducting nanowire single-photon detectors (SNPD) crucially depend on the quality of the unstructured NbN film and the structuring process itself. We have further optimized our mix&match photo- and e-beam lithography process (1) and are now able to produce state-of-the-art single-photon detectors. Starting from a 5 nm thick NbN film (2) with a $T_c \approx 14$ K we have prepared several detectors with different strip widths and filling factors. In Fig. 11.1 a scanning electron microscope (SEM) picture is shown that depicts part of a meander structure with a strip width of only ~ 50 nm.

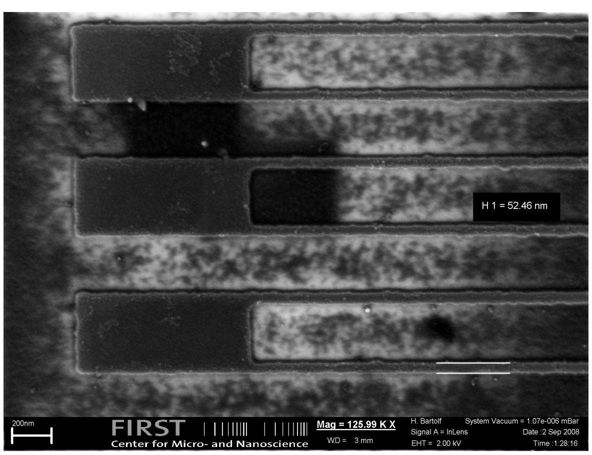

Figure 11.1:
SEM picture of a meander with approximately 50 nm strip width. The filling factor is around 15%.

For all the structures we have measured resistances as a function of temperature and magnetic field from which we could determine normal-state and superconducting properties. This is important to draw any conclusions about the detection mechanism. After the structuring the critical temperatures had dropped slightly to about 12.5 K, but the transitions were still smooth and relatively sharp, indicating very homogeneous meanders. The optical measurements were performed in a ^{4}He-bath cryostat, with the detectors cooled to ≈ 5.5 K. The detectors were biased with a custom-built, battery-powered constant voltage source and shielded from electro-magnetic interferences as much as possible. The continuous spectrum from the light source was passed through a prism monochromator and directed onto the meander through the optical access of the cryostat.

Three of the detectors were characterized in detail. They had different strip widths w and line spacings s, which should be reflected in

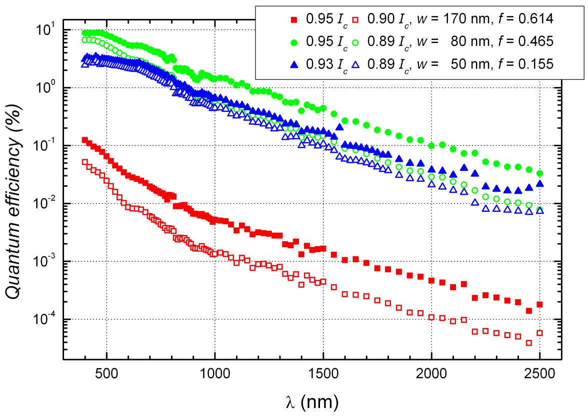

Figure 11.2: Quantum efficiency of three meanders with different strip widths as functions of the incident photon wavelength. Strip widths w and filling factors f are given in the caption.

their detection efficiencies and dark count rates. As an example we show in Fig. 11.2 the quantum efficiency as a function of incident light wavelength for fixed bias currents. The quantum efficiency is defined as the percentage of detected photons from the total flux of photons hitting the meander area per unit time. The data qualitatively fulfil our expectation that narrower meander lines improve the quantum efficiency at longer wavelengths, scaled with the filling factor $f \approx w/(w+s)$. The best achieved quantum efficiency of about 9% is in line with comparable state-of-the-art detectors (see, e.g., Ref. (3)) and further indicates the good homogeneity of the structures. The meander with a strip width of 50 nm reaches a quantum efficiency of roughly 3% (despite having a filling factor of only 0.155), and is one of the world-wide narrowest detectors produced so far.

[1] H. Bartolf, A. Engel, L. Gómez, and A. Schilling, Raith application note, Physics Institute of the University of Zurich, Switzerland (2008).

[2] K. Il'in et al., J. Low Temp. Phys., **151**, (2008) 585.

[3] C. Zinoni et al., Appl. Phys. Lett., **91**, (2007) 031106.

11.2 Search for melting of the flux line lattice in Nb_3Sn and V_3Si

Thermodynamic manifestations for the occurrence of a first order phase transition (FOT) of the vortex system in the mixed state of type II superconductors are well documented for the high-temperature superconductors $YBa_2Cu_3O_7$ and $Bi_2Sr_2CaCu_2O_8$, where it has been interpreted as a melting-like transition of the vortex lattice. Based on general arguments, such a first-order phase transition ought to be seen not only in high-T_c but also in conventional low-T_c superconductors, although it is expected to occur much closer to the upper-critical field H_{c2} (1) – (3).

There are indeed some experimental indications for the occurrence of such a transition very near $H_{c2}(T)$ of certain low-T_c superconductors (2) – (6). Any well developed, sharp first-order like peaks in the specific heat that are comparable to those observed in $YBa_2Cu_3O_7$ are absent in the published data, although very recently Lortz *et al.* interpreted their thermodynamic data on Nb_3Sn in terms of a FLL melting transition (5; 7).

It has been shown that a small ac magnetic field can help the vortices to reach equilibrium in the presence of flux pinning (8; 9). According to theoretical studies on equilibration processes with the help of a small ac field (9), the shaking frequency f should not play any role, but the shaking-field amplitude h_{ac} should be sufficiently large because it is related to the critical sheet current J_c (the current density integrated over the thickness d of the sample) and should fulfill the relation $h_{ac} > J_c/2$. We used an improved version of a low-temperature differential-thermal analysis (DTA) method (10; 11) in combination with an ac shaking magnetic field to measure the specific-heat of Nb_3Sn and V_3Si, and we compared the results with corresponding ac susceptibility and dc magnetization data.

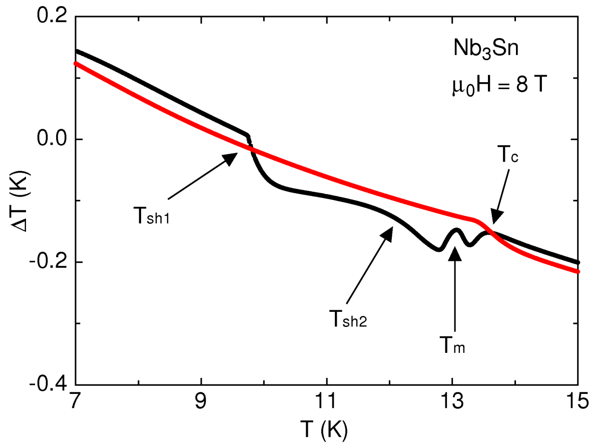

Figure 11.3: Temperature difference ΔT between the two thermometers of our DTA setup for the Nb_3Sn sample in $\mu_0 H = 8$ T. Red curve: Data without ac shaking field. Black curve: Data with an applied ac shaking field ($f = 5$ Hz and $h_{ac} = 0.5$ mT) oriented perpendicular to the main dc field.

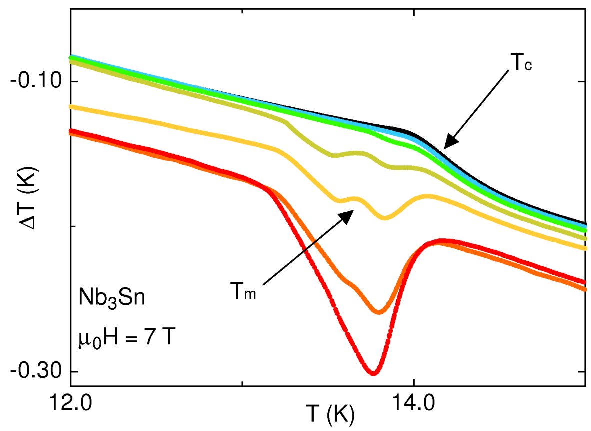

Figure 11.4: DTA-temperature difference for Nb_3Sn in $\mu_0 H = 7$ T and constant frequency $f = 5$ Hz for different shaking field amplitudes h_{ac}, varying form 0 up to ≈ 0.7 mT.

Figure 11.3 shows representative data measured in $\mu_0 H = 8$ T on the same Nb_3Sn crystal as used by Lortz *et al.* in previous studies (5; 7). The figure shows the temperature difference ΔT between the two thermometers of our DTA setup which is related to the specific heat. The red curve shows corresponding data with no ac shaking field, while the black curve shows a measurement with an ac shaking magnetic field oriented perpendicular to the main dc field ($f = 5$ Hz, $h_{ac} \approx 0.5$ mT). The data with vortex shaking exhibit 3 main new features as compared to the data without shaking. At T_{sh1}, a self heating process sets in that is likely caused by vortex motion, driven by the ac shaking field which is strong enough to overcome the pinning of the vortices at this temperature. At T_{sh2} a second, additional self heating process seems to set in. Within this second self heating region (at T_m), a bump-like feature occurs for some shaking parameters, superimposed to the self-heating effect. This bump-like feature is reminiscent to a signature of a first order phase transition and may indicate the melting of the vortex lattice, although the transition is rather broad and the latent heat associated with the transition is unusually high. Fig. 11.4 shows the evolution of this self-heating region for different shaking amplitudes. As expected, the self heating increases with increasing shaking amplitude. Interestingly, the bump-like feature at T_m first increases with increasing shaking amplitude, but then decreases for higher amplitudes h_{ac}.

In order to clarify the origin of the observed features, we investigated the same Nb_3Sn crystal also by measuring its ac susceptibility $\chi(T)$. To compare these data with our DTA measurements we chose a comparable frequency ($f = 10$ Hz) and shaking amplitudes. Fig. 11.5 shows one of these measurements for $h_{ac} = 1$ mT (down and up directions are drawn in black and red, respectively). Besides a feature that is usually interpreted as the manifestation of the "peak effect" in the literature (T_p in Fig. 11.5), a shoulder-like feature appears at a $T_m < T_p$, above which the observed hysteresis vanishes as one would expect if a vortex lattice melting transition occurs at T_m.

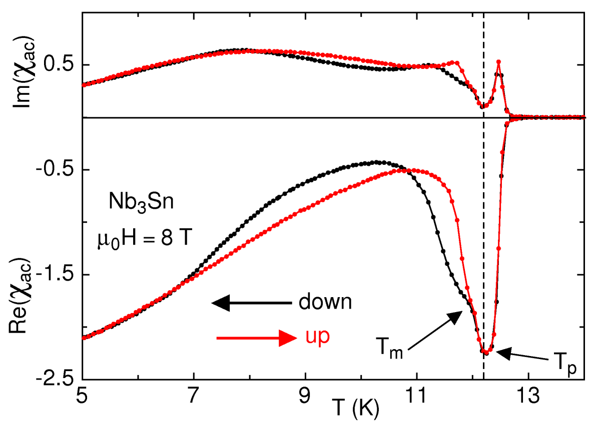

Figure 11.5: Real and imaginary part of the ac susceptibility for Nb_3Sn in $\mu_0 H = 8$ T with $f = 10$ Hz and $h_{ac} = 1$ mT.

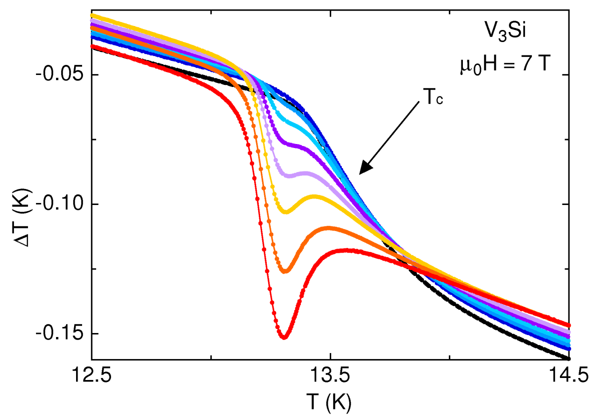

Figure 11.6: DTA-temperature difference for a V_3Si sample in $\mu_0 H = 7$ T and constant frequency $f = 5$ Hz for different shaking field amplitudes h_{ac}, varying form 0 up to ≈ 0.7 mT.

We performed similar DTA measurements on a V_3Si crystal that shares the same cubic "β-tungsten (A-15)" structure with Nb_3Sn. Fig. 11.6 shows a series of DTA measurements at fixed magnetic field $\mu_0 H = 7$ T, fixed ac shaking field frequency $f = 5$ Hz and different amplitudes h_{ac}. The ac shaking field causes again a self heating effect, but with no bump-like feature superimposed as observed in Nb_3Sn. Corresponding magnetic-susceptibility measurements on V_3Si (data not shown) also do not show any related shoulder-like feature below T_p either. We tentatively explain this different behavior of V_3Si with the stronger vortex pinning than in Nb_3Sn that manifests itself in a larger magnetic peak effect, thereby suppressing the melting transition at T_m.

[1] G. P. Mikitik and E. H. Brandt, Phys. Rev. B, **64**, (2001) 184514.

[2] V. A. Marchenko and A. V. Nikulov, JETP Letters, **34**, (1981) 17.

[3] E. Brézin, D. R. Nelson, and A. Thiaville, Phys. Rev. B, **31**, (1985) 7124.

[4] G. Ravikumar and H. Küpfer, Phys. Rev. B, **72**, (2005) 144530.

[5] R. Lortz et al., Phys. Rev. B, **75**, (2007) 094503.

[6] A. Bianchi et al., Phys. Rev. Lett., **91**, (2003) 187004.

[7] R. Lortz et al., Phys. Rev. B, **74**, (2006) 104502.

[8] M. Willemin et al., Phys. Rev. B, **58**, (1998) R5940.

[9] E. H. Brandt and G. P. Mikitik, Phys. Rev. Lett, **89**, (2002) 027002.

[10] A. Schilling and M. Reibelt, Rev. Sci. Instrum., **78**, (2007) 033904.

[11] M. Reibelt et al., Physica C, **468**, (2008) 2254.

11.3 Intrinsic instability of Bose-Einstein condensates in magnetic insulators

Quantum spin systems in solids have become a subject of intense research, both theoretically and experimentally. A number of such systems show magnetic-field induced phase transitions at zero temperature that have been interpreted as a Bose-Einstein condensation (BEC) of magnetic bosonic quasiparticles. In axially symmetric dimerized spin-1/2 systems, one expects a condensation of triplet bosonic excitations ("triplons") above a certain critical field H_c where the energy difference between the ground-state singlet and the lowest excited triplet states vanishes due to the Zeeman splitting. Despite the large number of experimental papers on the occurrence of BEC in magnetic insulators there is no direct proof for the existence of such a condensate, i.e., the demonstration of macroscopic phase coherence or even superfluidity of corresponding spin currents. To the best of our knowledge, the only attempt to find a direct experimental evidence for such a macroscopic quantum state in $TlCuCl_3$ has been undertaken in our group but has not shown any sign for such a coherent quantum state in $\mu_0 H = 9$ T on a time scale larger than 0.5 μs (see previous annual reports). The notorious lack of experimental evidence supporting the existence of a long-lived phase coherent condensate in any real material is, from an experimental point of view, highly unsatisfactory.

To further analyze this problem we have used a standard functional method to describe dilute Bose gases in the classical limit at $T = 0$ that provides an extremal condition for the potential energy u of the condensate per dimer in such systems (1). Including a perturbation term $\gamma(\Psi\Psi + \Psi^*\Psi^*)$ with $\gamma > 0$ that explicitly violates axial symmetry (2; 3) we obtain the condition

$$\begin{aligned} u(\Psi) &= -\mu\Psi^*\Psi + \gamma\left(\Psi\Psi + \Psi^*\Psi^*\right) + \frac{\nu_0}{2}\left(\Psi^*\Psi\right)^2 \\ &= min.\,, \end{aligned}$$

where $\Psi(r,t)$ is the complex scalar field describing the BEC condensate, $\mu(H) = g\mu_B\mu_0(H - H_c)$ is the chemical potential with the Landé g-factor, and ν_0 is the two-particle interaction potential (4).

An important consequence of a violated axial symmetry is that the potential energy at H_c for the optimum $\Psi_0(r) = |\Psi_0|\, e^{i\phi}$ is smaller for $\gamma > 0$ (by $\Delta u = 2\gamma^2/\nu_0$) than for an axially symmetric system with $\gamma = 0$ (see Figs. 11.7 and 11.8), and the corresponding phase $\phi = \pm\pi/2$ is fixed. This means that an originally axially

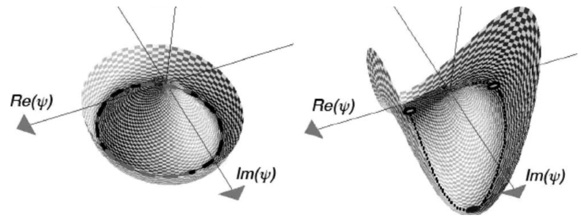

Figure 11.7: (a) Potential energy $u(\Psi)$ for axial symmetry ($\gamma = 0$). The minima are located on a circle with arbitrary phase ϕ (dashed line). (b) $u(\Psi)$ for violated axial symmetry ($\gamma > 0$). The potential energy at the isolated minima (filled circles) is lower than that of an axially symmetric system.

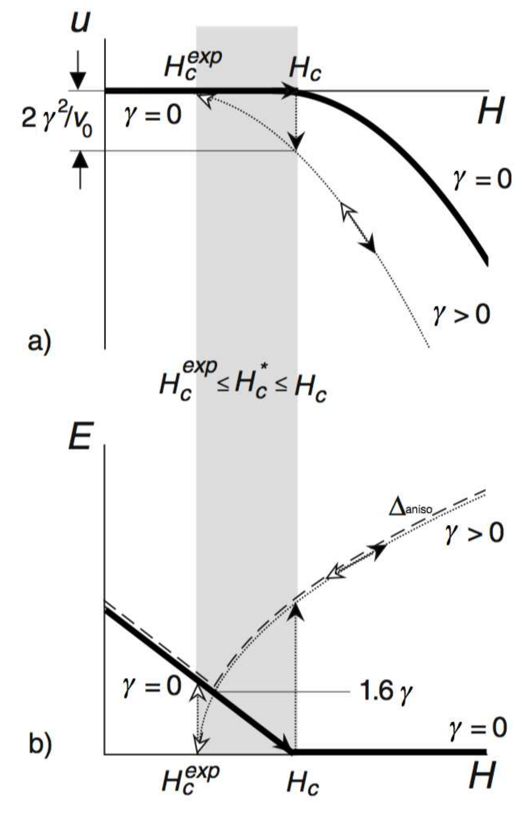

Figure 11.8: (a) Potential energy and (b) energy-level scheme of the lowest triplon branch of an axially symmetric system ($\gamma = 0$, solid lines) and of a system that shows a spontaneous violation of axial symmetry ($\gamma > 0$) at a field H_c^* with $H_c^* \leq H_c$ (dashed line). Arrows indicate the maximum possible hysteresis for increasing and decreasing magnetic field, respectively (shaded area)

symmetric system ($\gamma = 0$) tends to spontaneously distort ($\gamma > 0$) as soon as the BEC is formed at H_c as long as the total energy, including the crystal-lattice contribution, is lowered along with this distortion. As the potential energy may jump discontinuously at a $H_c^* < H_c$ (see Fig. 11.8a), the transition is probably of weakly-first order. Moreover, the resulting state above H_c^* cannot be regarded as a superfluid because the spin-supercurrent velocity $v_s = \hbar m^* \nabla \phi$ is strictly zero.

Our results easily explain why no experiment has ever detected any superfluid-like response in any magnetic insulator. It also accounts for numerous observations of first-order like effects at the critical fields of $TlCuCl_3$ (5; 6) and of the spin-1 system $NiCl_2$-4SC$(NH_2)_2$ (7). These arguments are so general that they should be applicable to all insulating spin systems that are supposed to show a Bose-Einstein condensation of magnetic bosonic quasiparticles, and we expect that all magnetic BEC systems in insulating spin systems are intrinsically unstable toward a spontaneous anisotropic distortion perpendicular to the external magnetic field.

[1] J. O. Andresen, Rev. Mod. Phys., **76**, (2004) 599.

[2] I. Affleck, Phys. Rev. B, **43**, (1991) 3215.

[3] J. Sirker, A. Weisse and O. P. Sushkov, J. Phys. Soc. Jpn., **74**, (2005) 129.

[4] R. DellŠAmore, A. Schilling and K. Krämer, Phys. Rev. B, **79**, (2009) 014438.

[5] O. Vyaselev et al., Phys. Rev. Lett., **92**, (2004) 207202.

[6] E. Ya. Sherman et al., Phys. Rev. Lett., **91**, (2003) 057201.

[7] V. S. Zapf et al., Phys. Rev. Lett., **96** (2006) 077204.

12 Surface Physics

T. Greber, M. Hengsberger, J. H. Dil, H. Yanagisawa, H. Ma, C. Galli-Marxer, C. Hengsberger, M. Morscher, T. Brugger, F. Meier, D. Leuenberger, S. Roth, J. Schmidlin, M. Thomann, D. Böni, P. Donà, M. Hausherr, M. Klöckner, J. Osterwalder

In the surface physics group model systems of well defined surfaces and interfaces are systematically studied in order to address fundamental issues that are potentially relevant for nanoscience and nanotechnology. Our laboratory is well equipped for the preparation and characterization of clean surfaces, ultrathin metal films, molecular monolayers and covalently bonded single layers like hexagonal boron nitride or graphene, all under ultrahigh vacuum (UHV) conditions. Techniques available to us include x-ray photoelectron spectroscopy (XPS) and diffraction (XPD), angle-resolved photoemission spectroscopy (ARPES), two-photon photoemission (2PPE) using femtosecond laser pulses, low-energy electron diffraction (LEED) and variable-temperature scanning tunneling microscopy (STM). At the nearby Swiss Light Source (SLS) we operate two more photoemission spectrometers, one for spin- and angle-resolved photoemission spectroscopy (SARPES) and one for photoelectron diffraction and holography. A growing network of national and international collaborations expands this set of techniques and provides us also with the necessary theoretical support.

The research carried out during the report period can be grouped into four topics:

- **Monolayer films of hexagonal boron nitride and graphene on metal surfaces**
  The boron nitride nanomesh is a one atom thick layer of hexagonal boron nitride (h-BN) on Rh(111) surfaces, which we discovered a few years ago (1). It exhibits a very regular hexagonal corrugation pattern with 2 nm wide "holes", i.e. regions where the layer is more strongly bonded to the metal surface, and a periodicity of 3.2 nm, giving the surface a mesh-like appearance in STM images. We have continued the studies of Co cluster formation on the nanomesh by adsorbing Co carbonyls. Preliminary results indicate that these molecules strip off their carbonyl groups completely and, when deposited at low temperatures (50 K), tend to form rather monodisperse ultrasmall clusters inside the holes. In the context of a new collaborative SNF SINERGIA project (since 1 October 2008), where the nanomesh template functionality in solutions is explored, our main activity is the study of the adsorption of water molecules on the nanomesh. Low-temperature STM images show the formation of monodisperse two-dimensional ice crystals. In the course or two Master projects (J. Schmidlin and Mario Thomann), our room temperature STM was equipped with a detector for photons excited locally by the tunneling current from the tip. Recently a clear contrast with the nanomesh periodicity could be observed on a h-BN covered Rh(111) surface. Finally, we have extended our activities in the field of sp^2 bonded monolayer networks to the closely related systems of graphene on transition metal surfaces. A direct comparison of the properties of graphene and boron nitride monolayers on the Ru(0001) surface are presented in Sec. 12.1.

- **Ultrafast processes at surfaces**
  Using femtosecond laser pulses from an amplified laser system, time-resolved photoemission can be used to observe fast electron dynamics at surfaces. Two major projects have been pursued and successfully finished last year. Image poten-

tial states, which exist in front of metal surfaces, may be spin-split due to the exchange-split bandstructure of the metal. Such a state has been identified in front of the h-BN/Ni(111)-surface investigated here. It can be exited resonantly using the second harmonic from a Ti:Sa laser system (2). The energy position of the image potential state is sensitive to the magnetic phase and can be used as an ultrafast thermometer for the phenomenological spin temperature in the surface region of the metal. By means of an intense infrared pump pulse, energy is pumped into the system, leading to the reduction of the magnetic moment within a few hundred femtoseconds (3). As a consequence of the enhanced electron temperature, the transient position of the image potential state shifts towards higher energies within about 200 fs after the pump pulse. This shift can be related to spin disorder resulting in an effective spin temperature close to the Curie temperature of bulk nickel.

The second project concerned time- and angle-resolved photoelectron spectroscopy from a self-assembled monolayer of tetramantane molecules absorbed onto Ag(111) and Au(111) surfaces. Tetramantane is the first member of the class of higher diamondoids, which are small nanometer-sized molecules of carbon atoms in a diamond structure (4). These monolayer systems were previously shown, using synchrotron radiation, to have a negative electron affinity (5). They represent thus very efficient electron emitters. Using a widely tunable parametric amplifier as light source, a threshold behavior was found for the excitation yield. This threshold could be related to the substrate bandstructure. Moreover, the experiments allowed the angular emission cone to be measured and the value of the negative electron affinity to be estimated. From these and further time-resolved measurements we conclude that the initial excitation takes place in the substrate. Furthermore, the retention time of the electrons in the diamondoid orbital before emission could be estimated to be below 2 fs, indicating a very efficient charge transfer from the substrate to this orbital and subsequent emission into vacuum.

In parallel to these efforts, photon-assisted field emission from sharp W-tips was studied by using infrared pulses from the laser oscillator. In order to characterize the tips and the electron-emission intensity patterns, a position-sensitive, microchannelplate amplified electron detector was used. For this purpose new read-out electronics and data acquisition routines were implemented within a Bachelor project (P. Donà). The emission patterns show a very distinct asymmetry, which is related to the propagation direction of the light field. These patterns are currently being simulated by using finite-element methods.

- **Spin-resolved photoemission and momentum mapping**

Our spin-resolved photoemission chamber at the SLS (COPHEE, the complete photoemission experiment) has been upgraded with new high voltage electronics for the Mott detectors, which has resulted in a further increase of the detection efficiency and in the operation stability. The combination of the unique capabilities of COPHEE with the two step analysis routine we developed last year (6) has resulted in a variety of new and unexpected results. We have, for example, been able to measure a spin splitting of Pb quantum well states which is not accessible with spin integrated ARPES (see Sec. 12.2). Further have we been able to provide the first direct experimental observation of the quantum spin Hall phase on the surface of a BiSb alloy (7). In order to determine the influence of reduced dimensionality on the spin structure of surfaces, we have performed SARPES measurements on the

Bi(114) vicinal surface. The Fermi surface of this system primarily consists of a pair of one-dimensional spin split bands (8). Because all electrons at the surface with positive momentum have spin up and all electrons with negative momentum spin down, Bi(114) can be considered as the parent compound of a one-dimensional quantum spin Hall system.

- **Further instrumental developments**
  For molecules adsorbed on ferromagnetic surfaces the spin-dependent coupling of molecular orbitals to states of the underlying substrate can be studied. In order to exploit the versatile preparation and characterization environment of our photoelectron spectrometer chamber, we have engaged in a development project for a simplified type of spin detector that is compatible with the existing hemispherical electron analyzer. In this new type of Mott detector, backscattered high-energy electrons are measured within scintillators. The light pulses are extracted by glass rods out of the UHV. A first prototype has been built and is currently undergoing tests.

  For more efficient studies of ultrafast phenomena on surfaces by means of time-resolved photoemission, a new electron display analyzer has been implemented, which allows the whole angular distribution of photoelectrons at a given energy to be recorded in one shot (9). The commissioning included the setup of a new vacuum system and building a new sample manipulator. Within a new Bachelor project (M. Hausherr) the visible light pulses of the second harmonic of the Ti:Sa laser are again frequency-doubled to about 6 eV in a new β-barium-borate crystal and coupled into the vacuum system by using a SrF_2-viewport, which is transparent for uv-radiation.

In the following, two highlights of last year's research are presented in more detail.

12.1 Comparison of single-layer graphene and hexagonal boron nitride on Ru(0001)

in collaboration with: S.Günther and J. Wintterlin, Department Chemie, Ludwig-Maximilian Universität, D-81377 München, Germany; B. Wang and M.-L. Bocquet, Laboratoire de Chimie, Université de Lyon, Ecole Normale Suprieure de Lyon, CNRS, F-69007 Lyon, France; D. Martoccia and P. R. Willmott, Swiss Light Source, Paul Scherrer Institut, CH-5232 Villigen, Switzerland.

Graphene and hexagonal boron nitride (*h*-BN) are isoelectronic sp^2 hybrid-bonded networks that can be grown on transition metals (10). For the case of h-BN/Rh(111) the formation of a nanomesh with new functionalities has been reported (1; 11; 12). Grown on Ru(0001) h-BN (13) and graphene (g) (14) also form large supercells, with lattice constants of about 3 nm, that are caused by the lattice mismatch between the sp^2 network and the substrate. For g/Ru(0001) surface X-ray diffraction showed a surprisingly large (23x23) unit cell (referenced to the primitive Ru(0001) unit cell) containing four 3 nm subcells (15). The strong site dependence of the interaction to the substrate leads to a corrugation or rippling of the overlayers with a height difference between strongly bonded and weakly bonded regions of the sp^2 networks, which is in the order of 0.1 nm. Bonding occurs wherever nitrogen or carbon atoms sit on top of metal atoms (16; 17). For the graphene layer this condition can be met by either one of the two carbon atoms in the unit cell, while for h-BN there is only one nitrogen atom in the unit cell. The overall area of strongly bonded regions it therefore larger in the graphene case. This has the consequence that the h-BN nanomesh has isolated strongly bonded patches (holes) and graphene has connected, strongly bonded valleys and weakly bonded mounds with a diameter of about 2 nm (18). One layer is in fact

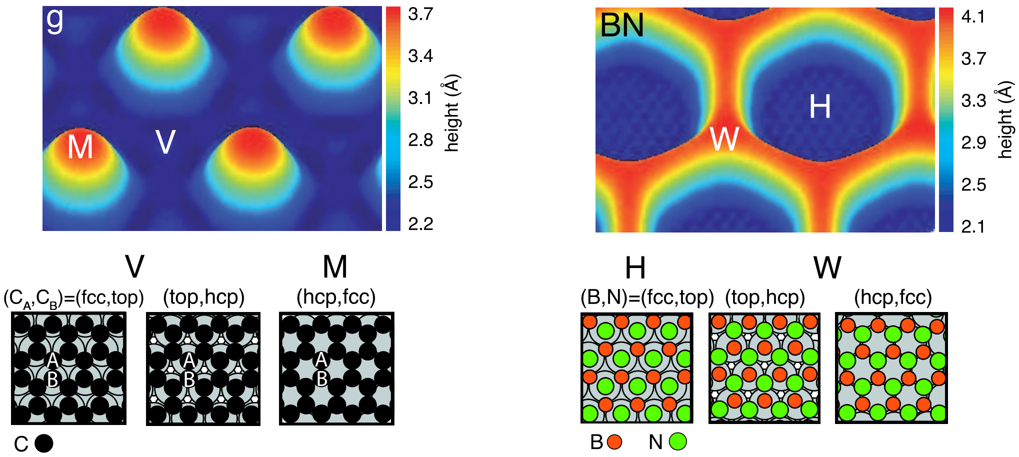

Figure 12.1: Views of the height modulated graphene (g) and h-BN on Ru(0001). M and V denote mounds (high) and valleys (low) of the graphene, H and W holes (low) and wires (high) of the h-BN. The six ball model panels illustrate the three different bonding regions (fcc, top), (top, hcp), and (hcp, fcc).

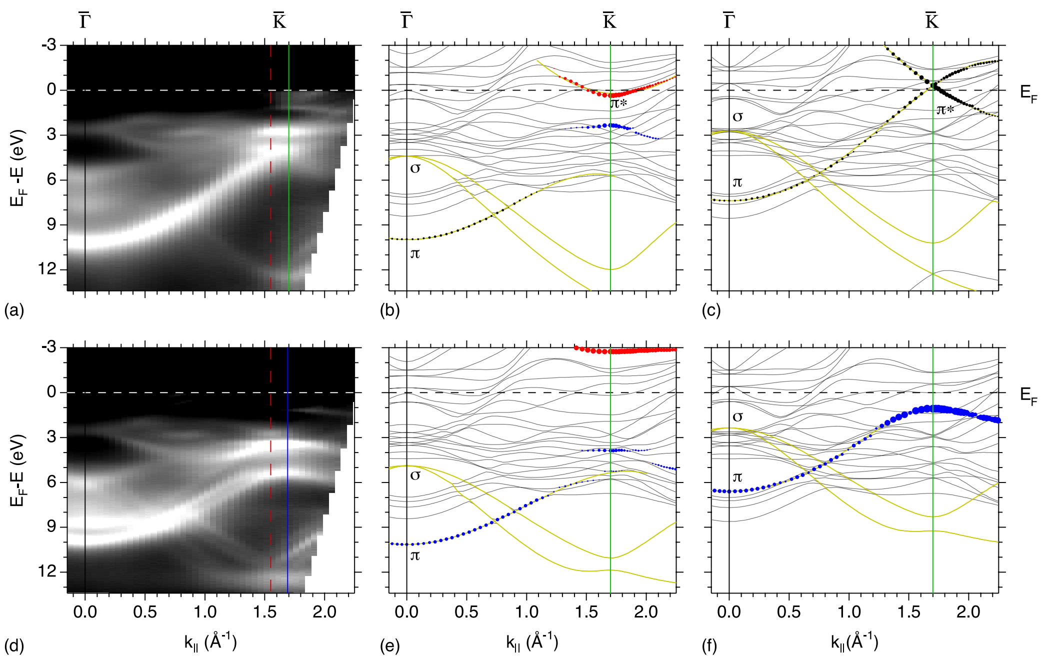

Figure 12.2: Band structures of graphene and h-BN nanomesh on Ru(0001) along $\overline{\Gamma K}$: (a) He II$_\alpha$ photoemission data of g/Ru(0001). (b) and (c) Density Functional Theory (DFT) results of g/Ru(0001) for the low ((C$_A$, C$_B$) (top, hcp)) and high ((C$_A$, C$_B$) (hcp, fcc)) regions, respectively (see Fig. 12.1). (d) He II$_\alpha$ photoemission of h-BN/Ru(0001). (e) and (f) DFT results of h-BN/Ru(0001) for the low ((B, N) (fcc, top)) and high ((B, N) (hcp, fcc)) regions. The vertical lines at and near $\overline{K}$ in (a) and (d) indicate the boundaries of the 1$\times$1 surface Brillouin zones for Ru (red dashed), h-BN (blue solid) and graphene (green solid). The sizes of the dots in the theoretical curves represent the p_z weight of specific adsorbate atoms in the bands, where blue describes atop atoms (C$_A$ in (b) and N in (e)) and red hollow site atoms (C$_B$ in (b) and B in (e)). Black dots in (c) depict the weight averaged over the two carbon atoms in the graphene unit cell. Thick yellow curves are guides for the eyes. From Ref. [18].

reminiscent of the casting mould of the other (see Fig. 12.1). Obviously this may cause similarities and differences in the electronic structure and functionality of the two systems.

The electronic structures along $\overline{\Gamma K}$ in the 1x1 surface Brillouin zones of h-BN/Ru(0001) and g/Ru(0001) show a large π-band gap at the $\overline{K}$ point. For graphene the carbon-substrate interaction causes this gap. It reflects the substrate induced symmetry breaking between the two carbon sublattices C_A and C_B of graphene. A charge transfer of 0.05 electrons per carbon atom to the graphene layer moves this gap fully into the occupied states (Fig. 12.2 a)), with electron pockets forming around the $\overline{K}$ points (18). For h-BN the sublattice symmetry breaking is intrinsic since the nitrogen and the boron network are not even identical in the free standing case - hence the large band gap. Most of these observations (Fig. 12.2 (a, d)) are reproduced by density functional theory (DFT, Fig. 12.2). The gaps and, for the graphene case, the charge transfer are nicely reproduced in calculations for the strongly bonded (low) regions (Fig. 12.2 (b, e)). In the h-BN case, the splitting of the σ and π bands resulting from the contribution of the weakly bonded (high) regions is also reproduced (Fig. 12.2 (f)), while the predicted closing of the gap on the mounds of graphene (Fig. 12.2 (c)) is not seen in our data.

12.2 Rashba-type spin-orbit splitting of quantum well states in ultrathin Pb films

in collaboration with: Luc Patthey, Swiss Light Source, PSI, Villigen, Switzerland and Gustav Bihlmayer, Institut für Festkörperforschung, Forschungszentrum Jülich.

When the thickness of a metal layer is smaller than the electron coherence length, quantum well states (QWS) may form in the layer. Within a simple model these are well described by standing electron waves between the metal-substrate and metal-vacuum interface. We have performed spin and angle resolved photoemission spectroscopy (SARPES) measurements on QWS in thin Pb films. It will be shown that the atomic and electronic structure of the metal-substrate interface provides the essential ingredient for the occurrence of Rashba type spin-orbit splitting of these quantum well states. This is a relativistic effect caused by the effective potential gradient that results from the breaking of the space inversion symmetry at surfaces or interfaces (19). In the reference frame of the electron this is equivalent to an in-plane magnetic field, and in a first approximation bands with opposite spin will be shifted in opposite momentum directions. The size of this band splitting depends on the atomic spin-orbit coupling strength and on the magnitude of the potential gradient, where a larger potential gradient results in a larger splitting.

The metal-vacuum interface and the metal-substrate interface are typically not identical for a thin metal layer, and consequently the space inversion symmetry is broken. Similarly to the situation for metal surface states this should result in the spin splitting of the quantum well states. However, up to now no splitting that can be explained by this mechanism has been observed. It has been shown previously that QWS may show a spin splitting due to hybridization with interface (20) or surface states (21), which either decays with layer thickness or is sensitive to contamination. Here we report the first observation of an intrinsic Rashba type spin-orbit splitting in metallic QWS by SARPES (22). An example of these results is shown in Fig. 12.3. The measured splitting of the Kramers pairs of approximately 15 meV is larger than what is observed in the classical Rashba systems, the two-dimensional electron gases in semiconductor heterostructures (23), but too small to be directly accessible by high resolution ARPES. The additional tag of spin polarization is needed to separate the

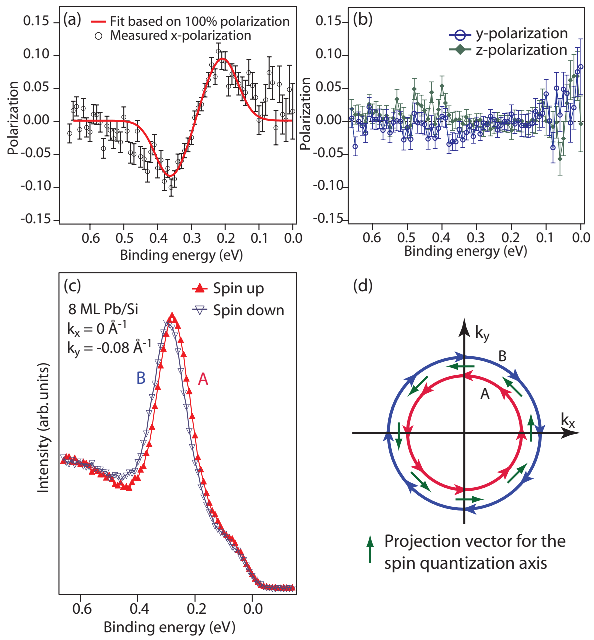

Figure 12.3: Spin and angle resolved photoemission data for an 8 ML thick Pb layer on Si(111)$\sqrt{3}\times\sqrt{3}$ ($R30°$). (a) Measured and modeled spin polarization in the x-direction of the sample. (b) Measured spin polarization along the y and z direction of the sample. (c) Spin resolved spectra obtained from the spin polarization in the x-direction. The splitting between the two peaks is 14 meV. (d) Schematic representation of a constant energy surface where the arrows of band A and B refer to the direction of the spin polarization axis (from Ref. [22]).

two split peaks. Furthermore we find a reversal of the spin orientation with respect to the Au(111) L-gap surface state (24) and no strong dependence on the Pb layer thickness.

The magnitude of the splitting, the spin polarization direction and the absence of a dependence on the layer thickness are explained by the net result of competing effects at both interfaces. This interpretation is corroborated by state-of-the-art density functional theory calculations where the substrate is included (22). This means that the spin-orbit interaction takes place throughout the whole layer, but the necessary asymmetry is induced by the two interfaces of the film. This opens up the possibility to manipulate the Rashba effect by interface engineering. This tunability in combination with the technologically interesting size of the band splitting and the fact that the system is formed on a semiconductor substrate, can provide a next step to the realisation of a spin field effect transistor as proposed by Datta and Das (25) and may benefit other fields of spintronics.

[1] M. Corso et al., Science **303**, 217 (2004).
[2] M. Muntwiler et al., Phys. Rev. B **75**, 075407 (2007).
[3] B. Koopmans et al., J. Magn. Magn. Mat. **286**, 271 (2005).
[4] J.E. Dahl, S.G. Liu, and R.M.K. Carlson, Science **299**, 96 (2003).
[5] W.L. Yang et al., Science **316**, 1460 (2007).
[6] F. Meier et al., Phys. Rev. B **77**, 165431 (2008).
[7] D. Hsieh et al., Science **323**, 919 (2009).
[8] J. W. Wells et al., Phys. Rev. Lett. **102**, 096802 (2009).
[9] T. Dütemeyer et al., Rev. Sci. Instr. **72**, 2638 (2001).
[10] C. Oshima and A. Nagashima, J. Phys.: Condens. Matter **9**, 1 (1997).
[11] S. Berner et al., Angew. Chem. Int. Ed. **46** 5115 (2007).
[12] H. J. Dil et al., Science **319** 1826 (2008).
[13] A. Goriachko et al., Langmuir **23**, 2928 (2007).
[14] S. Marchini, S. Günther and J. Wintterlin, Phys. Rev. B **76**, 075429 (2007).
[15] D. Martoccia et al., Phys. Rev. Lett. **101**, 126102 (2008).
[16] R. Laskowski, P. Blaha, T. Gallauner, and K. Schwarz, Phys. Rev. Lett. **98**, 106802 (2007).
[17] B Wang et al., Phys. Chem. Chem. Phys., **24**,3530 (2008).
[18] T. Brugger et al., Physical Review B, **79**, 045407 (2009).
[19] Y.A. Bychkov and E.I. Rashba, JETP Lett. **39**, 78 (1984).
[20] C. Koitzsch et al., Phys. Rev. Lett. **95**, 126401 (2005).
[21] K. He et al., Phys. Rev. Lett. **101**, 107604 (2008).
[22] J. H. Dil et al., Phys. Rev. Lett. **101**, 266802 (2008).
[23] J. Nitta et al., Phys. Rev. Lett. **78**, 1335 (1997).
[24] M. Hoesch et al., Phys. Rev. B **69**, 241401 (2004).
[25] S. Datta and B. Das, Appl. Phys. Lett. **56**, 665 (1990).

13 Physics of Biological Systems

Conrad Escher, Hans-Werner Fink, Matthias Germann, Heinz Gross (since January 2009), Tatiana Latychevskaia, Jean-Nicolas Longchamp, Elvira Steinwand.

in collaboration with:
Eugen Ermantraut, Clondiag Chip Technologies (Germany); Prof. John Miao, University of California at Los Angeles (USA); Prof. Dieter Pohl, University of Basel; Prof. Andre Geim, Manchester Centre for Mesoscience & Nanotechnology, University of Manchester, Dr. Ilona Müllerová, Institute of Scientific Instruments (Czech Republic), Dr. Petr Formanek, University of Dresden (Germany), Dr. Soichiro Tsujino (PSI, Switzerland).

The structural investigation of individual biological objects by employing coherent low energy electrons is the primary goal of our research. It involves holography with low energy electrons as well as coherent diffraction and is assisted by micro-structuring techniques using a focused gallium ion beam device.

Our current activities are divided in the following interconnected individual projects:

- **SIBMAR**
  Structural Information of Biological Molecules at Atomic Resolution is part of the EU "New Emerging Science and Technology" Programme. SIBMAR aims at high resolution structural information of individual biological molecules by employing coherent low energy electron waves. Partners from the Institute of Scientific Instruments Academy of Sciences of the Czech Republic in Brno, the Physics Department of the University of Manchester and the Physics-Institute of the University of Zurich are involved in SIBMAR. The overall idea is to apply holography with low energy electrons to investigate the structure of individual biological molecules. Major experimental challenges are to improve the interference resolution in electron holograms, establish methods for creating free standing thin films transparent for low energy electrons as well as appropriate techniques to present a single protein to the coherent electron wave front. Next to these experimental issues, a second, equally important aspect for achieving high resolution structural information is the reconstruction of the electron holograms. This is achieved by back-propagating the object wave information, recorded in the hologram plane, by employing a numerical algorithm to solve the integrals governing this coherent optics problem.

- **Electron and Ion Point Sources**
  We employ Field Ion Microscopy and related techniques for fabricating and using novel electron and ion point sources. Recently we have established collaboration with the PSI to characterize field emitter arrays produced by electron beam lithography and intended to be used as bright electron sources for the XFEL (X-Ray Free Electron Laser) project.

- **Fluorescent Microscopy**
  The aim of this project is to directly observe the dynamics of single DNA molecules in liquids by video fluorescent microscopy. In combination with molecular anchoring techniques, adopted from Clondiag, we address the energetics of a single DNA molecule. Appropriate DNA modifications for attaching fluorescent proteins to are designed by Clondiag Chip Technologies in Jena and shall serve us in our efforts to obtain structural information about proteins by electron holography.

- **Coherent Low-Energy Electron Diffraction Microscopy**
  This is a second approach, next to electron holography, of using a coherent electron wave front for structural biology at the single molecule level. It is in collaboration with John Miao from the University of California at Los Angeles and supported by the Swiss National Science Foundation and shall be described in some more detail below.

13.1 Summary

Most of the protein structural information data available today have been obtained from crystallography experiments by means of averaging over many molecules assembled into a crystal. While this has led to an impressive data base, a strong desire to gain structural data from just a single molecule is emerging for several reasons. Most of the biological relevant molecules exhibit different conformations; thus averaging over many of them smears out their fine structure. This need for averaging also limits cryo-TEM studies to particularly rigid species, like viruses (1) and radiation damage limits the obtainable resolution to $\approx 10\AA$ (2) The second motivation for the desire to image just one individual molecule is associated with the wish to drop the need to force proteins to assemble into crystals. If just one single protein could be analyzed in sufficient detail, the important class of membrane proteins that have a tendency to not crystallize would finally be accessible. Due to the strong inelastic scattering of X-rays and high energy electrons as employed in conventional electron microscopes, there is little hope for obtaining structural information from just one single molecule. The worldwide developments of X-ray Free Electron Lasers [6] did rise hope to circumvent the undesirable ratio between elastic and inelastic scattering by employing extremely short and bright pulses which do not leave enough time for the molecule to decompose owing to radiation damage.

The objective of this project is to derive atomic structure information from experiments carried out on just one individual molecule subject to the interaction with a coherent low energy electron wave. Evidence that there is no respectively undetectable radiation damage on a single molecule, combined with the fact that the de Broglie wave length of the low energy electron wave is in the $1\AA$ regime provide the potential for atomic resolution imaging of a single biomolecule. It appears that electrons with kinetic energies below 200 eV are the only known radiation today where elastic scattering dominates and radiation damage is minimal respectively not present at all (3). This in turn allows the acquisition of a large enough data-set from just one individual molecule without damaging it. This will be done by recording oversampled coherent low energy electron diffraction patterns of individual biological molecules. From these, the structure of the molecule can be recovered at a resolution of $2\AA$, which is sufficient to show the location of individual atoms in the molecule. The principle of iterative phase retrieval by oversampling pioneered by J. Miao (4), in which unique phase information about the wave front is recovered from a diffraction pattern, has already been demonstrated experimentally using X-rays and high energy electrons, limited however to robust inorganic samples.

[6] The Linac Coherent Light Source (LCLS) in the USA, http://www-ssrl.slac.stanford.edu/lcls/, to be completed in 2009, will be the world's first X-ray free electron laser for the creation and study of exotic states of matter, imaging structures and dynamics of biological and chemical molecules on an atomic scale and probing the fundamental aspects of atomic structure. A similar project, DESY in Germany, http://www.desy.de/html/home/index.html is expected to be operational by 2012. More recently, a Swiss XFEL project has been initiated at the PSI, http://fel.web.psi.ch.

13.2 The coherent electron diffraction microscope

The overall setup of the coherent electron diffraction imaging experiment is sketched in Fig. 13.1. A sharp W-tip acts as a field emitting electron point source of a coherent spherical electron wave of energies between 20 and 300 eV. A micro-lens placed a few microns away from the electron emitter forms a coherent parallel wave that impinges onto a molecule attached to a micro-structure some distance behind the lens in a field-free region. At a distant detector, the amplitude of the diffraction pattern, which corresponds to the Fourier transform of the diffractive object, is recorded with high spatial resolution. In order to be able to sample this pattern with sufficiently high frequencies to match the oversampling requirement, the object must be surrounded by a no-density region.

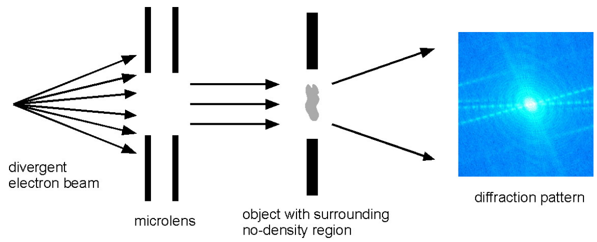

Figure 13.1: Schematic representation of the coherent electron diffraction microscope.

13.2.1 Experimental setup

A new diffraction microscope has been designed and built featuring a dedicated detector system for obtaining oversampled diffraction patterns (see Fig. 13.2). It comprises a micro-channel plate, a small grain phosphor screen directly deposited onto a fibre optic plate and a high resolution CCD camera. An electrochemically etched single tungsten (111) crystal, as used in LEEPS microscopy, serves as the source of coherent low energy electrons. It is mounted on a three-axis manipulator so that the tungsten tip can be positioned with a precision of 50 nm. The sample is mounted on a separate four-axis manipulator to enable centering in the beam. An additional degree of freedom for rotating the sample has been included so that diffraction patterns at various tilt angles can be acquired.

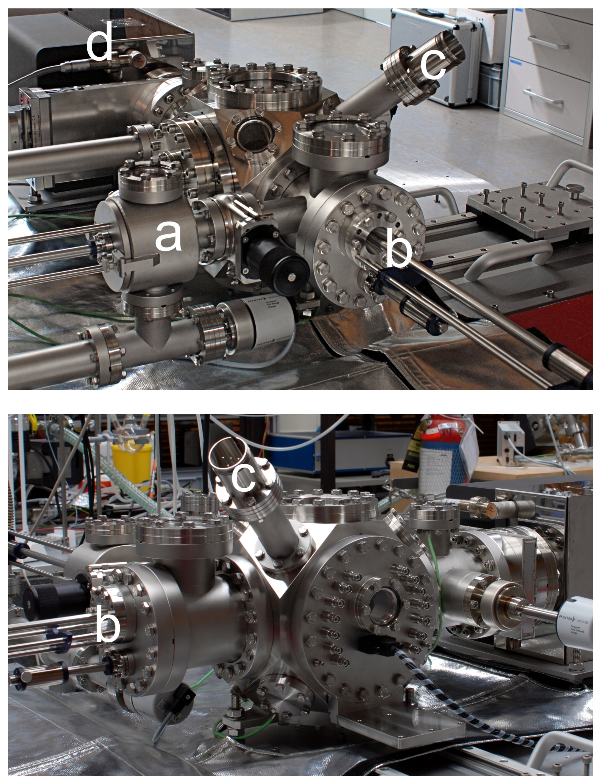

Figure 13.2: Vacuum chamber of the Coherent Diffraction Microscope. It comprises a load-lock (a) for rapid sample transfer, a wobble-stick (b) for flexible sample manipulation, a secondary-electron detector (c) for possible future applications and an elaborate pumping-system (d) to achieve UHV conditions.

The microscope has been designed to match the requirements of the oversampling phasing method and to optimise the

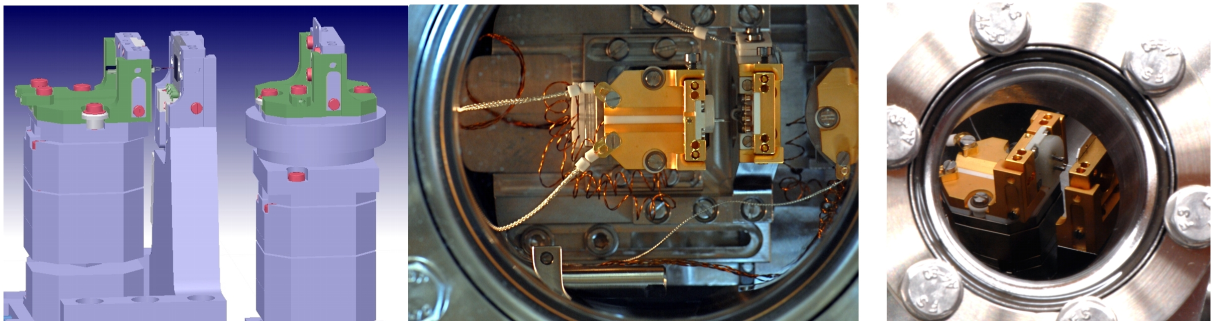

Figure 13.3: Electron source and sample are attached to manipulators featuring nm precision (schematic at left). A top (middle) and side view (right) into the Coherent Diffraction Microscope.

recording of diffraction patterns. These requirements on the experimental setup are summarized by:

$$\Delta \leq z\frac{\lambda}{Oa} \ ,$$

where λ is the wavelength, a the object size, Δ the pixel size of the detector, z the object-screen distance and O the square root of the ratio of the size of the no-density region surrounding the sample and the sample size, the so called oversampling ratio. The resolution is limited by the size of the detector, the sample-detector distance, the wavelength of the electrons, the oversampling ratio and the temporal coherence of the electron wave. With a state of the art pixel detector and a temporal coherence of the electron wave which is approximately 0.0005 for 200 eV electrons, an ultimate resolution of 0.70 $\AA$ could eventually be reached.

13.2.2 Electrostatic micro-lens

In the coherent diffraction microscope the micro-lens shall collimate the divergent electron beam emitted from the tungsten tip to form a parallel beam which is directed onto the molecule. The overall idea of employing a micro-lens is associated with the fact the electron lenses suffer from intrinsic spherical aberrations, essentially since there exists no concave electron lens, as has been recognized by Scherzer (5) a long time ago. Our way of circumventing the Scherzer theorem is to scale down electron source and lens dimensions. Since our electron source exhibits already an ultimate size of atomic dimension it is thus a matter of scaling down the lens and placing it at a short distance from the source. The lens diameter is directly associated with the spherical aberration Cs, as illustrated in Fig. 13.4 for a two-electrode lens. A typical macroscopic lens has an inner bore exhibiting centimeter

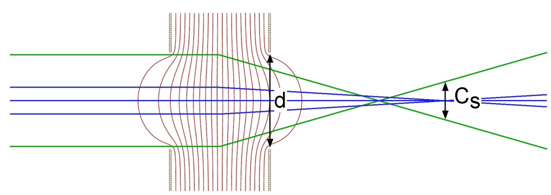

Figure 13.4: Schematic to illustrate the implication of lens dimensions d on the intrinsic spherical aberration Cs creating a disk of least confusion in the Gaussian focal plane of an electron lens.

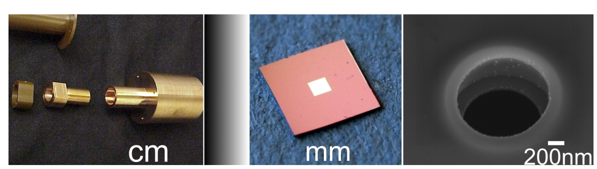

Figure 13.5: From left to right: macroscopically machined lens with centimeter dimension bore, silicon wafer with SiN window, electrostatic lens with 1 micron aperture.

dimension as illustrated in Fig. 13.5. We use a 5 mm by 5 mm silicon chip with a 1 mm by 1 mm SiN window of 1 micron thickness to form a micro-lens. With appropriate micro-machining techniques, explained in some detail below, we end up with a lens exhibiting an aperture of just 1 micron as shown in the SEM image at the right of Fig. 13.5. In comparison to conventional lenses, we have scaled lens dimension and thus spherical aberration by four orders of magnitude.

13.2.3 Micro-lens designs

During the past two years, we developed several procedures for fabricating micro-lenses. Principally, the lens consists of two carbon electrodes, separated by an insulating layer, with micrometer-sized apertures (see Fig. 13.6. Ray tracing calculations have shown that such design leads to lenses exhibiting the desired properties, in particular, the ability of the insulating layer to withstand the potential difference between the electrodes needed to collimate the electron beam. For the detailed fabrication of the lens there exist several approaches ranging from assembling the lens manually to more elaborate methods requiring several steps of evaporation and micro-structuring.

One of the methods considered as promising starts with the structuring of a 5 μm large hole in a 1 μm thick SiN membrane with the help of our focused ion beam (FIB) machine. Afterwards, two carbon flakes, previously deposited onto mica sheets, are transferred on

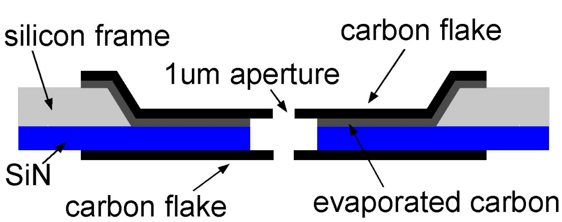

Figure 13.6: Schematic side-view of a micro lens.

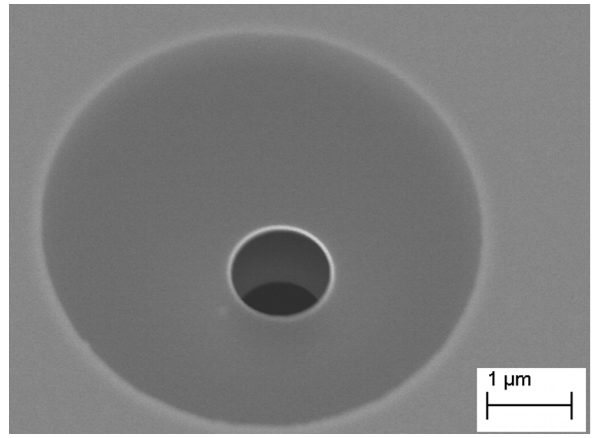

Figure 13.7: SEM image of a micro-lens taken at a tilt angle of 30°. The 5 micron bore covered on each side by a thin carbon flake is still visible.

both sides of the structured membrane. Finally, the 1 μm lens aperture is structured in the free-standing carbon flakes deposited over the 5 μm hole. A SEM image of the final result is presented in Fig. 13.7.

The picture series displayed in Fig. 13.8 demonstrates clearly that we are able to produce a parallel electron beam. To further characterize the lens focusing properties, the dependence of the focal length on the applied voltage has been extracted from several series of projection images. This demonstrates that the fabricated lenses work as expected and that our ray-tracing simulations are a reliable tool for designing electrostatic optical elements on a micrometer scale and shall in the future serve us as a guide for more elaborate micro-lens systems.

The next step shall be to place a single molecule into the parallel beam generated by the micro-lens and record a diffraction patter with a high sampling ratio.

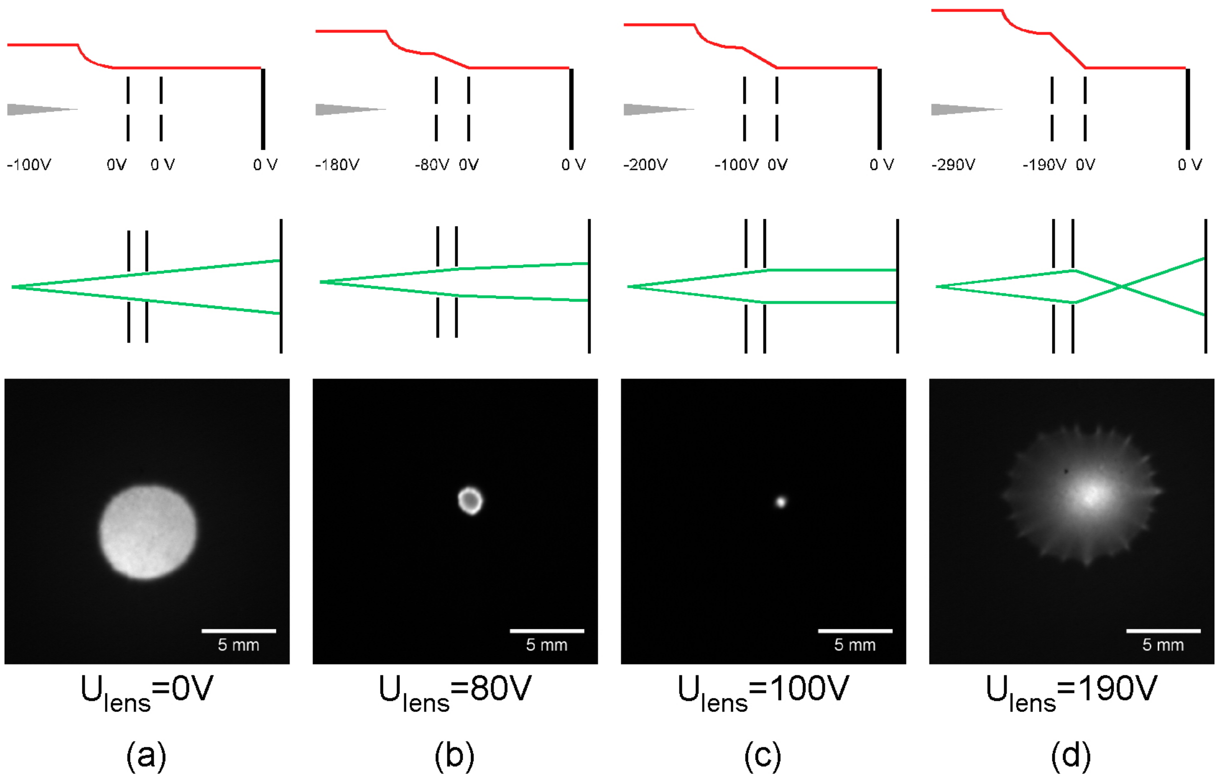

Figure 13.8: Series of projection images of a lens with varying negative voltage at the first lens electrode. For each projection image the corresponding potential energy of the electrons and the focusing situation are displayed. (a) Projection image of the lens aperture without applied voltage, (b) beam with a reduced divergence angle, (c) parallel beam impinging onto the detector, (d) cross-over point only a few microns behind the lens. In all situations, the distance between tip and lens amounts to approximately 8.5 μm and the lens to detector distance is fixed to 70 mm.

[1] M. van Heel et al., Quart. Rev. Biophys. 33 (2000) 307.

[2] J. Frank, Ann. Rev. Biophys. Biomol. Struct. 31 (2002) 303.

[3] M. Germann, T. Latychevskaia, C. Escher, H.-W. Fink, to be submitted.

[4] J. Miao et al., Nature 400 (1999) 342.

[5] O. Scherzer, Z. f. Physik 101 (1936).

14 Physical Systems Biology and non-equilibrium Soft Matter

C.M. Aegerter, U. Nienhaus (since April 2009), M. Schindlbauer (Bachelor student), T. Schluck (since September 2008), I.M. Vellekoop (since September 2008)

in collaboration with:
Institute of Molecular Biology (K. Basler, T. Aegerter-Wilmsen), Institute of Zoology (C. Lehner, S. Luschnig), ETH Zürich (E. Hafen, I. Sbalzarini, P. Koumoutsakos), EPF Lausanne (P. Renaud, D. Floreano), University of Lausanne (S. Bergmann), Biozentrum Basel (M. Affolter), University of Strasbourg (N. Rivier), University of Konstanz (G. Maret, W. Bührer, S. Fiebig, N. Isert, C.C. Maass), Deutsches Luft- und Raumfahrtzentrum (M. Sperl), University of Twente (A. Mosk), Universite Joseph Fourier Grenoble (S. Skipetrov, F.Graner), Technion Haifa (E. Akkermans).

Work in the group of physical systems biology and non-equilibrium soft-matter is concerned with the study of developmental biology using physical techniques. In this, we are developing novel imaging techniques for in-vivo imaging in turbid environments, as well as studying the influence of mechanical stresses on developmental processes. This implies that we are developing tools with which to measure mechanical stresses in live biological tissues as well as methods to stimulate these tissues using suited levels of force. The biological model system we are studying is the wing imaginal disc of *Drosophila*, which is a proto-organ that develops into the adult wing of the fly during metamorphosis. In years of genetic characterisation, this tissue in the fly's larva has been extensively studied and a host of genetic manipulation tools have been developed. Thus it is possible in a system like the wing imaginal disc to investigate the interplay of genetic factors and mechanical properties, which are also implied by the environment. In these projects on the development of organs in *Drosophila*, we are closely collaborating with Biology groups. In addition, we take the study of elastic properties of biological tissues as a starting point in the investigation of the properties of growing soft matter, where our model system consists of two dimensional foams, which form structures akin to the epithelial tissues we study in Biology.

In addition, we are interested more generally in phase transitions and non-equilibrium behaviour. For this purpose, we also study Anderson localization of light in turbid media, the dynamics of granular gases under microgravity, as well as that of levitated three dimensional foams. These investigations in turn influence our development of imaging techniques, as well as the study of mechanical properties of soft condensed matter.

14.1 Granular materials

In collaboration with the University of Konstanz, we are studying the behaviour of granular gases using diamagnetic levitation (1). Due to the levitation of the particles, it is possible to study the behaviour of the grains as a function of time when the excitation is switched off. Under normal circumstances, this behaviour is completely masked by the gravitational effect of grains falling to the bottom of the container. Due to the inelasticity of collisions between grains, the particles continually loose energy, which is a fundamental ingredient in the theoretical description of granular gases using kinetic theory. This has led to a description of the freely cooling granular gas by Haff more than 25 years ago (2), which is used as a ground state in the description of excited granular gases (3).

Using a collection of monodisperse Bismuth shots, we have created a granular gas in the bore of a strong superconducting solenoid (4). At an applied field of 13.5 T, the field gradient at the edge of the solenoid is strong enough such that the diamagnetic susceptibility of Bismuth leads to a repulsive force that equals gravity. Exciting the granular gas using an alternating component of the levitating field, a stable granular gas is created. When switching off this excitation, the cooling of the gas can be observed directly by studying the mean speed of the particles. According to Haff, the mean speed in a homogeneous gas should decrease with time as

$$\langle|v|\rangle(t) = \frac{\langle|v|(0)\rangle}{1 + t/\tau_H}, \qquad (14.2)$$

where τ_H is a time scale dependent on the mean free path of particles between collisions, their coefficient of restitution as well as the initial speed of the particles.

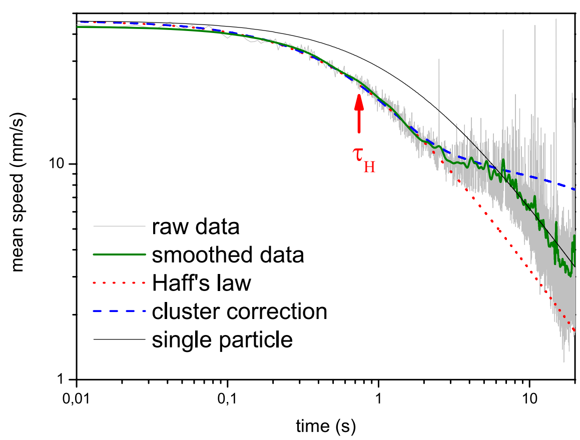

Figure 14.1:
The cooling of a granular gas as studied by video-imaging. As can be seen, the mean speed of the particles decreases as the excitation is switched off at time t = 0. The dotted line gives the prediction of Haff's law, which is adjusted for the presence of a cluster of particles in the gas in the dashed line. The thin solid line finally gives another Haff-like behaviour when the mean free path of particles becomes equal to the container size.

As can be seen in Fig. 14.1, the experimentally determined speeds are in good agreement with Haff's law at early times, where the gas is still homogeneous as indicated by the dotted line. At later times, the particles tend to form a cluster, which leads to an increase in the mean free path and thus a slowing down of the cooling process. This can also be seen in the data and the mean free path can be directly determined from the number of particles outside the cluster. Thus Haff's law can be adjusted to describe a clustering gas as well, indicated by the dashed line in Fig. 14.1, which is in good agreement with the data. Note that in the description of the data, no adjustable parameters were used since the parameters describing the Haff time τ_H can all be determined independently.

[1] W. Braunbek, Z. Phys. **121**, 764 (1939).

[2] P.K. Haff, J. Fluid. Mech. **134**, 401 (1983).

[3] X. Nie, E. Ben-Naim, and S. Chen, Phys. Rev. Lett. **89**, 204301 (2002).

[4] C.C. Maass, N. Isert, G. Maret, and C.M. Aegerter, Phys. Rev. Lett. **100**, 248001 (2008).

14.2 Coherent backscattering of light

When shining light onto a turbid medium, there is an enhancement of the backscattered light in the exact back-direction (1). This is due to the interference between reciprocal paths inside the multiply scattering sample, a phenomenon giving rise to Anderson localization in the strong scattering limit (2). In spite of the fact, that this enhancement has been known experimentally for almost 25 years, the standard description of the effect (3) still leads to an excess of backscattered intensity for extremely turbid samples, which would break the conservation of energy. Using our carefully calibrated setup, which is able to cover almost the whole angular range of reflections (4), we have studied the absolute enhancement in coherent backscattering (5). There we could show that there is a suppression of enhanced intensity at higher angles that exactly compensates for the backscattered enhancement at small angles. This suppression is due to interference effects arising when the first and last scatterer are within a wavelength of the incoming light and can be described by diagrammatic theory (6), which can be applied to the problem of coherent backscattering and is in excellent agreement with our measurements (5), see Fig. 14.2.

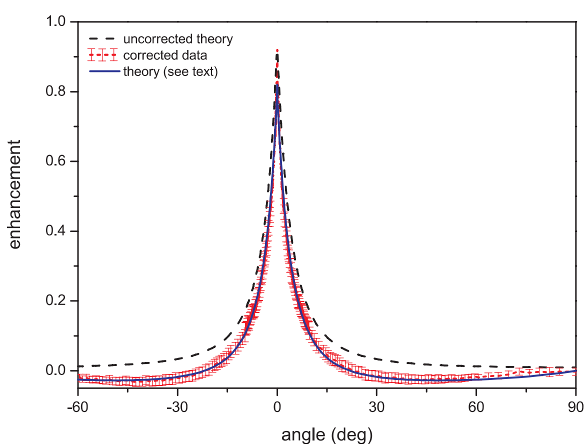

Figure 14.2:
The enhancement of backscattering due to path reciprocity in turbid media over a wide range of angles. Due to the wide angular resolution, it is possible to see a reduction of enhancement at angles around 45°, which makes sure that the enhancement in intensity fulfills conservation of energy. This can be described theoretically using a Hikami box [6], which describes the diffraction limit effect of two sources moving closer than a wave length. The corresponding theory is plotted as the dashed line. Without this effect, the dotted line is obtained which would be in conflict with conservation of energy.

[1] M.P. van Albada and A. Lagendijk, Phys. Rev. Lett. **55**, 2692 (1985); P.E. Wolf and G. Maret, Phys. Rev. Lett. **55**, 2696 (1985).

[2] P.W. Anderson, Phys. Rev. **109**, 1492 (1958).

[3] E. Akkermans, P.E. Wolf, and R. Maynard, Phys. Rev. Lett. **56**, 1471 (1986).

[4] P. Gross, S. Fiebig, M. Störzer, M. Clausen, G. Maret, and C.M. Aegerter, Rev. Sci. Instr. **78**, 033105 (2007).

[5] S. Fiebig, C.M. Aegerter, W. Bührer, M. Störzer, E. Akkermans, G. Montambaux, and G. Maret, Europhys. Lett. **81**, 64004 (2008).

[6] S. Hikami, Anderson localization in a nonlinear-σ-model representation, Phys. Rev. B **24**, 2671 (1981).

14.3 Measurements of mechanical stress in the wing imaginal disc of Drosophila

On the side of organ development, we have recently studied the regulation of growth in the wing imaginal disc theoretically and proposed a model for size regulation with an important role for mechanical forces creating a feedback acting on the growth rates of the system (1). Here, the main point was to show through simulations of a simplified model that inhomogeneous growth as is probably present in the initial stages of the wing imaginal disc due to a graded presence of growths factors, such as decapentaplegic or wingless can lead to a homogenization of the growth rates via mechanical feedback. In addition, the distribution of stresses in the tissue, which was assumed to be completely elastic, leads to a regulatory feedback controlling the cessation of growth via compressional forces in the locations of high growth factor concentration. A similar model has been put forward independently by another group as well (2; 3), which together with our study has lead to an increased interest in the study of mechanical forces in the development of organs in Drosophila.

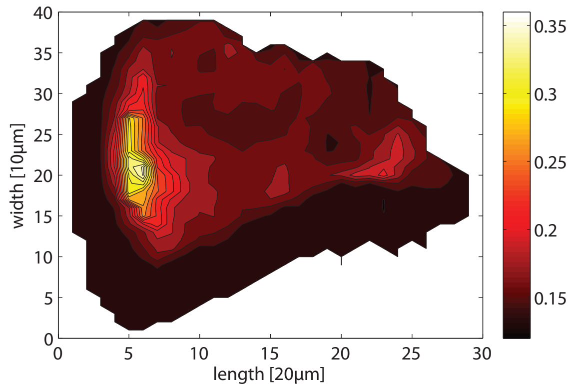

Figure 14.3:
Distribution of retardance in the wing imaginal disc of a late third instar larva. As can be seen, the retardance is highest in the centre of the wing pouch, where the orientation of the retardance and hence the stress can be checked by a rotation of the incoming polarization of the light. This shows that the stresses in the wing pouch are roughly radially distributed as is predicted by the models [1; 3].

In order to study the implications of this model, we have in the following begun the experimental study of the mechanical properties of the wing imaginal disc. As a starting point, we have studied the stresses present in wing discs of different ages using a setup to accurately measure birefringence and thus determine the stresses via photoelasticity. In a photoelastic experiment, the change in retardance of a material is measured under an applied stress. This retardance is given by the birefringence of the material as well as its thickness. Under an applied stress, the birefringence changes in proportion to the stress, because of the change in the electronic properties induced by the stress. In these experiments, we have used a sophisticated method of measuring the retardance directly (4), which yields the phase difference due to birefringence and thus the stress. The nature of this setup leads to a poor spatial resolution since the illumination needs to be scanned across the sample and thus is limited to 20 μm. This can however be increased in principle to the sub-cellular level by the inclusion of such a setup to a wide field microscope (5), which we are currently building up. We should therefore be able to measure the stress distribution to the cellular and sub cellular level in in-vitro wing imaginal discs in the future.

The present, preliminary investigations have already indicated the presence of a mechanical stress distribution with a radial maximum at the centre of the wing pouch, where compressional stresses are predicted by the models discussed above (1; 3), see Fig. 14.3. The extent of these stresses inside the wing imaginal disc is also seen to increase with age of the wing disc(6), still as predicted by the theoretical models. In addition, other predictions concerning the stress distribution could be tested, such as the temporal development of the peripheral tensile stress, where the predictions of the two models differ strongly. One of the models predicts an increasing stress (3), whereas the other predicts a constant or slightly decreasing stress (1). Our results indicate a temporally constant stress in the periphery of the wing disc in agreement with (1). These results are currently being submitted for publication (6).

[1] T. Aegerter-Wilmsen, C.M. Aegerter, E. Hafen, and K. Basler, Mech. Develop. **124**, 318 (2007).

[2] B.I. Shraiman, Proc. Natl. Acad. Sci. USA. **102**, 3318 (2005).

[3] L. Hufnagel, A.A. Teleman, H. Rouault, S.M. Cohen, and B.I. Shraiman, Proc. Natl. Acad. Sci. USA. **104**, 3835 (2007).

[4] G. Maret, M. v. Schickfus, A. Mayer, and K. Dransfeld, Phys. Rev.Lett. **35**, 397 (1975).

[5] R. Oldenbourg, Nature **381**, 811 (1996); R.J. Wijngaarden, M.S. Welling, C.M. Aegerter, and K. Heek, NATO Science Series II: **142**, 61 (2004).

[6] U. Nienhaus, T. Aegerter-Wilmsen, and C.M. Aegerter, to be published (2009).

15 Mechanical Workshop

K. Bösiger, B. Lussi, R. Maier, M. Schaffner, S. Scherr, O. Fardin (apprentice) and T. Naterop (apprentice)

With the modern tools of the mechanical workshop we produce, besides equipment for the research groups at the institute, an increasing number of parts for other departments of the University. For outside companies construction and modification work was done and we built prototypes and produced limited-lot series. The resulting income was used to supplement and extend the central store. Also new tooling and the continuing education of the workshop staff and the apprentices could be financed this way.

The central metal and technical material store maintained by us[7] supplies more than 30 institutes with materials and technical support. In November 2008 we organized for the second time an information meeting with the central store customers. The large number of attendants shows that our services are highly appreciated.

With a small investment we replenished the equipment of the welding shop with an electrical rotary draw tube and pipe bending machine. The device is programmable and the bending capacity goes up to 42 mm in diameter. In the training workshop also used for the basic courses we replaced a 35 years old lathe of the type "Schaublin 135" with the later model "Schaublin 125". The second hand machine could be obtained from the hardware marketplace maintained by the University. Dedicated central spanning bench vices were purchased for use on the modern milling machine with five axes. With these devices an easier and more accurate handling can be achieved.

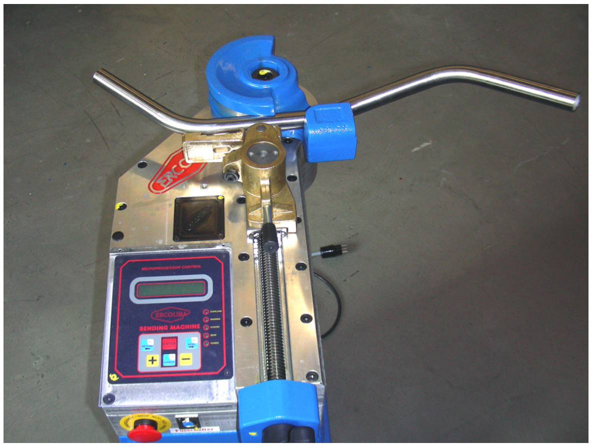

Figure 15.1: The new bending machine.

Below we list some of our main projects and activities during 2008.

- **Basic mechanical workshop courses**
  For the bachelor students we organize two basic courses. During the first stage the candidates learn how to use all kinds of measuring tools and accomplish simple work on drilling and milling machines as well as on the lathe. They learn how to read and produce technical drawings and the course ends with an introduction in the technique of hard soldering. In the second stage more demanding machining techniques are trained. Different materials are handled and an introduction into various welding processes is given. We had to arrange again four courses of 35 hours each because of the large number of students. The students appreciate the courses very much. In March 2009 an in-house introductory workshop course was arranged for the interested research staff. This one-week course will be repeated periodically.

[7] For a catalogue see http://www.physik.unizh.ch/groups/werkstatt/dienstleistung.html

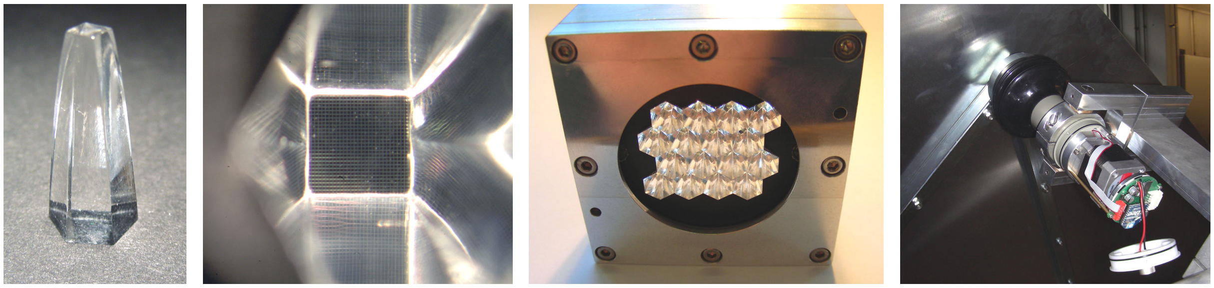

Figure 15.2: From left to right: two views of a prototype Winston Cone light concentrator, an array of 16 such cones and a picture of one actuator mounted on the mirror dummy prototype.

- **XENON Experiment (Sec. 4)**
  A photomultiplier test setup was built and different parts made out of Teflon were produced for the XENON experiment built up at the Gran Sasso laboratory in Italy.

- **CTA Cherenkov Telescope Array**
  Winston Cone light concentrators were produced using acrylic glass, which is transparent for ultraviolet light. We built a prototype test system with dummy mirror and the necessary actuators for the precise positioning of the mirrors (see Fig. 15.2).

- **LHCb silicon tracking detector (Sec. 8)**
  We renewed the cooling system of the electronic crates for the silicon tracker.

- **Surface Physics (Sec. 12)**
  We built several devices for Bachelor- and Master-thesis experiments carried out in this research group (see Fig. 15.3). Different evaporators were built and we manufactured parts used for evaporation deposition made out of molybdenum and stainless steel. New probe holders were provided as well. Maintenance and repair work was performed during the reporting period.

- **Solid State Physics (Sec. 10)**
  For this research group we produced sample holders and complete probe manipulators. Again different coil shells made out of different materials were manufactured. We started the development and construction of a new demonstration experiment with a running train supported by cooled high-temperature superconductors floating in a magnetic field. The setup will also be shown during public events.

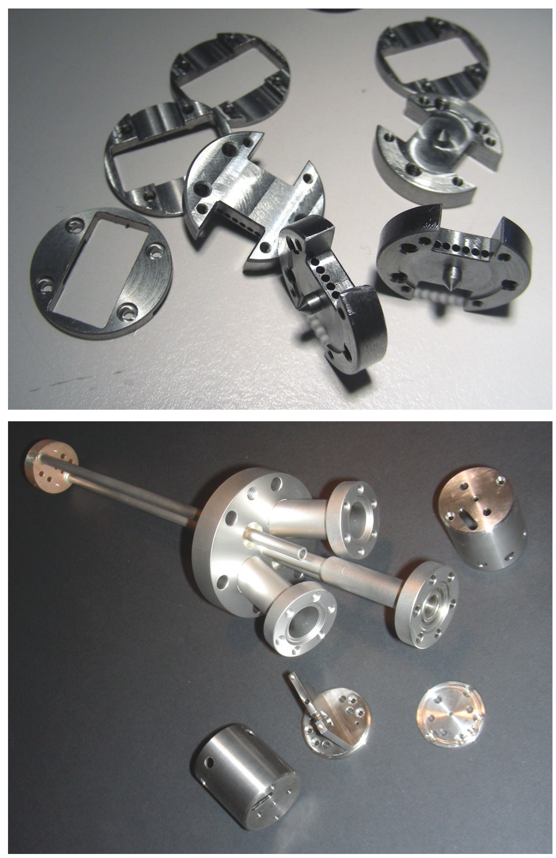

Figure 15.3: Parts of a sample holder made out of molybdenum and stainless steel. The lower picture shows a custom-made evaporator.

- **Physics of Biological Systems (Sec. 13)**
  We started the production of a dedicated vapour deposition device with six coating stations (Fig. 15.4). Maintenance and repair work was performed as well.

- **Continuing education of the workshop staff**
  In August 2008 an internal course in modern metrology techniques was organized. During four days we learned and trained the operation of the measuring machine installed in the workshop. Seminars and innovation days in relation with modern processing methods and materials were attended including the international trade fair "PRODEX" which shows the latest machine tools and accessories. CAM software courses were attended and assessments in welding were made.

- **Education of the apprentices**
  Between the April 28 and May 9 we organized trial apprenticeship for candidates interested in getting a grade as polytechnician. Besides the mandatory Swiss-mechanic courses the apprentices attended again advanced courses in computer controlled machine (CNC) programming, pneumatics and electronics. In February and March 2009 the apprentices started their preparation for their intermediate and final exams. For the project work which the apprentices have to perform in the fourth year of their education different parts for a V8 combustion engine were manufactured on the drilling and milling machines in our workshop (Fig. 15.5).

- **Miscellaneous**
  In April 2008 on the occasion of the 175th anniversary of the University of Zürich the apprentices designed and installed an exhibition stand (Fig.15.6). They informed about their work and demonstrated different devices built in the workshop. We visited a bio-fuel production plant in May 2008.

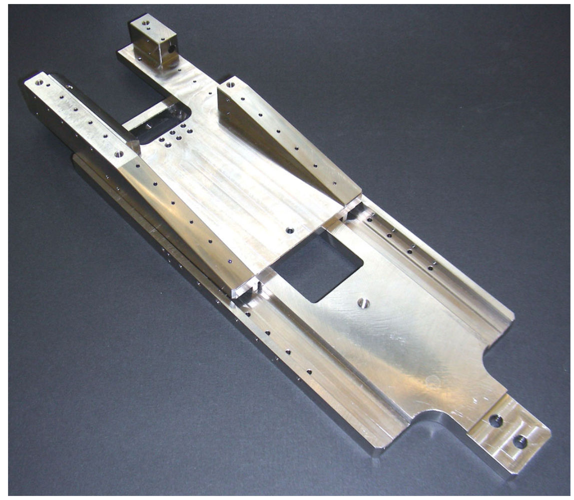

Figure 15.4: Component for the dedicated vapour deposition device with six coating stations.

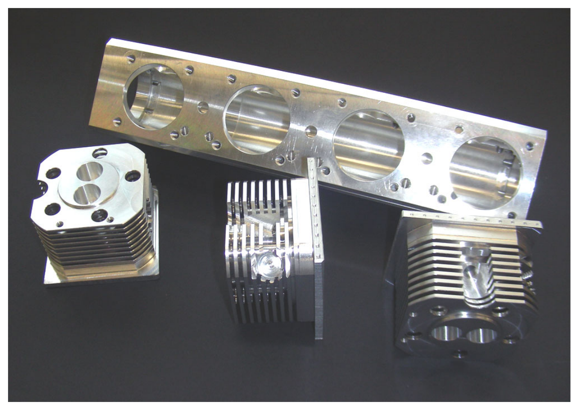

Figure 15.5: Cylinder heads and the crankcase for the V8 combustion engine.

Figure 15.6: Exhibition stand with running demonstrations. In the foreground a steam engine built in the workshop can be seen.

16 Electronics Workshop

W. Fässler, Hp. Meyer, P. Soland, and A. Vollhardt

During the reporting period the electronic workshop contributed to many projects of our institute, such as:

- With the delivery and successful installation mid 2008 of the components designed and manufactured for the CMS pixel detector at CERN our activities for this project were terminated. Meanwhile the complete system is integrated into the CMS detector and measurements with cosmic rays show that the detector system performs very well.
- The involvement in the installation and commissioning of the trigger tracker system of the LHCb experiment proceeds. Some laser diodes of the readout system had to be replaced and the cooling system of the electronics was upgraded.

Figure 16.1: Part of the readout electronics of the LHCb trigger tracker.

- The secondary particles generated in the atmosphere by high-energy gamma rays produce Cherenkov radiation which can be detected by optical telescopes. The Cherenkov Telescope Array (CTA) Project aims at building the next generation ground-based gamma-ray telescope. Two arrays of optical telescopes are planned. A southern hemisphere array, covering the energy range from some 10 GeV to about 100 TeV will allow for a detailed investigation of galactic sources including the central part of our Galaxy and for the observation of extragalactic objects. A northern hemisphere array, sensitive in the low energy region from some 10 GeV to $\sim$1 TeV is dedicated mainly to extragalactic objects. The required mirror diameter of about 20 m can only be realized by segmentation. The individual mirror facets span an area of 2.5 m^2.

Mechanical instabilities in the support structure of the telescope require a continuous alignment of the facets with respect to a reference position. This is done with two precise actuators installed on every segment. The electronic workshop developed and built the control electronics for a prototype system. The devices allow a range of operation of 35 mm with a precision of $\sim$35 μm. To minimize cabling a wireless communication is planned with the central control processor. To test the actuators under realistic conditions with constant exposure to the environment we are presently building a remote controlled test setup with a dummy mirror facet. It will be installed in spring 2009 on the roof of the institute's building. Whereas the actuators are permanently moving we record the actual positions and weather condi-

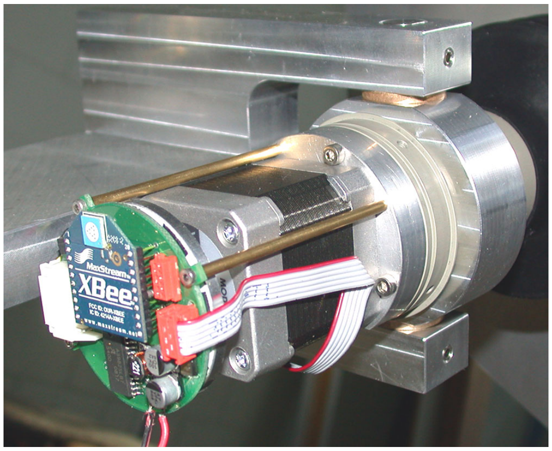

Figure 16.2: Prototype actuator for the CTA experiment with the control electronics and the wireless communication unit. Two of these are used to align one single mirror facet.

tions. The data will be analyzed and used to find correlations and possible impacts.

- For a new spin polarimeter of the Surface Physics group we constructed fast programmable discriminators and a high-speed interface. The discriminators had to be small since they have to fit in the detector head near the GAPD sensor.

- For the XENON experiment a dedicated bipolar power supply and special ultra-clean PMT bases made out of a Teflon substrate were built.

- We are also coordinating the development and construction of a new demonstration experiment with a running train supported by cooled high temperature superconductors floating in a magnetic field. Among others we built different adaptor boxes with the necessary dedicated cables and a simple motor control unit for a new student experiment which measures the gravitational constant.

- In collaboration with L. Pauli and M. Weber (J. Seiler retired in June 2008), who are responsible for the preparation of the demonstration experiments, we renewed and improved again some experiments. As an example Fig. 16.3 shows the renewed control unit and the actual user interface of the microwave scattering demonstration experiment.

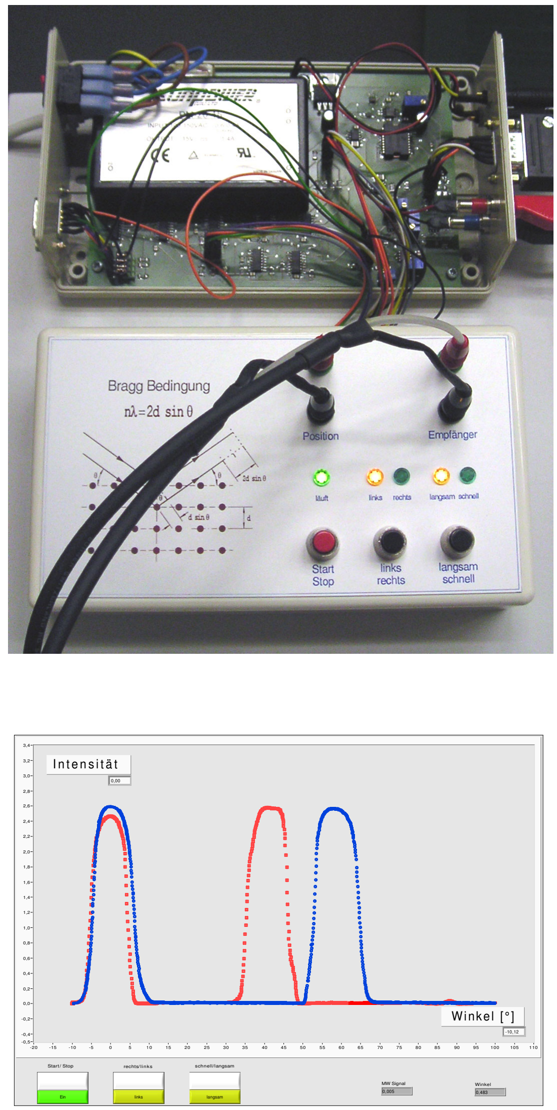

Figure 16.3: The renewed control unit and the computer user interface of the Bragg demonstration scattering experiment. The curves show two measurements with different orientation of the crystal model axis.

The electronics workshop supported all research groups in maintaining and repairing the existing devices and equipment. Thanks to a supplementary credit we could purchase some new tooling which helps in assembling cables. The Automatic Cutting Machine cuts wire, cable, round material such as tubing, flat ribbon and Glass Fiber Optic cable. This unit can process wires up to 21 mm^2, cuts round material up to 15 mm in diameter and cuts flat material up to 100 mm wide. Programming and operation is performed with a user-friendly control panel. The Stripping Machine is an electric wire and cable stripping machine for a wide range of single conductor wires, either stranded or solid up to 4.7 mm in diameter for partial strips, respectively 3.2 mm in diameter for full strips. It strips lengths up to 25 mm and handles wires from 0.03 to 5.26 mm^2. The machine is highly portable, compact and fast and powerful. Stripping of most insulation types with one set of blades is no problem with this robust machine. The stripping length and stripping diameter are easily adjustable, allowing quick changeover between different types of wires. In addition, the unit is also capable of partial and full insulation strips.

In April 2008 on the occasion of the 175th anniversary of the University of Zürich the workshop staff arranged and installed an exhibition stand. We provided different electronic construction sets and the necessary tooling for the assembly of the devices. Interested visitors were invited to assemble their own part with our help and instruction. Guests, primarily children with their parents, were building electronic devices with an amazing enthusiasm all day until the last resistor was soldered to the final remaining printed circuit board.

17 Publications

17.1 Elementary particles and their interactions

17.1.1 ArDM

Articles in press

- **Development of wavelength shifter coated reflectors for the ArDM argon dark matter detector**
  V. Boccone *et al.*, Journal of Instrumentation.

- **The ArDM project: A Liquid Argon TPC for Dark Matter Detection**
  V. Boccone, Proc. XIII Int. Conf. on Calorimetry in High Energy Physics (CALOR 08), Pavia, 2008, arXiv:0810.4490v1, Journal of Physics.

Invited Lectures

- V. Boccone: **The ArDM project: A Liquid Argon TPC for Dark Matter**
  XIII Int. Conf. on Calorimetry in High Energy Physics (CALOR 08), Pavia, 28 May 2008.

- P. Otyugova: **The ArDM - 1 ton Experiment**
  3rd CHIPP Neutrino Meeting, Zurich, 17.-18. November 2008.

- C. Regenfus: **The Argon Dark Matter Experiment (ArDM)**
  4th Patras Workshop on Axions, WIMPs and WISPs, DESY, Hamburg, 19 June 2008.

17.1.2 ATHENA

Article

- **Temporally Controlled Modulation of Antihydrogen Production and the Temperature Scaling of Antiproton-Positron Recombination**
  M.C. Fujiwara *et al.*, Phys. Rev. Lett. **101** (2008) 053401.

17.1.3 CDMS

Article

- **Search for Weakly Interacting Massive Particles with the First Five-Tower Data from the Cryogenic Dark Matter Search at the Soudan Underground Laboratory**
  CDMS Collaboration, Phys. Rev. Lett 102, 011301 (2009).

Invited lectures and conference contributions

- L. Baudis: **Direct Detection of Cold Dark Matter with CDMS and XENON**
  LAPTH Seminar, LAPP Annecy, June 27 2008.
- T. Bruch: **Recent results from the CDMS-II experiment**
  4th PATRAS Workshop, DESY, Hamburg, June 19 2008.
- S. Arrenberg: **Hunting for Dark Matter with the CDMS Experiment**
  MINOS Collaboration Meeting, Ely, June 11, 2008.
- T. Bruch: **Search for Axions with the CDMS-II Experiment**
  DPG, LMU Munich, Germany, March 9 2009.

17.1.4 CMS

Articles

- **The CMS experiment at the CERN LHC**
  S. Chatrchyan *et al.*, Journal of Instrumentation **3** (2008) S08004.
- **B physics at CMS**
  T. Speer, Proc. 2007 Eur. Conf. on High Energy Physics, Manchester, Journal of Physics: Conference Series **110** (2008) 052049.
- **Beauty Production and Identification at CMS**
  A. Schmidt, Nuclear Physics B (Proceedings Supplements) **187** (2009) 216.
- **Fast Simulation of the CMS Detector at the LHC**
  A. Schmidt, IEEE Nuclear Science Symposium Conference Record **N37-4** (2008) 2795.
- **A novel technique for the reconstruction and simulation of hits in the CMS Pixel Detector**
  V. Chiochia, IEEE Nuclear Science Symposium Conference Record **N27-3** (2008) 1909.

Articles in press

- **Mechanical Design and Material Budget of the CMS Barrel Pixel Detector**
  C. Amsler *et al.*, Journal of Instrumentation (2008).
- **Position resolution for the CMS Barrel Pixel Detector after irradiation**
  E. Alagöz, Proc. 11th Topical Seminar on Innovative Particle and Radiation Detectors, Siena, Nucl. Phys. B.
- **Experience with CMS pixel software commissioning**
  V. Chiochia, Proc. 17th Int. Workshop on Vertex detectors (Vertex 08), Stockholm, 2008, arXiv:0812.0681, Proceedings of Science.

- **Searches for New Phenomena at CMS and ATLAS**
  T. Rommerskirchen, Moriond QCD and High Energy Interactions, La Thuile, 2009.

- **Heavy Flavour Physics at CMS and ATLAS**
  L. Wilke, Moriond QCD and High Energy Interactions, La Thuile, 2009.

CMS notes and reports

- **Impact of Tracker Misalignment on the CMS b-tagging performance**
  A. Schmidt *et al.*, CMS Note AN-2007/047.

- **SUSY searches with dijet events**
  T. Rommerskirchen and the CMS collaboration, CMS Physics analysis report SUS-08-005.

- **Beauty Production and Identification at CMS**
  A. Schmidt, CMS Conference report CR-2008/061.

- **Gamma ray bursts: observation and theoretical conjectures**
  E. Alagöz *et al.*, CERN Yellow report 2008-004 (2008) 287.

Invited Lectures

- E. Alagöz: **Position resolution for the CMS Barrel Pixel Detector after irradiation**
  11th Topical Seminar on Innovative Particle and Radiation Detectors, Siena, 3 October 2008.

- V. Chiochia: **Experience with CMS pixel software commissioning**
  17th Int. Workshop on Vertex detectors (Vertex 08), Stockholm, 27 July 2008.

- V. Chiochia: **A novel technique for the reconstruction and simulation of hits in the CMS Pixel Detector**
  IEEE Nuclear Science Symposium, Dresden, 19 October 2008.

- T. Rommerskirchen: **Searches for New Phenomena at CMS and ATLAS**
  Moriond QCD and High Energy Interactions 2009, La Thuile, 17 March 2009.

- A. Schmidt: **Fast Simulation of the CMS Detector at the LHC**
  IEEE Nuclear Science Symposium, Dresden, 20 October 2008.

- A. Schmidt: **Beauty Production and Identification at CMS**
  Eighth Int. Conf. on Hyperons, Charm and Beauty Hadrons (BEACH2008), Columbia, USA, 22 June 2008.

- L. Wilke: **LHC status and upgrade plan: CMS**
  Meeting of the Swiss Institute of Particle Physics (CHIPP), Lausanne, 8 September 2008.

- L. Wilke: **Heavy Flavour Physics at CMS and ATLAS**
  Moriond QCD and High Energy Interactions 2009, La Thuile, 16 March 2009.

17.1.5 D0

Articles

- **Search for Higgs bosons decaying to tau pairs in ppbar collisions with the D0 detector**
  V. M. Abazov *et al.*, Phys. Rev. Lett. $\mathbf{101}$, 071804 (2008).

- **First study of the radiation-amplitude zero in Wgamma production and limits on anomalous WWgamma couplings at $\sqrt{s}$=1.96 TeV**
  V. M. Abazov *et al.*, Phys. Rev. Lett. $\mathbf{100}$, 241805 (2008).

- **Evidence for production of single top quarks**
  V. M. Abazov *et al.*, Phys. Rev. D $\mathbf{78}$, 012005 (2008).

- **Search for decay of a fermiophobic Higgs boson $h_f \to \gamma\gamma$ with the D0 detector at $\sqrt{s} = 1.96$ TeV**
  V. M. Abazov *et al.*, Phys. Rev. Lett. $\mathbf{101}$, 051801 (2008).

- **Search for pair production of doubly-charged Higgs bosons in the $H^{++}H^{--} \to \mu^+\mu^+\mu^-\mu^-$ final state at D0**
  V. M. Abazov *et al.*, Phys. Rev. Lett. $\mathbf{101}$, 071803 (2008).

- **Search for large extra dimensions in the mono-photon final state at sqrt(s) = 1.96 TeV**
  V. M. Abazov *et al.*, Phys. Rev. Lett. $\mathbf{101}$, 011601 (2008).

- **Measurement of the ratio of the $p\bar{p} \to W$+c-jet cross section to the inclusive $p\bar{p} \to W$+jets cross section**
  V. M. Abazov *et al.*, Phys. Lett. B $\mathbf{666}$, 23 (2008).

- **Search for scalar top quarks in the acoplanar charm jets and missing transverse energy final state in $p\bar{p}$ collisions at $\sqrt{s} = 1.96$ TeV**
  V. M. Abazov *et al.*, Phys. Lett. B $\mathbf{665}$, 1 (2008).

- **Measurement of the ttbar production cross section in ppbar collisions at sqrts = 1.96 TeV**
  V. M. Abazov *et al.*, Phys. Rev. Lett. $\mathbf{100}$, 192004 (2008).

- **Search for W-prime boson resonances decaying to a top quark and a bottom quark**
  V. M. Abazov *et al.*, Phys. Rev. Lett. $\mathbf{100}$, 211803 (2008).

- **Search for squarks and gluinos in events with jets and missing transverse energy using 2.1 fb-1 of ppbar collision data at $\sqrt{s}$=1.96 TeV**
  V. M. Abazov *et al.*, Phys. Lett. B $\mathbf{660}$, 449 (2008).

PhD thesis

- **Search for the Rare Decays $B^\pm \to K^\pm\mu^+\mu^-$ and $B_d^0 \to K^*\mu^+\mu^-$ with the D0 Experiment**
  Andreas Wenger, PhD thesis, Universität Zürich, Dezember 2008.

17.1.6 DIRAC

Articles

- **A new aerogel Cherenkov detector for DIRAC-II**
  Y. Allkofer *et al.*, Nucl. Instrum. Meth. in Phys. Research **A 595** (2008) 84.
- **The C_4F_{10} Cherenkov detector for DIRAC-II**
  S. Horikawa *et al.*, Nucl. Instrum. Meth. in Phys. Research **A 595** (2008) 212.
- **Evidence for πK-atoms with DIRAC**
  B. Adeva *et al.*, Physics Letters **B 674** (2009) 11.
- **Search for πK-atoms with DIRAC II**
  Y. Allkofer *et al.*, Proc. XII Int. Conf. on Hadron Spectroscopy, Physics Series, Vol. **XLVI** (2008) 883.

Article in press

- **Observation of πK-atoms with DIRAC-II**
  Y. Allkofer, Int. conf. on exotic atoms and related topics (EXA08), Vienna, 2008.

PhD thesis

- **Search for πK-atoms with DIRAC**
  Y. Allkofer, Inaugural Dissertation, Universität Zürich, 2008.

Invited Lecture

- **Observation of πK-atoms with DIRAC-II**
  Y. Allkofer, Int. conf. on exotic atoms and related topics (EXA08), Vienna, 2008.

17.1.7 GERDA

Invited lectures and conference contributions

- L. Baudis: **The GERDA Experiment**
  Third CHIPP Swiss Neutrino Workshop, ETH Zurich, November 17 2008.
- L. Baudis: **Suche nach dem neutrinolosen Doppelbetazerfall und das GERDA Experiment am Gran Sasso Untergrundlabor**
  Physikalische Gesellschaft Zürich, April 10 2008.
- F. Froborg: **The GERDA Experiment**
  CHIPP Planery Meeting, Lausanne, September 5 2008.

- F. Froborg: **The Calibration System for the GERDA Experiment**
  ISAPP 2008, Valencia, July 19 2008.

17.1.8 H1

Articles

- **A General Search for New Phenomena at HERA**
  F. D. Aaron *et al.*, Phys. Lett. B **674** (2009) 257.
- **Study of Charm Fragmentation into $D^{\pm}$ Mesons in Deep-Inelastic Scattering at HERA**
  F. D. Aaron *et al.*, Eur. Phys. J. C **59** (2009) 589.
- **Inclusive Photoproduction of ρ^0, K^0 and ϕ Mesons at HERA**
  F. D. Aaron *et al.*, Phys. Lett. B **673** (2009) 119.
- **Measurement of Diffractive Scattering of Photons with Large Momentum Transfer at HERA**
  F. D. Aaron *et al.*, Phys. Lett. B **672** (2009) 219.
- **Multi-Lepton Production at High Transverse Momenta in ep Collisions at HERA**
  F. D. Aaron *et al.*, Phys. Lett. B **668** (2008) 268.
- **Measurement of the Proton Structure Function F_L at Low x**
  F. D. Aaron *et al.*, Phys. Lett. B **665** (2008) 139.
- **Search for Excited Electrons in ep Collisions at HERA**
  F. D. Aaron *et al.*, Phys. Lett. B **666** (2008) 131.
- **A Search for Excited Neutrinos in e-p Collisions at HERA**
  F. D. Aaron *et al.*, Phys. Lett. B **663**, 382 (2008).

Articles in press

- **Events with Isolated Leptons and Missing Transverse Momentum and Measurement of W Production at HERA**
  F. D. Aaron *et al.*, arXiv:0901.0488 (hep-ex).
- **Strangeness Production at low Q^2 in Deep-Inelastic ep Scattering at HERA**
  F. D. Aaron *et al.*, arXiv:0810.4036 (hep-ex).

Bachelor thesis

- **Identification of isolated photons at high energies at H1**
  Arno Gadola, Bachelor thesis, Universität Zürich, März 2008.

Conference contribution

- **Prompt Photon Production in Photoproduction at HERA**
  K. Nowak, XVI International Workshop on Deep-Inelastic Scattering and Related Subjects, University College London, April 7-11, 2008.

17.1.9 LHCb

Article

- **The LHCb Detector at the LHC**
  A. A. Alves *et al.*, JINST **3**, S08005 (2008).

Conference contributions and invited talks

- **Electroweak physics at LHCb**
  Jonathan Anderson, Seminar at the School of Physics, University College Dublin, November 18, 2008.
- **The LHCb Silicon Tracker: lessons learned (so far)**
  A. Vollhardt, Topical Workshop on Electronics for Particle Physics (TWEPP), Naxos (Greece), September 2008.

LHCb notes

- **Production, Commissioning and First Data of the LHCb Silicon Tracker**
  H. Voss *et al.*, CERN-LHCb-2008-062.
- **TT detector description and implementation of the survey measurements**
  C. Salzmann and J. Van Tilburg, CERN-LHCb-2008-061.
- **The LHCb Silicon Tracker: lessons learned (so far)**
  A. Vollhardt, CERN-LHCb-2008-049.

17.1.10 Ultracold neutrons

Articles

- **Neutron velocity distribution from a superthermal solid 2H2 ultracold neutron source**
  I. Altarev *et al.*, Eur. Phys. J. A 37, 922614 (2008).
- **Storage of ultracold neutrons in high resistivity, non-magnetic materials with high Fermi potential**
  K. Bodek *et al.*, Nuclear Instruments and Methods in Physics Research A 597, 222226226 (2008).

PhD thesis

- **Production, Characterization and Reflectivity Measurements of Diamond-like Carbon and other Ultracold Neutron Guide Materials**
  Stefan Heule, PhD thesis, Universität Zürich, Juni 2008.

Conference contributions and invited talks

- **Direct Experimental Limit on Neutron → Mirror Neutron Oscillations**
  A. Knecht, International Workshop on Particle Physics with Slow Neutrons, 31. May 2008, Grenoble. Talk and Poster.

17.1.11 XENON

Articles

- **First Results from the XENON10 Dark Matter Experiment at the Gran Sasso National Laboratory**
  XENON Collaboration, Phys. Rev. Lett. 100, 021303 (2008).

- **New measurement of the relative scintillation efficiency of xenon nuclear recoils below 10 keV**
  E. Aprile, L. Baudis, B. Choi *et al.*, Phys. Rev. C 79, 045807 (2009).

- **Determination of the scintillation and ionization yield of liquid Xe from the XENON10 experiment**
  XENON10 Collaboration, Nucl. Inst. and Meth. A 601, 339 (2009).

- **Limits on the Spin-Dependent WIMP-nucleon Cross Section from the XENON10 Experiment**
  XENON10 Collaboration, Phys. Rev. Lett. 101, 091301 (2008).

Invited lectures and conference contributions

- L. Baudis: **Cold Dark Matter Searches with XENON**
  ETH/UZH Physics Colloquium, Zurich, December 10 2008.

- L. Baudis: **Backgrounds and Sensitivity Expectations for XENON100 Identification of Dark Matter**
  IDM08, Stockholm, August 19 2008.

- L. Baudis: **Dark Matter Searches with Liquid Xenon Experiments**
  Physics colloquium, Max Planck Institute for Nuclear Physics Heidelberg, July 16 2008.

- L. Baudis: **Cold Dark Matter Searches with XENON**
  CERN joint PP/EP seminar, October 27 2008.

- L. Baudis: **Cold Dark Matter Searches and the XENON Experiment**
  DESY seminar, June 17 2008.

- R. Santorelli: **Calibration of the Xenon100 detector**
  Dark Matter at the crossroads, DESY, Hamburg, October 1 2008.

- R. Santorelli: **The XENON Dark Matter Project**
  Rencontres de Moriond EW 2008, La Thuile, March 6 2008.

- A.D. Ferella: **Material screening and background expectation for the Xenon100 experiment**
  Dark Matter at the crossroads, DESY, Hamburg, October 1 2008.

- A. Manalaysay: **R&D of Liquid Xenon TPCs for Dark Matter Searches**
  CHIPP 2008 Workshop on Detector R&D, Geneva, June 12 2008.

- M. Haffke: **Untergrundstudien für das Xenon 1t-Projekt**
  DPG, LMU Munich, Germany, March 9 2009.

17.1.12 Miscellaneous

Reviews

- **Review of Particle Physics**
  C. Amsler *et al.* (Particle Data Group), Physics Letters $\mathbf{B}$ $\mathbf{667}$ (2008) 1.

- **2008 Particle Physics Booklet**
  C. Amsler *et al.* (Particle Data Group), Special issue printed by Elsevier.

- **Flavor physics of leptons and dipole moments**
  M. Raidal and A. van der Schaaf *et al.*, Eur. Phys. J. C (2008) 57: 13-182.

Articles

- **The** $\eta(1405)$**,** $\eta(1475)$**,** $f_1(1420)$**, and** $f_1(1510)$
  C. Amsler and A. Masoni, Phys. Lett. $\mathbf{B}$ $\mathbf{667}$ (2008) 641.

- **Note on scalar mesons**
  N.A. Törnqvist, S. Spanier and C. Amsler, Phys. Lett. $\mathbf{B}$ $\mathbf{667}$ (2008) 594.

- **Quark Model**
  C. Amsler, T. DeGrand and B. Krusche, Phys. Lett. $\mathbf{B}$ $\mathbf{667}$ (2008) 172.

- **Low energy tracking and particles identification in the MUNU Time Projection Chamber at 1 bar: possible application in low energy solar neutrino spectroscopy**
  Z. Daraktchieva *et al.* (MUNU Collaboration), J. Phys. G: Nucl. Part. Phys. $\mathbf{35}$ (2008) 125107.

- **Dark Matter Disc Enhanced Neutrino Fluxes from the Sun and Earth**
  T. Bruch, A. Peter, J. Read, L. Baudis and G. Lake, Physics Letters B 674, 250-256 (2009).

- **Detecting the Milky Way's Dark Disk**
  T. Bruch, J. Read, L. Baudis and G. Lake, Astrophysical Journal 696, 920-923 (2009).

- **Kaluza-Klein Dark Matter: Direct Detection vis-a-vis LHC**
  S. Arrenberg, L. Baudis, K. Kong, K.T. Matchev and J. Yoo, Phys. Rev. D78, 056002 (2008).

Talks

- C. Amsler: **From Antihydrogen to Dark Matter, Experimental Challenges**
  Physik-Kolloquium, Universität Basel, 20 February 2009.
- A. van der Schaaf: $\mu \to 3e$ **and muon EDM 5000 times better?**
  Meeting of the Swiss Institute of Particle Physics (CHIPP), Lausanne, 8 September 2008.
- A. van der Schaaf: **Prospects of a** $\mu \to 3e$ **search at** 10^{-16}
  3rd CHIPP Swiss neutrino workshop, ETH Zürich, 17.-18. November 2008.
- U. Straumann: **CHIPP and Swiss Particle Physics**
  R-ECFA visit in Switzerland, EPF Lausanne, 6 March 2009.
- A. Büchler: **PhD student point of view**
  R-ECFA visit in Switzerland, EPF Lausanne, 6 March 2009.
- L. Baudis: **Direct Dark Matter Searches: An Overview**
  New Horizons for Modern Cosmology, Dark Matter Conference, Galileo Galilei Institute, Florence, February 9 2009.
- L. Baudis: **Status of Direct Experimental Searches for Dark Matter**
  ENTApP Dark Matter Workshop, CERN, February 3 2009.
- L. Baudis: **Searching for Cold Dark Matter Signatures in the Milky Way**
  EPFL seminar, Lausanne, December 1 2008.
- L. Baudis: **Direct WIMP Searches**
  Dark Matter at the Crossroads, DESY, Hamburg, October 1 2008.
- L. Baudis: **Results and Prospects of Direct Dark Matter Detection**
  CHIPP Plenary Meeting, Lausanne, September 9 2008.
- L. Baudis: **Cold Dark Matter Searches with the CDMS and XENON Experiments**
  Physics colloquium, University of Bielefeld, June 30 2008.
- L. Baudis: **Experimental Dark Matter Searches: an Overview**
  APP UK 2008 Conference, June 20 2008.
- L. Baudis: **Dark Matter Searches with Liquid Noble Gases**
  E15 seminar, TU Munich, June 4 2008.
- L. Baudis: **Direct Detection of Cold Dark Matter**
  Physics Colloquium, Paul Scherrer Institute, April 24 2008.
- S. Arrenberg: **Die dunkle Seite des Universums**
  Nacht der Forschung "Forschende im Gespräch", Zürich, September 26 2008.
- T. Bruch: **Signatures of the Milky Way's Dark Disk in Current and Future Experiments**
  IDM 2008, Stockholm, August 18 2008.

- S. Arrenberg: **Kaluza-Klein Dark Matter - Direct Detection vis-a-vis LHC**
  IDM 2008, Stockholm, August 18 2008.

- M. Haffke: **Dark Matter Searches**
  Teilchenphysik Seminar, University of Bonn, Bonn, July 17 2008.

Master thesis

- **A fast online and triggerless signal reconstruction based on cross-correlation**
  Arno Gadola, Master thesis, Universität Zürich, January 2009.

17.2 Condensed matter

17.2.1 Superconductivity and Magnetism

Articles

- **Nodeless superconductivity in the infinite-layer electron-doped cuprate superconductor $Sr_{0.9}La_{0.1}CuO_2$**
  R. Khasanov, A. Shengelaya, A. Maisuradze, D. Di Castro, I.M. Savić, S. Weyeneth, M.S. Park, D.J. Jang, S.-I. Lee, and H. Keller, Phys. Rev. B **77**, 184512-1-6 (2008).

- **3D-xy critical properties of $YBa_2Cu_4O_8$ and magnetic-field-induced 3D to 1D crossover**
  S. Weyeneth, T. Schneider, Z. Bukowski, J. Karpinski, and H. Keller,
  J. Phys.: Condens. Matter **20**, 345210-1-4 (2008).

- **Single crystals of superconducting $SmFeAsO_{1-x}F_y$ grown at high pressure**
  N.D. Zhigadlo, S. Katrych, Z. Bukowski, S. Weyeneth, R. Puzniak, and J. Karpinski,
  J. Phys.: Condens. Matter **20**, 342202-1-5 (2008).

- **Evidence for competition between the superconducting and the pseudogap state in $(BiPb)_2(SrLa)_2CuO_{6+\delta}$ from muon-spin rotation experiments**
  R. Khasanov, Takeshi Kondo, S. Strässle, D.O.G. Heron, A. Kaminski, H. Keller, S.L. Lee, and Tsunehiro Takeuchi, Phys. Rev. Lett. **101**, 227002-1-4 (2008).

- **Lack of evidence for orbital-current effects in $Y_2Ba_4Cu_7O_{15-\delta}$ from ^{89}Y NMR**
  S. Strässle, J. Roos, M. Mali, T. Ohno, and H. Keller, Phys. Rev. Lett. **101**, 237001-1-4 (2008).

- **Weak High-Temperature Bulk Ferromagnetism in Mn-Doped $CdGeAs_2$ Semiconductors**
  V.G. Storchak, J.H. Brewer, D.G. Eshchenko, S.L. Stubbs, S.P. Cottrell, A.A. Nikonov, O.E. Parfenov and S.F. Marenkin, Chapter 2 in: Spintronics: Materials, Applications and Devices, Editors: G.C. Lombardi et al, pp. 49-58, Nova Science Pulblishers (2008).

- **Spatially resolved inhomogenious ferromagnetism in (Ga,Mn)As diluted magnetic semiconductors: A microscipic study by muon spin relaxation**
  V.G. Storchak, D.G. Eshchenko, E. Morenzoni, T. Prokscha, A. Suter, X. Liu and J.K. Furdina, Phys. Rev. Lett. **101**, 027202-1-4 (2008).

- **Muon-spin rotation measurements of the penetration depth of the Mo_3Sb_7 superconductor**
  R. Khasanov, P.W. Klamut, A. Shengelaya, Z. Bukowski, I.M. Savić, C. Baines, and H. Keller, Phys. Rev. B **78**, 014502-1-5 (2008).

- **Unconventional isotope effects, multi-component superconductivity and polaron formation in high temperature superconductors**
  A. Bussmann-Holder and H. Keller,
  Journal of Physics: Conference Series **108**, 012019-1-16 (2008).

- **Oxygen isotope effect on the superconducting transition and magnetic states within the phase diagram of $Y_{1-x}Pr_xBa_2Cu_3O_{7-\delta}$**
  R. Khasanov, A. Shengelaya, D. Di Castro, E. Morenzoni, A. Maisuradze, I.M. Savić, K. Conder, E. Pomjakushina, A. Bussmman-Holder, and H. Keller, Phys. Rev. Lett. **101**, 077001-1-4 (2008).

- **Detection of charge transfer processes in Cr-doped $SrTiO_3$ single crystals**
  F. La Mattina, J.G Bednorz, S.F. Alvarado, A. Shengelaya, and H. Keller,
  Appl. Phys. Lett. **93**, 022102-1-3 (2008).

- **Jahn-Teller physics and high-T_c superconductivity**
  H. Keller, A. Bussmann-Holder, and K.A. Müller, Materials Today **11**, 38-46 (2008).

- **Polaron coherence as origin of the pseudogap phase in high temperature superconducting cuprates**
  A. Bussmann-Holder, H. Keller, A.R. Bishop, A. Simon, and K.A. Müller,
  J. Supercond. Nov. Magn. **21**, 353-357 (2008).

- **Pressure effects on the magnetic transition temperature in ordered double perovskites**
  D. Di Castro, P. Dore, R. Khasanov, H. Keller, P. Mahadevan, Sugata Ray, D.D. Sarma, and P. Postorino, Phys. Rev. B **78**, 184416 (2008).

- **Superfluid density and angular dependence of the energy gap in optimally doped $(BiPb)_2(SrLa)_2CuO_{6+\delta}$**
  S. Strässle, R. Khasanov, T. Kondo, D.O.G. Heron, A. Kaminski, H. Keller, S.L. Lee, and T. Takeuchi, J. Supercond. Nov. Magn. **22**, 189-193 (2009).

- **Fermi Surface and Order Parameter Driven Vortex Lattice Structure Transitions in Twin-Free $YBa_2Cu_3O_7$**
  J.S. White, V. Hinkov, R.W. Heslop, R.J. Lycett, E.M. Forgan, C. Bowell, S. Strässle, A.B. Abrahamsen, M. Laver, C.D. Dewhurst, J. Kohlbrecher, J.L. Gavilano, J. Mesot, B. Keimer, and A. Erb, Phys. Rev. Lett. **102**, 097001-1-4 (2009).

- **Comparison of different methods for analyzing μSR line shapes in the vortex state of type-II superconductors**
  A. Maisuradze, R. Khasanov, A. Shengelaya, and H. Keller,
  J. Phys.: Condens. Matter **21**, 075701-1-15 (2009).

- **Probing the Yb^{3+} spin relaxation in $Y_{0.98}Yb_{0.02}Ba_2Cu_3O_x$ by electron paramagnetic resonance**
  A. Maisuradze, A. Shengelaya, B.I. Kochelaev, E. Pomjakushina, K. Conder, H. Keller, and K.A. Müller, Phys. Rev. B **79**, 054519-1-8 (2009).

- **Evidence for Polaron Formation in High-Temperature Superconducting Cuprates: Experiment and Theory**
  A. Bussmann-Holder and H. Keller, J. Supercond. Nov. Magn. **22**, 123-129 (2009).

- **Anisotropy of superconducting single crystal $SmFeAsO_{0.8}F_{0.2}$ studied by torque magnetometry**
  S. Weyeneth, R. Puzniak, U. Mosele, N.D. Zhigadlo, S. Katrych, Z. Bukowski, J. Karpinski, S. Kohout, J. Roos, and H. Keller, J. Supercond. Nov. Magn. **22**, 325-329 (2009).

- **Muon-spin rotation study of the ternary noncentrosymmetric superconductors $Li_2Pd_xPt_{3-x}B$**
  P.S. Häfliger, R. Khasanov, R. Lortz, A. Petrovic, K. Togano, C. Baines, B. Graneli, and H. Keller, J. Supercond. Nov. Magn. **22**, 337-342 (2009).

- **Evidence for two distinct anisotropies in the oxypnictide superconductors $SmFeAsO_{0.8}F_{0.2}$ and $NdFeAsO_{0.8}F_{0.2}$**
  S. Weyeneth, R. Puzniak, N.D. Zhigadlo, S. Katrych, Z. Bukowski, J. Karpinski, and H. Keller, J. Supercond. Nov. Magn. **22**, 347-351 (2009).

- **Superconductivity at 23 K and low anisotropy in Rb-substituted $BaFe_2As_2$ single crystals**
  Z. Bukowski, S. Weyeneth, R. Puzniak, P. Moll, S. Katrych, N.D. Zhigadlo, J. Karpinski, H. Keller, and B. Batlogg, Phys. Rev. B **79**, 104521-1-8 (2009).

- **Magnetism and superconductivity in cuprate heterostructures studied by Low Energy μSR**
  B.M. Wojek, E. Morenzoni, D.G. Eshchenko, A. Suter, T. Prokscha, E. Koller, E. Treboux, Ø. Fischer, and H. Keller, Physica B **404**, 720-723 (2009).

- **Near-surface muonium states in germanium**
  T. Prokscha, E. Morenzoni, D.G. Eshchenko, H. Luetkens, G.J. Nieuwenhuys, and A. Suter, Physica B **404**, 866-869 (2009).

- **Low energy muon studies of semiconductor interfaces**
  D.G. Eshchenko, V.G. Storchak, E. Morenzoni, T. Prokscha, A. Suter, X. Liu, and J.K. Furdyna, Physica B **404**, 873-875 (2009).

- **RF-μSR in electric field studies of GaP**
  D.G. Eshchenko, V.G. Storchak, and S.P Cottrell, Physica B **404**, 876-879 (2009).

- **Muon track induced current measurements in semi-insulating GaAs**
  D.G. Eshchenko, V.G. Storchak, and S.P Cottrell, Physica B **404**, 880-883 (2009).

- **Electron localization into magnetic polaron in EuS**
  V.G. Storchak, O.E. Parfenov, J.H. Brewer, P.L. Russo, S.L. Stubbs, R.L. Lichti, D.G. Eshchenko, E. Morenzoni, S.P. Cottrell, J.S. Lord, T.G. Aminov, V.P. Zlomanov, A.A.Vinokurov, R.L. Kallaher, and S. von Molnár, Physica B **404**, 896-898 (2009).

- **Novel muonium centers - magnetic polarons - in magnetic semiconductors**
  V.G. Storchak, O.E. Parfenov, J.H. Brewer, P.L. Russo, S.L. Stubbs, R.L. Lichti, D.G. Eshchenko, E. Morenzoni, V.P. Zlomanov, A.A. Vinokurov, and V.G. Bamburov, Physica B **404**, 899-902 (2009).

- **High-pressure muon spin rotation studies of magnetic semiconductors: EuS**
  D.G. Eshchenko, V.G. Storchak, E. Morenzoni, and D. Andreica, Physica B **404**, 903-905 (2009).

Articles in press

- **The microscopic study of a single hydrogen-like impurity in semi-insulating GaAs**
  D.G. Eshchenko, V.G. Storchak, S.P. Cottrell, and E. Morenzoni, cond-mat/0810.2692.

PhD theses

- **Investigation of cuprate superconductors by electron paramagnetic resonance (EPR) and muon-spin rotation (μSR)**
  A. Maisuradze, PhD thesis, Universität Zürich, 2008.

- **Insulator-to-metal transition and resistive switching in Cr-doped $SrTiO_3$**
  F. La Mattina, PhD thesis, Universität Zürich, 2008.

- **Investigations of the energy gaps in cuprate superconductors**
  S. Strässle, PhD thesis, Universität Zürich, 2009.

Master thesis

- **Realisierung eines Tieftemperatureinsatzes für hochsensitive Drehmomentmagnetometrie**
  U. Mosele, Master thesis, Universität Zürich, 2008.

Conference reports

- **Muon track induced current measurements in semi-insulating GaAs**
  D.G. Eshchenko, V.G. Storchak, and S.P Cottrell, μSR 2008 – 11^{th} International Conference on Muon Spin Rotation, Relaxation, & Resonance, Tsukuba, Japan, July 21-25, 2008.

- **RF-μSR in electric field studies of GaP**
  D.G. Eshchenko, V.G. Storchak, and S.P Cottrell, μSR 2008 – 11^{th} International Conference on Muon Spin Rotation, Relaxation, & Resonance, Tsukuba, Japan, July 21-25, 2008.

- **Low Energy Muon studies of semiconductor interfaces**
  D.G. Eshchenko, V.G. Storchak, E. Morenzoni, T. Prokscha, A. Suter, X. Liu, and J.K. Furdyna, μSR 2008 – 11^{th} International Conference on Muon Spin Rotation, Relaxation, & Resonance, Tsukuba, Japan, July 21-25, 2008.

- **High-pressure Muon Spin Rotation studies of magnetic semiconductors: EuS**
  D.G. Eshchenko, V.G. Storchak, E. Morenzoni, and D. Andreica, μSR 2008 – 11^{th} International Conference on Muon Spin Rotation, Relaxation, & Resonance, Tsukuba, Japan, July 21-25, 2008.

- **Magnetism and superconductivity in cuprate heterostructures studied by Low Energy μSR**
  B.M. Wojek, E. Morenzoni, D.G. Eshchenko, T. Prokscha, A. Suter, E. Koller, E. Treboux, Ø. Fischer, and H. Keller, μSR 2008 – 11^{th} International Conference on Muon Spin Rotation, Relaxation, & Resonance, Tsukuba, Japan, July 21-25, 2008.

- **Magnetism and superconductivity in cuprate heterostructures studied by Low Energy μSR**
  B.M. Wojek, E. Morenzoni, D.G. Eshchenko, A. Suter, T. Prokscha, E. Koller, E. Treboux, Ø. Fischer, and H. Keller, 7th PSI Summer School on Condensed Matter Research, Zuoz, August 16-22, 2008.

- **Search for orbital-ourrent effects in $Y_2Ba_4Cu_7O_{15-\delta}$ using ^{89}Y NMR**
  S. Strässle, J. Roos, M. Mali, T. Ohno, and H. Keller, March Meeting of the American Physical Society, Pittsburgh, March 16-20, 2009.

- **Temperature dependent anisotropy of oxypnictide superconductors studied by torque magnetometry**
  S. Weyeneth, R. Puzniak, N.D. Zhigadlo, S. Katrych, Z. Bukowski, J. Karpinski, U. Mosele, S. Kohout, J. Roos, and H. Keller, March Meeting of the American Physical Society, Pittsburgh, March 16-20, 2009.

Invited lectures

- H. Keller: **Universal correlations of unconventional isotope effects in cuprate superconductors**
  CoMePhS Meeting Rome, University of Rome *La Sapienza*, Rome, Italy, April 9-11, 2008.
- H. Keller: **Unconventional isotope effects and multi-component superconductivity in cuprates**
  6^{th} International Conference of the Stripes Series, Stripes 08, Quantum Phenomena in Complex Matter, Erice (Sicily), Italy, July 26 - August 1, 2008.
- H. Keller: **Unconventional Isotope effects in cuprate superconductors**
  22^{nd} General Conference of the Condensed Matter Division of the European Physical Society, University of Rome *La Sapienza*, Rome, Italy, August 25-29, 2008.
- H. Keller: **Unconventional isotope effects and multi-component superconductivity in cuprates**
  Second CoMePhS Workshop in Controlling Phase Separation in Electronic Systems, Nafplion, Greece, September 30 - October 4, 2008.
- S. Weyeneth: **Temperature dependent anisotropy of $SmFeAsO_{1-x}F_y$ single crystals studied by torque magnetometry**
  International Workshop on Iron-(Nickel)-Based Superconductors, The Institute of Physics, Chinese Academy of Sciences, Beijing, China, October 19, 2008.
- H. Keller: **Unconventional isotope effects and multi-component superconductivity in cuprate high-temperature superconductors**
  University of Augsburg, Augsburg, Germany, December 16, 2008.
- H. Keller: **Isotope effects and multi-band superconductivity in high-temperature superconductors**
  SMEC 2009 Conference, Study of Matter at Extreme Conditions, Miami - Western Caribbean, U.S.A., March 28 - April 2, 2009.

17.2.2 Phase transitions and superconducting photon detectors

Articles

- **$LaBaNiO_4$: A Fermi glass**
  A. Schilling, R. Dell'Amore, J. Karpinski, Z. Bukowski, M. Medarde, E. Pomjakushina and K. A. Müller, J. Phys.: Condens. Matter, **21**, (2009) 015701.
- **$U(1)$ symmetry breaking and violated axial symmetry in $TlCuCl_3$ and other insulating spin systems**
  R. Dell'Amore, A. Schilling and K. Krämer, Phys. Rev. B, **79**, (2009) 014438.

- **Synthesis and Characterization of Hybrid Materials derived from Polyaniline and Lacunary Keggin-type Polyoxotungstates**
  E. F.C. Chimamkpam, F. Hussain, A. Engel, A. Schilling and G. R. Patzke, ZAAC, **635**, (2009) 624.

- **Intrinsic Quantum Efficiency and Electro-Thermal Model of a Superconducting Nanowire Single-Photon Detector**
  A. Semenov, P. Haas, H.-W. Hübers, K. Il'in, M. Siegel, A. Kirste, D. Drung, T. Schurig and A. Engel, J. Mod. Optics, **56**, (2009) 345.

- **Magnetic Vortices in Superconducting Photon Detectors**
  A. Engel, H. Bartolf, A. Schilling, A. Semenov, H.-W. Hübers, K. Il'in and M. Siegel, J. Mod. Optics, **56**, (2009) 352.

- **Multi-project wafer scale process for productive research and development**
  H. Bartolf, A. Engel, L. Gómez and A. Schilling, Raith Application Note 2008, Raith GmbH.

- **Fraction of Bose-Einstein condensed triplons in $TlCuCl_3$ from magnetization data**
  R. Dell'Amore, A. Schilling and K. Krämer, Phys. Rev. B, **78**, (2008) 224403.

- **Differential-thermal analysis around and below the critical temperature T_c of various low-T_c superconductors: A comparative study**
  M. Reibelt, A. Schilling, P. C. Canfield, G. Ravikumar and H. Berger, Physica C, **468**, (2008) 2254.

- **Vortex-based single-photon response in nanostructured superconducting detectors**
  A. D. Semenov, P. Haas, H.-W. Hübers, K. Il'in, M. Siegel, A. Kirste, T. Schurig and A. Engel, Physica C, **468**, (2008) 627.

- **Fabrication of metallic structures with lateral dimensions less than 15 nm and $j_c(T)$-measurements in NbN micro- and nanobridges**
  H. Bartolf, A. Engel, A. Schilling, K. Il'lin, M. Siegel, Physic C, **468**, (2008) 793.

- **Current-Induced Critical State in NbN Thin-Film Structures**
  K. Il'in, M. Siegel, A. Engel, H. Bartolf, A. Schilling, A. Semenov, H.-W. Hübers, J. Low Temp. Phys., **151**, (2008) 585.

PhD thesis

- **Bose-Einstein condensation in the quantum spin-system $TlCuCl_3$: Any sign of "magnetic superfluidity"?**
  Raffaele Dell'Amore, PhD thesis, Physik-Institut Universität Zürich, 2008.

Contributed Conference Presentations

- **Fabrication of superconducting single-photon detectors (poster)**
  H. Bartolf, L. Gómez, A. Engel, A. Schilling, International Conference on Nanostructured Materials (NANO 2008), Rio de Janeiro, Brazil, 1.-6.6.2008.

Invited Lectures

- **Josephson junction arrays for THz radiation detection**
  L. Gómez, Conference on Quantum Metrology 2008 (QM2008), Pozna n, Poland, 5.5.2008.
- **Superconducting Nanostructures & Single-Photon Detector**
  A. Engel, Manep Project 5 Internal Workshop 2008, Neuchâtel, Switzerland, 23.1.2009.

17.2.3 Surface Physics

Articles

- **Comparative electron diffraction study of the diamond nucleation layer on Ir(001)**
  S. Gsell, S. Berner, T. Brugger, M. Schreck, R. Brescia, M. Fischer, J. Osterwalder, B. Stritzker, Diamond Relat. Mater.17, 1029-1034 (2008).
- **Quantitative vectorial spin analysis in ARPES: Bi/Ag(111) and Pb/Ag(111)**
  F. Meier, J. H. Dil, J. Lobo-Checa, L. Patthey, J. Osterwalder, Phys. Rev. B 77, 165431:1-7 (2008).
- **Charge-transfer dynamics in one-dimensional C_{60} chains**
  V. Pérez-Dieste, A. Tamai, T. Greber, S. G. Chiuzbaian, L. Patthey, Surf. Sci. 602, 1928-1932 (2008).
- **Living on the edge: a nanographene molecule adsorbed across gold step edges**
  M. Treier, P. Ruffieux, R. Schillinger, T. Greber, K. Müllen, R. Fasel, Surf. Sci. Lett. 602, L84-L88 (2008).
- **Exchange-split interface state at h-BN/Ni(111)**
  K. Zumbrägel, K. Wulff, Ch. Eibl, M. Donath, M. Hengsberger, Phys. Rev. B 78, 085422:1-7 (2008).
- **Graphene on Ru(0001): a 25 x 25 supercell**
  D. Martoccia, P. R. Willmott, T. Brugger, M. Björk, S. Günther, C. M. Schlepütz, A. Cervellino, S. A. Pauli, B. D. Patterson, S. Marchini, J. Wintterlin, W. Moritz, T. Greber, Phys. Rev. Lett. 101, 126102:1-4 (2008).
- **Direct observation of space charge dynamics by picosecond low-energy electron scattering**
  C. Cirelli, M. Hengsberger, A. Dolocan, H. Over, J. Osterwalder, T. Greber, Europhys. Lett. 85, 17010:1-5 (2008).
- **Growth of twin-free heteroepitaxial diamond on Ir/YSZ/Si(111)**
  M. Fischer, R. Brescia, S. Gsell, M. Schreck, T. Brugger, T. Greber, J. Osterwalder, B. Stritzker, J. Appl. Phys. 104, 123531:1-5 (2008).
- **Rashba-type spin-orbit splitting of quantum well states in ultrathin Pb films**
  J. H. Dil, F. Meier, J. Lobo-Checa, L. Patthey, G. Bihlmayer, J. Osterwalder, Phys. Rev. Letters 101, 266802: 1-4 (2008).
- **Comparison of electronic structure and template function of single-layer graphene and a hexagonal boron nitride nanomesh on Ru(0001)**
  T. Brugger, S. Günther, B. Wang, J. H. Dil, M.-L. Bocquet, J. Osterwalder, J. Wintterlin, T. Greber, Phys. Rev. B 79, 045407:1-6 (2009).

- **Observation of unconventional quantum spin textures in topological insulators**
  D. Hsieh, Y. Xia, L. Wray, D. Qian, A. Pal, J. H. Dil, J. Osterwalder, F. Meier, G. Bihlmayer, C. L. Kane, Y. S. Hor, R. J. Cava, M. Z. Hasan, Science 323, 919-922 (2009).

- **Nondegenerate metallic states on Bi(114): a one-dimensional topological metal**
  J. W. Wells, J. H. Dil, F. Meier, J. Lobo-Checa, V. N. Petrov, J. Osterwalder, M. M. Ugeda, I. Fernandez-Torrente, J. I. Pascual, E. D. L. Rienks, M. F. Jensen, Ph. Hofmann, Phys. Rev. Lett. 102, 096802:1-4 (2009).

- **Two- and three-dimensional band structure of ultrathin Ni on Cu(001)**
  M. Hoesch, V. N. Petrov, M. Muntwiler, M. Hengsberger, J. Lobo-Checa, T. Greber, J. Osterwalder, Phys. Rev. B 79, 155404:1-10 (2009).

Article in press

- **Fermi surfaces of single-layer dielectrics on transition metals**
  T. Greber, M. Corso, J. Osterwalder, Surf. Sci., doi:10.1016/j.susc.2008.08.043.

Master theses

- **Two-photon photoemission from tetramantane monolayers**
  Silvan Roth, Master thesis, Physik-Institut, Universität Zürich, 2008.

- **Lumineszenz von h-BN Nanomesh**
  Jeanette Schmidlin, Master thesis, Physik-Institut, Universität Zürich, 2008.

PhD thesis

- **Novel approaches to the bottom-up fabrication of ordered organic nanostructures on metal surfaces**
  Matthias Treier, PhD thesis, Physik-Institut, Universität Zürich, 2008. (work carried out at EMPA, Thun).

Contributed conference presentations

- **Time-resolved photoelectron spectroscopy from solid surfaces**
  M. Hengsberger, pre-NCCR Strategy Meeting "Ultrafast Phenomena in Nature", Bern, 03.06.08.

- **Measuring the nanoscale electrostatic potential landscape with PAX**
  J. H. Dil, 3rd Swiss Molecules on Surfaces (molCHsurf-III) Discussion Meeting, Bern, 10.06.08.

- **Growth of Co clusters on the nanomesh and their characterization**
  T. Brugger, EU-STREP NanoMesh Final Meeting, Orscholz, Germany, 23.06.08.

- **Understanding and tuning the electron spin on surfaces: Bi/Ag(111)**
  F. Meier, SLS Symposium on Surface Science, PSI, 01.07.08.

- **Time-resolved 2PPE studies on a ferromagnetic h-BN/Ni(111) surface (Poster)**
  D. Leuenberger, International Conference on Ultrafast Surface Dynamics (USD-6), Kloster Banz, Germany, 24.07.08.

- **Ar@C_{60} - a photoemission study on a noble gas endofullerene**
  M. Morscher, European Conference on Surface Science 2008, Liverpool, UK, 27.07.08.
- **Initial-state effects on electron transition probability in the phonon scattering process**
  H. Yanagisawa, European Conference on Surface Science 2008, Liverpool, UK, 28.07.08.
- **Rashba-type spin-orbit splitting in quantum well states in thin Pb films**
  J. H. Dil, European Conference on Surface Science 2008, Liverpool, UK, 28.07.08.
- **Understanding and tuning the electron spin on surfaces**
  F. Meier, European Conference on Surface Science 2008, Liverpool, UK, 30.07.08.
- **Is graphene on Ru(0001) a nanomesh ?**
  T. Brugger, European Conference on Surface Science 2008, Liverpool, UK, 31.07.08.
- **Two-photon photoemission experiments on tetramantane monolayers**
  S. Roth, 19th European Conference on Diamond, Diamond-like Materials, Carbon Nanotubes and Nitrides, Sitges, Spain, 10.09.08.
- **Explanation of the Rashba effect at surfaces through quantum well states in ultrathin Pb films**
  J. H. Dil, SLS Workshop on the Spectroscopy of Novel Materials, Rigi, 19.01.09.
- **Fermi surface spin textures of mixed surface alloys: BiPbSb/Ag(111)**
  F. Meier, SLS Workshop on the Spectroscopy of Novel Materials, Rigi, 19.01.09.
- **Asymmetric electron emission from a tungsten tip apex due to surface plasmon polaritons excited by laser pulses**
  H. Yanagisawa, Symposium on Surface and Nano Science (SSNS-09), Shizukuishi, Japan, 29.01.09.
- **Magnetism in the Ni(111) surface**
  T. Greber, 24th Workshop on Novel Materials and Superconductors, Planneralm, Austria, 21.02.09.
- **Non-magnetic spin structures in ultrathin Pb films**
  J. H. Dil, SLS Symposium on Magnetism in Reduced Dimensions, PSI, 03.03.09.
- **Rashba-type spin-orbit splitting of quantum well states in ultrathin Pb films (Poster)**
  J. H. Dil, Symposium on Surface Science (3S'09), St. Moritz, 12.03.09.
- **Fermi surface of graphene on Ru(0001)**
  T. Brugger, March Meeting of the American Physical Society, Pttsburgh, PA, USA, 16.03.09.
- **Unconventional Fermi surface spin textures in the Bi-Pb-Sb/Ag(111) surface alloy**
  F. Meier, Frühjahrstagung der Deutschen Physikalischen Gesellschaft, Dresden, 26.03.09.
- **Rashba-type spin-orbit splitting in quantum well states in ultrathin Pb films**
  J. H. Dil, Frühjahrstagung der Deutschen Physikalischen Gesellschaft, Dresden, 26.03.09.

Invited lectures

- T. Greber: **Near-node photoelectron holography**
  SLS Symposium on Diffraction and Phase Retrieval, PSI, 01.04.08.

- J. H. Dil: **Influence of the interface on electron confinement in thin metal films**
  Seminar, Physics Department, EPFL, Lausanne, 11.04.08.

- J. Osterwalder: **Monolagen von hexagonalem Bornitrid: das isolierende Pendant zum Graphene**
  Physik-Kolloquium, Universität Kaiserslautern, Germany, 16.06.08.

- M. Hengsberger: **Time-resolved photoelectron spectroscopy from ferromagnetic surfaces**
  XI-th Symposium on Surface Physics, Prague, Czech Republic, 01.07.08.

- T. Greber: **Nanomesh: yesterday, today and in the future**
  EU-STREP NanoMesh Final Meeting, Orscholz, Germany, 23.06.08.

- T. Greber: **Single sheets of boron nitride sp^2 networks: from flat layers to nanomesh**
  International Workshop on Nanomaterials and Nanodevices, Chinese Academy of Sciences Session, Beijing, China, 02.07.08.

- T. Greber: **The conformation matters: from molecular chains and switches to chiral recognition**
  International Workshop on Nanomaterials and Nanodevices, Kunming Session, Kunming, China, 05.07.08.

- T. Greber: **Surface trapping of atoms and molecules with dipole rings**
  Seminar, Key Laboratory of Metastable Science and Technology, Qinhuandao, China, 18.07.08.

- J. Osterwalder: **Hexagonal boron nitride layers as templates for molecular organization**
  MONET and iNANO PhD School "Molecular Organization and Function on Surfaces", Aarhus, Denmark, 11.09.08.

- T. Greber: **See them, and see them move: towards time resolved electron scattering**
  Workshop on Surface Diffraction and Spectroscopic Methods for Nanoscience, Trieste, Italy, 03.10.08.

- J. Osterwalder: **Quantitative three-dimensional spin polarimetry in ARPES**
  55th Meeting of the American Vacuum Society, Boston, MA, USA, 22.10.08.

- T. Greber: **Single-layer dielectrics**
  Rencontre Nationale Matière Condensée et Modélisation des Systèmes (MCMS 2008), Fès, Morocco, 27.10.08.

- T. Greber: **Boron nitride nanomesh: a robust template for molecule and cluster arrays**
  56th IUVSTA Workshop on Template Mediated Growth of Nanostructures, Schlaining, Austria, 03.11.08.

- T. Greber: **Trapping molecules on graphene and hexagonal boron nitride single layers**
  Seminar, Sandoghdar Group, Physical Chemistry Department, ETH Zürich, 21.11.08

- M. Hengsberger: **Time-resolved photoemission from h-BN/Ni(111)**
  Seminar, Max-Planck-Institut für Mikrostrukturphysik, Halle, Germany, 23.10.08.

- T. Greber: **Production of h-BN single layers**
  Seminar, Hong Kong University of Science and Technology, China, 19.01.08.

- M. Hengsberger: **Time- (and angle-) resolved (two-photon) photoelectron spectroscopy**
  SLS Workshop on the Spectroscopy of Novel Materials, Rigi, 20.01.09.

- M. Hengsberger: **Two-photon photoemission experiments from diamondoid monolayers**
  Seminar, Institut für Festkörperphysik, Forschungszentrum Karlsruhe, Germany, 29.01.09.
- T. Greber: **Corrugated sp^2 hybridized layer templates for molecules**
  Symposium on Surface and Nano Science (SSNS-09), Shizukuishi, Japan, 29.01.09.
- T. Greber: **Absolute determination of molecular conformation by angle-scanned photoelectron diffraction (XPD)**
  Seminar, Institute of Solid State Physics ISSP, University of Tokyo, Japan, 05.02.09.
- M. Hengsberger: **Crazy idea or scientific case ? - time-resolved photoelectron spectroscopy at x-ray energies using a time-of-flight spectrometer with spin filter**
  PSI-XFEL Workshop on Crazy Ideas and Challenges, PSI, 27.02.09.
- J. Osterwalder: **Photoelectrons and materials properties**
  Symposium "Headways in Materials Science", EMPA Dübendorf, 06.03.09.
- J. H. Dil: **Time-, spin-, space- and angle-resolved photoemission on correlated materials**
  PSI-XFEL Workshop on Correlated Systems, Universität Zürich, 06.03.09.
- J. Osterwalder: **Measuring spin polarization vectors in ARPES**
  Hauptvortrag, Frühjahrstagung der Deutschen Physikalischen Gesellschaft, Dresden, 26.03.09.

17.2.4 Physics of Biological systems

Article in press

- **Simultaneous reconstruction of phase and amplitude contrast from a single holographic record**
  T. Latychevskaia and H.-W. Fink, Optics Express.

Bachelor and Master theses

- **Gepulste Elektronenholographie**
  Matthias Germann, Master thesis.
- **Die Bindungsenergie von Wasser an DNA**
  Flavio Lanfranconi, Bachelorarbeit.
- **Messung der Temperaturabhängigkeit der Desorptionsrate von Schwerwasser auf verschiedenen Substraten mittels Thermodesorptionsspektroskopie**
  Fabian Hobrecker, Bachelorarbeit.
- **Optische Holographie einer geladenen Wolframspitze**
  Florian Schwarz, Bachelorarbeit.

PhD thesis

- **Quantification of the Gating Charge in K^+ and Na^+ Ion Channels by Use of eGFP Fluorescence**
  Dominik Grögler, PhD thesis.

Presentations

- **Vom Schattenbild zum Hologramm**
  Elvira Steinwand, Jean-Nicolas Longchamp, Florian Schwarz, Flavio Lanfranconi and Tatiana Latychevskaia, demonstrations and talks at the "Nacht der Forschung 2008", Zurich Lake, 26 September 2008.

- **Holography with Low Energy Electrons - a brief status report (master thesis of Matthias Germann)**
  Hans-Werner Fink, SIBMAR workshop, Brno, Czech Republic, 22-23 October 2008.

- **Hologram reconstruction and related issues**
  Tatiana Latychevskaia, SIBMAR workshop, Brno, Czech Republic, 22-23 October 2008.

- **Coherent Diffraction - oversampling - micron sized electron optical lenses**
  Elvira Steinwand and Jean-Nicolas Longchamp, SIBMAR workshop, Brno, Czech Republic, 22-23 October 2008.

- **DNA sample preparation issue discussion and update**
  Eugen Ermantraut, Heinz Gross, Conrad Escher and Hans-Werner Fink, SIBMAR workshop, Brno, Czech Republic, 22-23 October 2008.

- **Efforts towards Atomic Resolution in Low Energy Electron Holography**
  Matthias Germann, SIBMAR workshop in Lucerne, Switzerland, 26-29 January 2009.

- **Reconstruction of Low Energy Electron Holograms**
  Tatiana Latychevskaia, SIBMAR workshop in Lucerne, Switzerland, 26-29 January 2009.

- **Coherent Diffraction with Low Energy Electrons**
  Elvira Steinwand and Jean-Nicolas Longchamp, SIBMAR workshop in Lucerne, Switzerland, 26-29 January 2009.

- **Experiments with Individual DNA Molecules**
  Conrad Escher, SIBMAR workshop in Lucerne, Switzerland, 26-29 January 2009.

17.2.5 Physical Systems Biology and non-equilibrium Soft Matter

Articles

- **Conservation of energy in coherent backscattering at large angles**
  S. Fiebig, C.M. Aegerter, W. Bührer, M. Störzer, E. Akkermans, G. Montambaux, and G. Maret, Europhys. Lett. **81**, 64004 (2008).

- **Experimental study of the freely cooling granular gas**
  C.C. Maass, N. Isert, G. Maret, and C.M. Aegerter, Phys. Rev. Lett. **100** 248001 (2008).

- **Universal optimal transmission of light through disordered materials**
  I.M. Vellekoop and A.P. Mosk, Phys. Rev. Lett. **101**, 120601 (2008).

- **Spatial amplitude and phase modulation using commercial twisted nematic LCDs**
  E.G. van Putten, I.M. Vellekoop, and A.P. Mosk, Applied Optics **47**, 2076 (2008).

- **Phase control algorithms for focusing light through turbid media**
  I.M. Vellekoop and A.P. Mosk, Optics Communications **211**, 3071 (2008).

- **Coherent backscattering and localization of light**
  C.M. Aegerter and G. Maret, Progress in Optics **52**, 1 (2009).

- **Influence of gravity on a granular Maxwell's demon experiment**
  N. Isert, C.C. Maass, and C.M. Aegerter, Europ. Phys. J. E **28**, 205 (2009).

Articles in press

- **Velocity distributions of uniformly heated three dimensional granular gases**
  C.C. Maass, G. Maret, and C.M. Aegerter.

- **Determination of mechanical stress in** Drosophila **wing imaginal discs using photoelasticity**
  U. Nienhaus, T. Aegerter-Wilmsen, and C.M. Aegerter.

- **Effects of growth regulation by mechanical stress on epithelial topology**
  T. Aegerter-Wilmsen, A. Christen, E. Hafen, C.M. Aegerter, and K. Basler.

Conference reports

- **Velocity distributions in levitated granular gases (poster)**
  C.C. Maass, N. Isert, G. Maret, and C.M. Aegerter, Gordon conference on granular and granular fluid flow, Colby college, USA, June 22nd - 27th 2008.

- **Levitated granular gases**
  C.C. Maass, N. Isert, G. Maret, and C.M. Aegerter, Workshop of the European graduate college in soft condensed matter, Strasbourg, France, September 15th - 17th 2008.

- **Dynamics of levitated foams**
  N. Isert, R. Straub, G. Maret, and C.M. Aegerter, Workshop of the European graduate college in soft condensed matter, Strasbourg, France, September 15th - 17th 2008.

- **Monodisperse Spherical Nano-Particles for Optical Application**
  S. Shafaei, W. Bührer, S. Fiebig, G. Maret, and C.M. Aegerter, Workshop of the European graduate college in soft condensed matter, Strasbourg, France, September 15th - 17th 2008.

- **Coherent backscattering at small angles**
  S. Fiebig, W. Bührer, G. Maret, and C.M. Aegerter, Workshop of the European graduate college in soft condensed matter, Strasbourg, France, September 15th - 17th 2008.

- **Teaching quantitative Biology (poster)**
  C.M. Aegerter, Systemsbiology URPP retreat, Monte Verita, Switzerland, October 12-15 2008.

- **Forces in the wing imaginal disc of Drosophila melanogaster (poster)**
  T. Schluck, I.M. Vellekoop and C.M. Aegerter, All SystemsX-Day, Basel, Switzerland, October 16, 2008.

- **Anderson localization of light. (poster)**
  W. Bührer, S. Fiebig, G. Maret, and C.M. Aegerter, Symposium 50 years of Anderson localization, Paris, France, December 4th - 5th 2008.

- **Dynamics of Diamagnetically Levitated Foams (poster)**
  N. Isert, R. Straub, G. Maret, and C.M. Aegerter, Workshop 'Frontiers in soft matter', Les Houches, France, February 15th - 20th 2009.

- **Improvement of Synthesized Titania Particles for Anderson Localization Experiments (poster)**
  S. Shafaei, W. Bührer, S. Fiebig, G. Maret, and C.M. Aegerter, Workshop 'Frontiers in soft matter', Les Houches, France, February 15th - 20th 2009.

Invited lectures

- C.M. Aegerter: **Transport and localization of light in disordered systems**
  Summer School of the Karlsruher School of Optics and Photonics, Bad Herrenalb, Germany, 20.08.2008.

- C.M. Aegerter: **Coherent backscattering and Anderson localization of light**
  International Conference on Quantum Optics and Quantum Information, Vilnius, Lithuania, 20.09.2008.

- C.M. Aegerter: **Levitated granular gases**
  Deutsches Luft- und Raumfahrtzentrum, Köln, Germany, 18.11.2008.

- I.M. Vellekoop: **Universal optimal transmission of light through disordered materials**
  Physics@FOM, Veldhoven, The Netherlands, 20.01.2009.

- C.M. Aegerter: **Levitated granular gases**
  Workshop 'Frontiers in soft matter', Les Houches, France, 20.02.2009.

17.2.6 Miscellaneous

- H. Keller: **Physik ist überall - faszinierende Experimente aus dem Alltag**
  Demonstrationsvorlesung, 175-Jahr Feier, MNF-Tag, Universität Zürich, Zürich, Switzerland, April 19, 2008.

- H. Keller: **Hochtemperatur-Supraleitung - 20 Jahre danach**
  Talk, Studentenhaus Allenmoos, Zürich, Switzerland, April 23, 2008.